Title
Millimeter-wave polarimetry instrumentation and analysis

Author
Bierman, Evan M.

Publication Date
2011

Peer reviewed|Thesis/dissertation

UNIVERSITY OF CALIFORNIA, SAN DIEGO

Millimeter-Wave Polarimetry Instrumentation and Analysis

A dissertation submitted in partial satisfaction of the
requirements for the degree
Doctor of Philosophy

in

Physics

by

Evan M. Bierman

Committee in charge:

Professor Brian G. Keating, Chair
Professor George Fuller
Professor Larry Larson
Professor Hans Paar
Professor Gabriel Rebeiz

2011

The dissertation of Evan M. Bierman is approved, and it is acceptable in quality and form for publication on microfilm and electronically:

Chair

University of California, San Diego

2011

DEDICATION

To my wife and parents

for showing me how to be a better person.

EPIGRAPH

Interestingly, according to modern astronomers, space is finite. This is a very comforting thought – particularly for people who can never remember where they have left things.

—Woody Allen

I had a dream last night, I was eating a ten pound marshmallow. I woke up this morning and the pillow was gone.

—Tommy Cooper

You can't have everything. Where would you put it?"

—Stephen Wright

TABLE OF CONTENTS

LIST OF FIGURES

LIST OF TABLES

ACKNOWLEDGEMENTS

"If I have seen further it is only by standing on the shoulders of giants."
—Sir Isaac Newton

While that quote by Newton tends to be overused, it does not make it any less true. First and foremost I would like to thank my partner and best friend, Hollie, for so many things. It is hard to put into words what she has meant to me both personally and professionally. I have no doubt in my mind I would not be writing this thesis without her. And to Jonah, who provides me with endless motivation to do my best and to live life to the fullest.

My parents for always telling me, “You can do whatever you want!”, for supporting me no matter what, for coming along with me through so many different changes in direction. I could not have asked for a better set of role models. To my big brother as well, I don’t think you’ll ever know how much I appreciate you.

My friends and family are a beacon of strength to me on a daily, monthly, and yearly basis. To Florence and Doug; thank you for all the guidance and wisdom, and for the food and comfortable bed along my journey. Thank you Aunt Paula also for the comfortable bed and yummy food. To Bobby and Aaron for making sure I got into just enough trouble to keep me sane. To the Meyertholens and Sudanos, thank you for swimming up river with me. To Chuck, Gregg, Kaufman, Bulby, Berkowitz, Beliak, Sam, Goodman, Naomi, Aaron, Yoav, Chris, Josh, Max, Mike, Soto; I am the person today because you have all made it possible. To the Biermans, Andrews, Owens, Dietzs, Silvers, Fuchs, Roths, Kayes, Brooks, Rockowers; you’ve always made this world seem brighter.

I had the good fortune to join an incredibly smart and hard working team to teach and guide me along the way. My fellow graduate students in crime, Kiwon, Cynthia, and Yuki who have taught me so much. To John, Denis, and Darren: there’s no way I could possibly explain what an honor it was to work with you. To Ed and NASA Goddard; one of my biggest regrets in grad school is that I couldn’t find a way to collaborate more with you. To my other GSRPers; I’m glad we all met and had a chance to meet and learn from one another. To Andrew; I’m not sure if I will ever understand, but your legacy, brilliance, and warm nature will always live on. To Jamie, Bill H., Tomo, John, Viktor, Bill J., Chaolin, Eric, Pete, Hien, Clem, Steffan, Graca, Chris, Justus, Mike; it was a pleasure to work with and learn from you all. To Nate, Jon, Ian, Dave, Darcy, Marc, Chad, Cristel, Eric; for making SERF a fun and interesting place to come everyday. To my MBI collaborators; thank you for letting me be a part of something so unique and interesting. To Tom; I will come pick you up at whatever train station you want no matter what time it is. To Meir; for pushing me to be more than just a flower picker.

Lastly to Brian; you provided me with amazing opportunities to use my skills in so many different ways and so many different situations. My resume is full because of you. I thank you without hesitation for teaching me and helping me get my Ph.D. and become a professional.

Technical acknowledgements: Chapter 1, in full (with minor exceptions to conform to this thesis), is a reprint of the material as they were submitted to the Astrophysical Journal, February 2011, E. M. Bierman, T. Matsumura, C. D. Dowell, B. G. Keating, P. Ade, D. Barkats, D. Barron, J. O. Battle, J. J. Bock, H. C. Chiang, T. L. Culverhouse, L. Duband, E. F. Hivon, W. L. Holzapfel, V. V. Hristov, J. P. Kaufman, J. M. Kovac, C. L. Kuo, A. E. Lange, E. M. Leitch, P. V. Mason, N. J. Miller, H. T Nguyen, C. Pryke, S. Richter, G. M. Rocha, C. Sheehy, Y. D. Takahashi, K. W. Yoon, “A Millimeter-Wave Galactic Plane Survey with the BICEP Polarimeter”. The dissertation author was the primary investigator and first author of this paper.

VITA

Education

2011	Ph.D., Physics, University of California, San Diego
2010	M.S., Physics, University of California, San Diego
2008	C.Phil., Physics, University of California, San Diego
1999	B.A., Physics, University of California, Berkeley

PUBLICATIONS

Gault, et al., “Measurements of a Cryogenic Linear Polarization Modulator for mm-Wavelengths”, *2011*

Bierman, et al., “A Millimeter-Wave Galactic Plane Survey with the BICEP Polarimeter”, *2011*

Chiang, et al., “Measurement of CMB Polarization Power Spectra from Two Years of BICEP Data”, *2009*

Takahashi, et al., “Characterization of the BICEP Telescope for High-Precision CMB Polarimetry”, *2009*

Tucker, et al., “The Millimeter-Wave Bolometric Interferometer (MBI)”, *2008*

Yoon, et al., “BICEP: a Bolometric Large Angular Scale CMB Polarimeter”, *2006*

Timbie, et al., “The Einstein Polarization Interferometer for Cosmology (EPIC) and MBI”, *2006*

ABSTRACT OF THE DISSERTATION

Millimeter-Wave Polarimetry Instrumentation and Analysis

by

Evan M. Bierman

Doctor of Philosophy in Physics

University of California, San Diego, 2011

Professor Brian G. Keating, Chair

The chapters in this thesis roughly follow a reverse chronological order of my work in graduate school. Chapter 1 is the culmination of work with Dr. Dowell at Caltech, motivated by Professor Keating, to study polarized Galactic emission. Although the main goal of BICEP was to search for CMB B-modes, observation time was also spent on the Galactic plane region. Initially the data were collected to understand Galactic emission as a foreground of CMB polarization; however, the final paper focused on studying Galactic physics and not the CMB. Through comparison of BICEP data to other experiments, different models of the polarization production were explored. This paper also served as the initial instrument paper for the 220 GHz hardware added to BICEP for the second and third observing seasons.

Chapter 2 is the software analysis work related to the paper in Chapter 1 that either did not make it into the paper or did not pan out. To explore BICEP's capabilities and produce better maps different scan strategies were explored such as full 360° scans and elevation scanning. BICEP observations are contaminated on large scales by a noise source that has not been fully identified. Different mapmaking methods were explored to remove this systematic as well as $1/f$ noise and telescope systematics to maximize

recovered signal.

Chapter 3 represents a sample of contributions to the BICEP telescope and the UCSD FTS. To characterize the spectral response of the BICEP telescope and the faraday rotation modulators, I helped design and construct the UCSD including layout and optical design, synthesizing wire grids, integrating the system with our lab's test cryostat, and developing software and analysis tools. My main contribution to the CMB polarization work on BICEP was analysis of calibration data. Specifically I talk about my work to understand the beams and differential pointing from observations of the Moon.

Chapter 4 represents my work on Faraday Rotation devices. Initially, these devices were developed to overcome $1/f$ noise and some beam systematics; however, the usage of these devices were limited and their full capabilities were not tested. The devices were shown to work generally as designed and were followed up by similar devices developed and deployed for the MBI-4 experiment.

Figure 0.1: Picture of the BICEP telescope at the geographic South Pole taken by Dr. Denis Barkats (2006 winter-over) taken at sunset. The aurora, stars, and Moon are all visible. The picture shows the isolation of the Dark Section Laboratory compared to what exists naturally in this environment. The telescope is on the second floor of the building, on the right side, looking up through the reflective metal ground shield.

Chapter 1

A Millimeter-Wave Galactic Plane Survey with the BICEP Polarimeter

1.1 BICEP Galaxy Paper Abstract

In addition to its potential to probe the Inflationary cosmological paradigm, millimeter-wave polarimetry is a powerful tool for studying the Milky Way galaxy's composition and magnetic field structure. Towards this end, presented here are Stokes I, Q, and U maps of the Galactic plane from the millimeter-wave polarimeter BICEP covering the Galactic longitude range $260^\circ < \ell < 340^\circ$ in three atmospheric transmission windows centered on 100, 150, and 220 GHz. The maps sample an optical depth $1 \lesssim A_V \lesssim 30$, and are consistent with previous characterizations of the Galactic millimeter-wave frequency spectrum and the large-scale magnetic field structure permeating the interstellar medium. Polarized emission is detected over the entire region within two degrees of the Galactic plane and indicates that the large-scale magnetic field is oriented parallel to the plane of the Galaxy. An observed trend of decreasing polarization fraction with increasing total intensity rules out the simplest model of a constant Galactic magnetic field orientation along the line of site in the Galactic plane. Including WMAP data in the analysis, the degree-scale frequency spectrum of Galactic polarization fraction is plotted between 23 and 220 GHz for the first time. A generally increasing trend of polarization fraction with electromagnetic frequency is found,

which varies from 0.5%-1.5% at frequencies below 50 GHz to 2.5%-3.5% above 90 GHz. The BICEP and WMAP data are fit to a two-component (synchrotron and dust) model showing that the higher frequency BICEP data are necessary to tightly constrain the amplitude and spectral index of Galactic dust. Furthermore, the dust amplitude predicted by this two-component fit is consistent with model predictions of dust emission in the BICEP bands. The polarization angles in all three bands are generally perpendicular to those measured by starlight polarimetry and show changes in the structure of the Galactic magnetic field on the scale of 60°. Map noise and systematic effects are characterized and the resulting maps and derived parameters are corrected for spectral mismatch leakage and time-series filtering effects. The effort to extend the capabilities of BICEP by installing 220 GHz band hardware into the existing BICEP focal plane is described along with the results of the data analysis from the new band.

1.2 Introduction

Emission from the Milky Way Galaxy at millimeter wavelengths is both a rich source of astrophysical information and a potential contaminant for cosmic microwave background (CMB) observations. The density of gas and dust in the interstellar medium (ISM) varies from very low (< 1 particle cm^{-3}) in diffuse regions to very high ($> 10^6$ particle cm^{-3}) in molecular clouds and complexes (collections of star-forming cloud cores at approximately the same distance and age). Measurements in the millimeter band have the potential to probe a wide range of ISM densities while near-IR bands (Martin & Whittet, 1990) have enough resolution to probe medium to high density ISM regions.

In general, large-scale diffuse emission from the Galaxy at frequencies below 90 GHz is dominated by the synchrotron mechanism in ionized gas, and to a lesser extent free-free along with thermal emission from rotational and vibrational modes of dust (Rybicki & Lightman, 1979). Emission at frequencies above 90 GHz is dominated by vibrational modes of Galactic dust (Whittet, 1992). However, not all emission mechanisms give rise to polarized radiation. For example free-free emission from electron-ion scattering can contribute to the measured intensity (although it is not the dominant at any millimeter-wave band) near 90 GHz; however, this emission is not polarized. The exact composition of the Galaxy's emission spectrum varies across the sky and can change when observing polarized intensity. Multi-wavelength observations in the infrared and millimeter can determine the properties of the continuum emission, spectral lines, and polarization.

Polarized radiation probes various aspects of the ISM and Galactic magnetic field. Dust grains aligned perpendicular to the Galactic plane by the Galactic magnetic field preferentially absorb and scatter starlight in one direction, causing more extinction of one polarization mode compared to the other (Davis & Greenstein, 1951; Hiltner, 1951; Hildebrand, 1988a; Fosalba et al., 2002; Lazarian, 2007). Optical polarimetric observations of stars have revealed that the dust grains, and hence the Galactic magnetic field in the diffuse component, are preferentially oriented parallel to the Galactic plane (Mathewson & Ford, 1970). Complementary to this, dust grains aligned along their long dimensions by the Galactic magnetic field emit radiation in the infrared and millimeter bands polarized orthogonally to the Galactic magnetic field (Lazarian, 2007). The desire to characterize the ISM and the Galactic magnetic field provides the motivation for millimeter-wave continuum polarimetry of the Galaxy (Hildebrand, 1988b; Hildebrand et al., 1999; Chuss et al., 2003; Novak et al., 2003; Benoît et al., 2004; Matthews et al., 2009; Culverhouse et al., 2010; Dotson et al., 2010).

The main goal of the Background Imager of Cosmic Extragalactic Polarization (BICEP, Keating et al. 2003a; Chiang et al. 2010) and its successors[1] is to search for the unique CMB B-mode polarization pattern due to primordial gravitational waves, which has an amplitude determined by the energy scale of inflation (Seljak & Zaldarriaga, 1997; Kamionkowski et al., 1997). Polarized Galactic emission is an astronomical foreground (Bock et al., 2008) that may need to be confronted to make this measurement, and therefore, the properties of the emission also motivate the investigation (Jones, 2003; Ponthieu et al., 2005; Tucci et al., 2005; Eriksen et al., 2006; Hansen et al., 2006; Amblard et al., 2007; Larson et al., 2007; Eriksen et al., 2008; Leach et al., 2008; Miville-Deschênes et al., 2008; Dodelson et al., 2009; Dunkley et al., 2009). Only a few experiments have explored large-scale Galactic polarization properties at frequencies between 90 GHz and 350 GHz, such as Archeops (353 GHz, Benoît et al. 2004),

[1] list of future space, balloon, and ground CMB experiments: http://cmbpol.uchicago.edu/workshops/technology2008/depot/meyer-stephan.pdf

WMAP (94 GHz, Kogut et al. 2007), and QUaD (100 and 150 GHz, Culverhouse et al. 2010). To further study emission from sources other than the CMB, BICEP was upgraded from a two-band experiment (100 and 150 GHz) to a three-band polarimeter with the addition of 220 GHz capability for the second and third seasons. This paper discusses unique aspects of the BICEP Galactic observations, including the Galactic maps with the additional 220 GHz channels (Section 1.4.1), explains the data analysis methodology (Section 1.3.2-1.3.5), and discusses the analysis of the polarized Galactic signal(Section 1.4.6-1.4.7).

1.3 BICEP Instrument and Mapmaking

1.3.1 Brief Instrument Description

For a complete description of the BICEP telescope see Yoon et al. (2006) and Takahashi et al. (2010). BICEP is an on-axis refracting telescope with a 250 mm aperture and can scan in azimuth and elevation as well as rotate around the optical axis (boresight) of the telescope, which is less than 0.01° away from the center feed. BICEP's small aperture allows the entire optical system to be cooled to cryogenic temperatures in a vacuum cryostat, sealed with a millimeter-wave transparent foam window. While located at the South Pole, the telescope mount is enclosed at room temperature within the observatory, protected by a fabric bellows structure. To control the response of the beam sidelobes and minimize ground contamination, the telescope has an inner co-moving absorptive forebaffle and a fixed reflective outer ground screen, similar to that used in POLAR (Keating et al., 2003b). The readout electronics are sealed in an RF-tight cage and consist of detector AC biasing circuits, analog preamplifiers, lock-in amplifier cards, and cold JFETs in the cryostat.

The focal plane is comprised of 49 pairs of polarization sensitive bolometers (PSBs) (Jones et al., 2003), two orthogonal detectors per feed, whose responses are summed or differenced to measure total intensity and polarization, respectively. For the first observing season in 2006, the focal plane had twenty-five feeds tuned for the 100 GHz atmospheric transmission window and twenty-four tuned for the 150 GHz atmospheric window. For the second and third observing seasons, the focal plane consisted of twenty-five 100 GHz feeds, twenty-two 150 GHz feeds, and two new feeds tuned for the 220 GHz atmospheric transmission window (discussed in Appendix 1.8.1). Three corrugated feedhorn sections, cooled to ≤ 4 K, couple radiation from the two high-density polyethylene lenses to each PSB while also providing a sharp low-frequency cutoff for the band. The high-frequency cutoff is defined by a set of metal mesh filters (Ade et al., 2006) attached to the feedhorn stack. The filters and PSBs are cooled to 250 mK by a ^{4}He-^{3}He-^{3}He-sorption refrigerator system (Duband et al., 1990). Teflon filters block out-of-band infrared radiation to minimize optical loading.

1.3.2 Scan Strategy

Figure 1.1 shows the three main BICEP observing regions overlaid on the Galactic dust model of Finkbeiner et al. (1999) (hereafter FDS) evaluated at 150 GHz. Approximately 10,000 hours were spent observing a region predicted to have minimal astronomical foreground contamination in an attempt to detect the B-mode signature of inflationary gravitational waves ("CMB" region), 945 hours were dedicated to observing the Galactic plane in a region near the center of the Galaxy ("Gal-bright" region, $300^\circ < \ell < 340^\circ$) and 1484 hours were spent observing the Galactic plane in a region farther from the Galactic center ("Gal-weak" region, $260^\circ < \ell < 300^\circ$).

BICEP observes all regions in a similar manner. The smallest observing unit is a 'half-scan'; a uni-directional azimuthal telescope movement at constant elevation that lasts 27 seconds. To avoid potential thermal disturbances, 3.5 seconds are cut at the beginning and end of each half-scan. The choice of scan speed is bounded at low frequency by the atmosphere and detector stability, and bounded at high frequency by the bolometer time constant. Within those constraints, the telescope scan speed is chosen to be $2.8^\circ/\mathrm{sec}$ to minimize microphonics and thermal drifts. A 'scan-set' lasts approximately one hour and consists of 50 half-scans each in the positive and negative azimuthal directions at a given elevation.

A calibration period at the beginning and end of each scan-set consists of a small one degree elevation movement, called an 'el-nod', which serves as the primary relative gain calibration within a feed and across the focal plane. Atmospheric loading is proportional to the line-of-sight air-mass, which is well modeled as $\csc(\theta_{el})$ plus an offset,

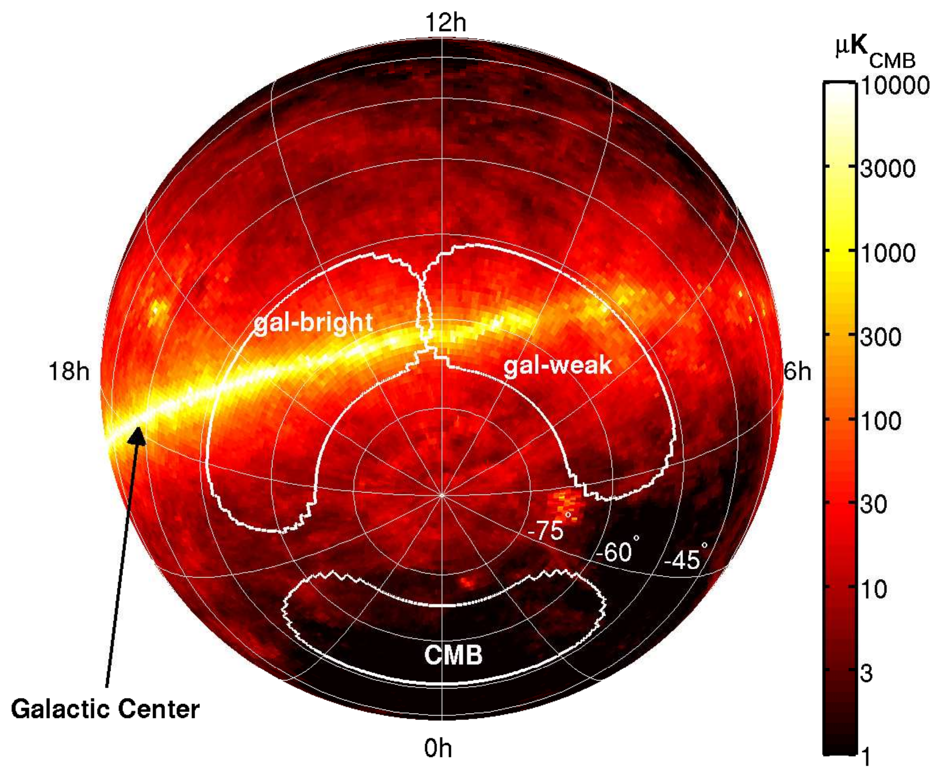

Figure 1.1: 150 GHz FDS Model 8 dust emission prediction (Finkbeiner et al., 1999), shown in equatorial coordinates. BICEP's primary CMB observing field is called "the southern Galactic hole", a region of low dust emission used for optimal B-mode detection. The two Galactic fields are used for studying astronomical foregrounds and Galactic physics. The Gal-weak region spans the Galactic plane from Galactic longitude $260^\circ < \ell < 300^\circ$, while the Gal-bright region spans the plane from $300^\circ < \ell < 340^\circ$.

where θ_{el} is the elevation angle. El-nods produce a similar detector response (approximately 100 mK peak to peak) across all detectors for an elevation change of one degree. To normalize the response over time, the average response during the el-nod for all the detectors in each band is calculated and divided out.

As opposed to tracking the celestial observing center, BICEP centers each scan-set about a fixed azimuth angle causing sky sources to move relative to the scan center, while stationary ground and scan thermal/optical contamination remains fixed. This has the added benefit of grouping both the scan and ground contaminations into one contamination ("scan-fixed contamination"). Chiang et al. (2010) takes this process a step further and removes a template of the scan-fixed contamination from each scan-set; however, this additional step was not necessary in this paper because of the much larger polarization signal relative to the noise.

After each scan-set, the telescope is stepped in elevation by 0.25° and moved in azimuth to locate the next scan-set about the center of the observing region. Each set of scan-sets (called a "phase") consists of seven (lasting six hours) or ten (lasting nine hours) steps at one of four orientations about the boresight (0°, 180°, 135°, 315°) centered in the elevation range 55° to 60°. Observations of the Gal-weak field were carried out mostly in six hour phases in Austral winter. Observations of the Gal-bright field consisted primarily of nine hour phases during Austral summer 2008, although there were a few other six hour phases executed at various times during the three years of observing.

Timestream statistics (such as the variance, skew and kurtosis of a half-scan) and el-nod calibration values are used to determine nominal observing conditions. These statistics allowed the data to be cut on various time scales such as per-phase, per-scan-set and per-scan bases. Gal-bright observations use 763 out of 945 total possible hours and Gal-weak observations use 1463 out of 1484 total possible hours based on el-nod cuts, while scan statistics cut approximately 5% of the remaining data.

1.3.3 Spectroscopic Characterization

Instrumental properties of the telescope can cause noticeable effects in the observed Galaxy maps unless they are properly taken into account. One of the most pernicious of these properties is the spectral response mismatch, which can affect the resulting maps differently depending upon the observed source's spectrum. The key instrumental properties of BICEP are summarized in Table 1.1 as described in this section, Appendix 1.8.2 and Takahashi et al. (2010).

For all PSBs used in BICEP, at all three frequency bands, detected radiation from the sky produces a bolometer signal,

$$d(t) = K(t) \otimes \Big\{ n(t) + g(t) \int d\nu A_e(\nu) F(\nu) \int d\Omega\, P(\Omega) \tag{1.1}$$

$$\Big(I + \gamma (Q \cos(2\psi) + U \sin(2\psi) \Big) \Big\}, \tag{1.2}$$

where I, Q, and U are the total intensity and two linear polarization Stokes parameters on the sky respectively. BICEP is incapable of measuring the fourth Stokes parameter V, which accounts for circular polarization. However, for the CMB and Galaxy emission, V is expected to be negligible compared with the two linear Stokes parameters. The effective antenna area, A_e, is assumed to be proportional to ν^{-2}. To recover the underlying sky signal from the detector voltage timestreams $d(t)$, each of the following parameters is calibrated as described in Takahashi et al. (2010): ψ, the detector polarization angle; ϵ, the cross-polarization response; $\gamma = \frac{1-\epsilon}{1+\epsilon}$, the resulting polarization efficiency; $P(\Omega)$, the antenna response as a function of angular position Ω; $F(\nu)$, the end-to-end detector spectral response including filters, feedhorns, lenses, etc.; $g(t)$, the detector responsivity; $n(t)$, the noise; $K(t)$, the time-domain bolometer transfer function and filtering due to the electronics that is convolved ("$\otimes$") with the detector signal.

Takahashi et al. (2010) explored the leakage of total intensity to polarization for each feed, estimated using individual PSB pair-sum and pair-difference maps from the CMB region. The relative gain uncertainty is similar to spectral gain mismatch but can include other effects such as thermal response mismatch. The maps were cross-correlated, showing the relative gain uncertainty was less than 0.8% and 1.3% for 100 and 150 GHz feeds respectively. It was found that the relative gain mismatch for the 220 GHz pixels was 10% and visual inspection of the maps showed the two 220 GHz detectors gave inconsistent polarization results. The cause of this inconsistency was found to be mostly attributable to spectral gain mismatch.

Table 1.1: Telescope Characteristics

Characteristics of BICEP from its three observing seasons. While not an exhaustive list of all possible categories and errors, the listed parameters show the properties of the polarimeter relevant for this paper. Section 1.3.3 discusses the spectroscopic characterizations in more detail, while a brief discussion of the other BICEP characterizations are in Appendix 1.8.2 and Section 1.4.3.4 with further discussion in Takahashi et al. (2010). Characteristics for 100 and 150 GHz are consistent with Takahashi et al. (2010) except for spectral characterizations.

Instrument Property (Band Average)	100	150	220
Number of Feeds (2006, 2007-2008)	25, 25	24, 22	0, 2
Polarization Orientation Uncertainty	$< 0.7^\circ$	$< 0.7^\circ$	$< 0.7^\circ$
Pair-Relative Polarization Orientation Uncertainty	0.1°	0.1°	0.1°
Polarization Efficiency, γ	0.92	0.93	0.85
Optical efficiency (OE)	20.8%	19.8%	15.8%
Gaussian Beam Width (FWHM)	0.93°	0.60°	0.42°
Differential Pointing / Beam Size	1.0 %	1.8 %	2.6 %
Ghost Beam Power	0.41%	0.50%	1.3%
Ghost Beam Power, Pair-Difference	0.02%	0.04%	0.04%
Spectral Band Centers, flat source (GHz)[a]	95.5	149.8	208.2
Spectral Band Centers, Galaxy (GHz)	96.3	152.4	212.2
Spectral Gain Mismatch[b]	0.17%	0.19%	0.72%
Relative Gain Uncertainty[b]	0.8%	1.3%	$< 10\%$
Absolute Gain Uncertainty	2%	2%	15%
Noise Equivalent Temperature (μK$\sqrt{s}$)	530	450	1040
($MJy/sr\sqrt{s}$)	0.12	0.18	0.50
Noise Equivalent Q-Polarization[c] (μK$\sqrt{s}$)	410	340	880
($MJy/sr\sqrt{s}$)	0.090	0.14	0.42

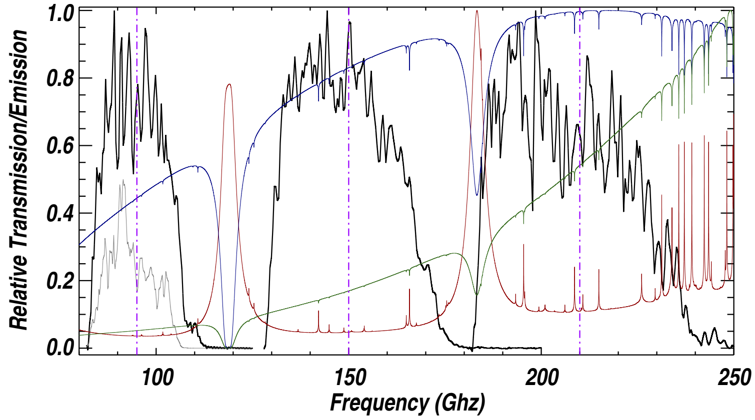

Figure 1.2: BICEP's three electromagnetic frequency spectra, $F(\nu)$, normalized to unity (black) with the band centers (shown as vertical purple dashed lines). Also plotted is the average spectral response for WMAP's 94 GHz band normalized to 0.5 (gray) and the spectral radiance, $S(\nu)$, for a model of atmospheric emission at the South Pole (red; Grossman (1989)), the spectrum (blue) of the CMB anisotropy (temperature derivative of the Planck function evaluated at 2.725 K (Fixsen & Mather, 2002)) and a typical Galactic emission spectrum (green) in the BICEP observing region, as seen through the atmosphere.

A careful campaign to characterize all of BICEP's feeds was undertaken in January 2008 at the South Pole using a high resolution (up to 250 MHz resolution) polarized Fourier transform spectrometer (FTS). The optical alignment and power falling on each pair of bolometers in a feed was calibrated before a set of eight independent spectral measurements were taken. Figure 1.2 shows $F(\nu)$, the average spectral responses for each band with the FTS's source spectrum divided out, assuming the FTS's source filled the pixel's beam.

If not calibrated properly, mismatched spectral responses can cause spurious polarization in detector differences and gain errors among different feeds. For example, the WMAP satellite (Jarosik et al., 2007) notes that passband mismatch is a problem; solved by fitting out for a spurious map component. The value of the mismatch is quoted as 1% on average with a maximum of 3.5% for the 23 GHz band (Page et al., 2007), in agreement with pre-flight spectral measurements. BICEP does not have sufficient polarization angle coverage for each feed to fit out the spurious component; however, it is possible to use the measured spectral responses to mitigate this effect.

BICEP's spectral response mismatch leaks intensity into polarization and is caused by the combination of two effects. First, several feeds have mismatched spectra, most notably the two 220 GHz feeds. Second, each PSB is calibrated relatively using the change in atmospheric loading with elevation; however, atmospheric emission has a different spectrum than Galactic emission or the CMB. The spectral mismatch leakage is calculated using the measured instrumental spectral response, a model of the atmospheric emission at the South Pole (Grossman, 1989), and a model of the typical Galactic spectrum in the 220 GHz observing region derived from fitting Equation 1.19 to BICEP and WMAP data as performed in Section 1.4.5.

The spectral gain mismatch (ξ) is :

$$\xi = \frac{G_A - G_B}{G_A + G_B} \tag{1.3}$$

where the responsivities, $G_{A,B}$, represent the two PSBs in a feed and are given by

$$G_{A,B} = \frac{\Gamma_{atmosphere}}{\Gamma_{Galaxy}} \tag{1.4}$$

$$\Gamma_{source} = \int F(\nu) S(\nu)\ \nu^{-2} d\nu \tag{1.5}$$

where $S(\nu)$ is the spectral radiance $\left(\frac{W}{sr\ m^2\ Hz}\right)$ of the source and ν^{-2} accounts for the throughput of the optics, which are assumed to be single-moded.

Shown in Figure 1.3 are examples of the spectral gain mismatch between two PSBs in a feed for each band and the spectral gain mismatch per frequency given by:

$$\frac{d\xi}{d\nu} = \left(\frac{F_A(\nu)}{\Gamma_{A,Galaxy}} - \frac{F_B(\nu)}{\Gamma_{B,Galaxy}}\right) S_{atmosphere}(\nu)\ \nu^{-2} / (G_A + G_B) \tag{1.6}$$

The integral of the leakage fraction, $\frac{d\xi}{d\nu}$, over the bounds shown gives the total spectral leakage measured for that feed, ξ. The leakage at 220 GHz comes from the combination of a small difference in lower band edge and a large amount of power from the atmospheric water line at 185 GHz. The average magnitudes of the spectral gain mismatch are 0.17%, 0.19%, 0.72% for 100, 150, and 220 GHz, respectively, using a typical Galactic source spectrum and median precipitable water vapor conditions at the South

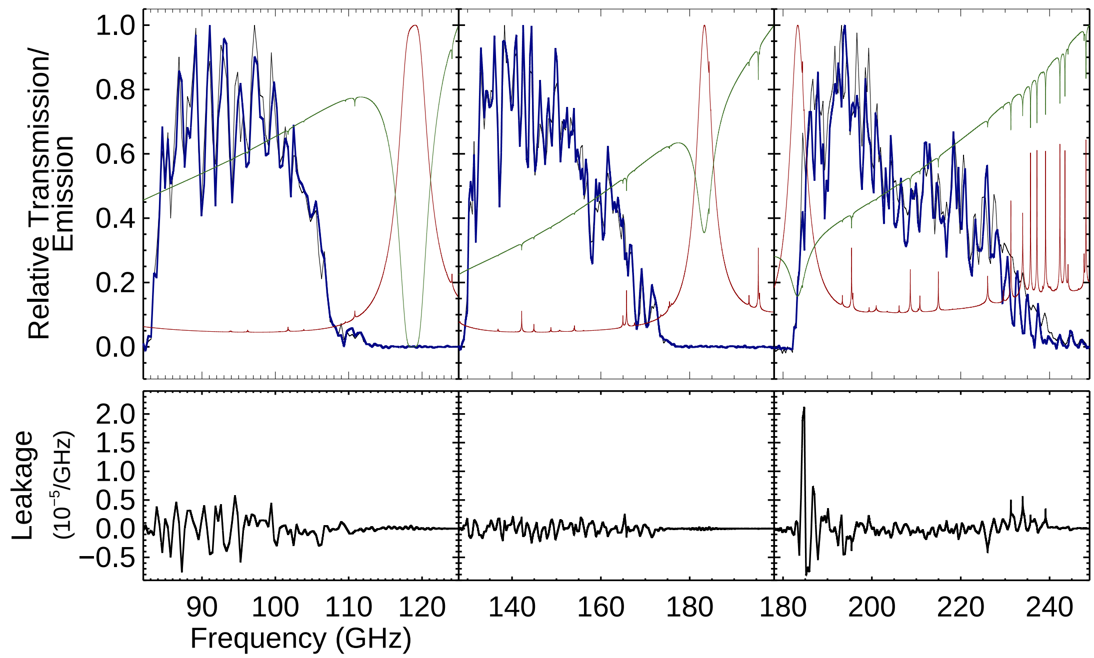

Figure 1.3: Spectral gain mismatch for one feed at each of BICEP's three bands. The top plots show the measured spectral responses for the two PSBs in a feed, "A" (Black) and "B" (Blue), along with a model of atmospheric transmission at the South Pole during median Austral winter conditions (red; Grossman (1989)) and a typical Galactic source spectrum (green) in the 220 GHz analysis region, as seen through the atmosphere. The bottom three plots show the leakage fraction per frequency, $\frac{d\xi}{d\nu}$, if calibrated off the atmospheric emission but observing the Galactic source spectrum as shown.

Pole during Austral winter. Changing the observed source or atmospheric conditions can have an appreciable change in these numbers. For example, one of the 150 GHz feeds has a 0.12% leakage during typical Austral summer conditions but can change in value by 0.5% depending on the atmospheric model. In this paper, typical values are used to correct the maps for this effect and simulations are carried out to probe the effects of the uncertainty in this calculated parameter.

The absolute gain calibration for BICEP maps at each frequency, co-added over all detectors, is determined by comparing total intensity angular cross power spectra from the BICEP CMB region to the angular power spectra found by WMAP in the same region (see Chiang et al. (2010) and Takahashi et al. (2010) for more details). Spectral gain mismatch between feeds could potentially introduce systematic effects into the analysis via feed calibration differences. Comparing the two 220 GHz-feed intensity maps, a difference of 30% is found. While this discrepancy was initially suspected to be due to spectral gain mismatch between different feeds, an investigation into the origin of this discrepancy did not find that this was the cause. While calibration per feed is important, this effect does not leak intensity power to polarization, and the quantities studied in this paper are mostly relative quantities insensitive to this systematic. Therefore a calibration error per feed will not significantly affect the results of this paper.

While the three bands are called “100 GHz”, “150 GHz”, and “220 GHz”, these are not the actual band centers. The band center for a given source is calculated as:

$$\nu_0 = \frac{\int_{\nu_L}^{\nu_H} \nu\, F(\nu)S(\nu)\, \nu^{-2}\, d\nu}{\int_{\nu_L}^{\nu_H} F(\nu)S(\nu)\, \nu^{-2}\, d\nu}, \tag{1.7}$$

where $F(\nu)$ is the measured average spectral response for each band, $S(\nu)$ is the source emission spectrum, and ν^{-2} accounts for the throughput of the receiver. For a flat spectral source, this gives 95.5, 149.8, and 208.2 GHz for 100, 150, and 220 GHz bands respectively. The dominant source of uncertainty is due to the optical setup and whether the FTS source is beam filling or not. This can change these values by 0.5, 0.8, and 1.0 GHz for 100, 150 and 220 GHz respectively. Changing the integration limits can also change these values by approximately 0.1 GHz for each band. If the band center is determined using a CMB source as seen through the atmosphere this gives band centers 96.2, 150.6, and 208.8 for 100, 150 and 220 GHz. If the band center is determined using a typical Galactic source with dust and synchrotron emission, as seen through the atmosphere, this gives band centers 96.3, 152.4, and 212.2 for 100, 150 and 220 GHz. Another way to calculate the average band center is to compute the band center for each detector separately and then average over all the detectors in a band. Doing this for the Galactic spectrum gives average band centers of 96.3, 152.3, 212.0 GHz with uncertainties in the average of 0.1, 0.3, and 1.0 GHz for 100, 150 and 220 GHz respectively. The standard deviation of the distributions over the detectors are 0.4, 1.4, and 2.1 GHz for 100, 150 and 220 GHz respectively, showing how different the spectral responses of a given detector in a band can be. Out-of-band high frequency response is less than -25 dB, which was characterized by using high-pass thick-grille filters and a chopped source.

1.3.4 Time Domain Data Processing

Following the el-nod calibration and correction for spectral gain mismatch, the sum and the difference of a PSB pair are calculated. Differencing the calibrated orthogonally linearly polarized detectors removes most of the unpolarized atmospheric response and unpolarized, scan-fixed, contamination. Atmospheric $1/f$ noise dominates the *rms* of the pair-sum timestreams for a typical half-scan. These fluctuations can be less than 1 mK in good weather or reach approximately 300 mK in bad weather, with a $1/f$ knee as high as a few Hertz. The data also contain a sub-dominant scan-fixed contamination, which does not integrate down as uncorrelated noise. To remove both $1/f$ atmospheric and scan-fixed contamination, the data from each half-scan are high-pass filtered by removing a second-order polynomial fit to each half-scan, at the cost of removing some Galactic signal as well. The pair-sum and pair-difference timestreams are treated separately but with the same filtering.

Polynomial removal causes an obvious distortion of the signal when the scans include the Galactic plane. To reduce this effect, the Galaxy is masked during the determination of the polynomial fit ("polynomial mask"). The preferred filtering scheme uses a second-order polynomial while masking out samples $|b| < 4°$. This scheme achieves a compromise between noise filtration and signal preservation. This process is not perfect and some residual filtering effects remain in the maps, as discussed in Section 1.4.3. A dedicated study of different filtering techniques was undertaken but none improved the maps significantly without causing worse filtering effects or adding additional noise. For example, maps with only a DC offset removed have less filtering applied to the data but also have large scale non-physical features that makes quantitative analysis unreliable.

There is an added complication in this scheme for scans that end within the masked region (Figure 1.4). A polynomial constrained by measurements on both sides of the Galactic plane closely approximates the low-frequency drifts within the interpolated region. However, scans not constrained on both sides of the plane require the polynomial to be extrapolated beyond the fitted region. Extrapolated polynomials tend to diverge because there are no data constraining the fit. Therefore, the filtering scheme is modified so that scan portions that end within the masked region are excluded, giving rise to maps with a missing wedge (Figure 1.5). Additionally, a brief measurement on both sides of the plane was not enough to constrain the polynomials sufficiently. Therefore, scans were required to have at least 10 samples on either side of the Galactic plane to be used in the mapmaking process.

1.3.5 Mapmaking

Once the data-processing steps are completed, the Stokes parameters I, Q, and U are derived using standard techniques (Jones et al., 2007). Equation 1.1 can be simplified to

$$d'_{A,B} = g_{A,B}\Big(I + \gamma_{A,B}\,\Big(Q\,\cos(2\,\psi_{A,B}) + U\,\sin(2\,\psi_{A,B})\Big)\Big), \tag{1.8}$$

assuming the beam functions are the same for a given pair of PSBs and the responsivities, $g_{A,B}$, still include the spectral gain mismatch after el-nod calibration. The Stokes parameters I, Q, and U now represent quantities integrated over Ω and ν, and $\{A,B\}$ refers to the two orthogonal bolometers within a given feed.

Before calculating the sum and difference data of the two PSBs in a feed, the spectral gain mismatch factors calculated in Equation 1.3 are corrected:

$$\begin{aligned} d_A &= d'_A \times (1+\xi) \\ d_b &= d'_b \times (1-\xi), \end{aligned} \tag{1.9}$$

where ξ is the spectral gain mismatch and the $d'_{A,B}$ denotes the uncorrected timestream data. The pair-sum (d_+) and pair-difference (d_-) timestreams can then be determined:

$$\begin{aligned} d_+ = \frac{d_A + d_B}{2} &= I + \alpha_+ Q + \beta_+ U \approx I \\ d_- = \frac{d_A - d_B}{2} &= \alpha_- Q + \beta_- U \approx Q\,\cos(2\,\psi_A) + U\,\sin(2\,\psi_A), \end{aligned} \tag{1.10}$$

which give rise to the Stokes parameters I, Q, and U where $\alpha_\pm$ and $\beta_\pm$ account for polarization angle:

$$\begin{aligned} \alpha_\pm &\equiv \frac{\gamma_A\,\cos(2\,\psi_A) \pm \gamma_B\,\cos(2\,\psi_B)}{2} \\ \beta_\pm &\equiv \frac{\gamma_A\,\sin(2\,\psi_A) \pm \gamma_B\,\sin(2\,\psi_B)}{2}. \end{aligned} \tag{1.11}$$

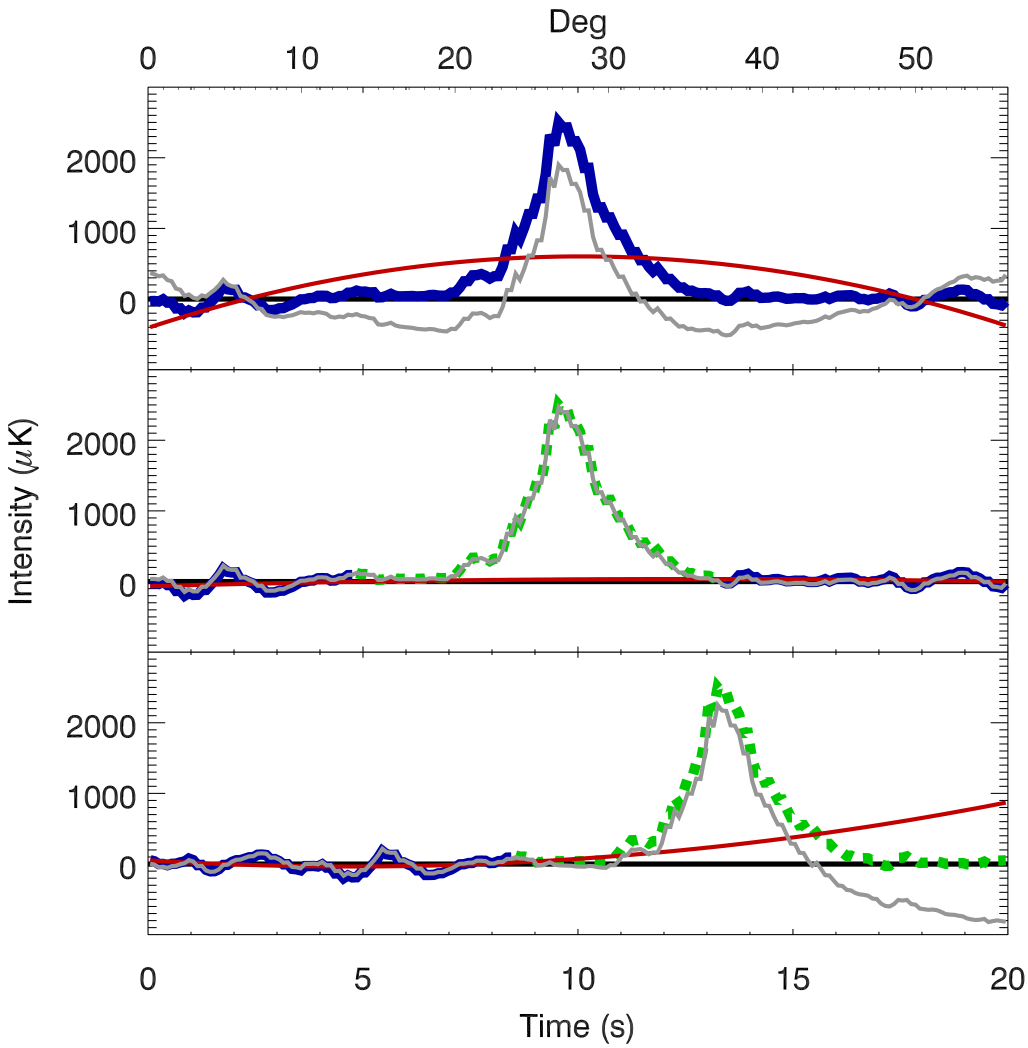

Figure 1.4: A detector timestream simulation showing three different polynomial filtering methods. The top plot shows a typical timestream resulting from a scan across the Galaxy (blue) with a fitted second-order polynomial (red) subtracted off, causing a significant distortion of the Galaxy (gray). The middle plot shows the same scan, except the Galaxy (green) has been excluded from the fit. The polynomial has been interpolated across the Galaxy leading to minimal filtering effects. The bottom plot shows a typical scan that ends on the Galaxy, requiring the polynomial to be extrapolated onto the Galaxy. The extrapolated polynomial causes severe distortion of the maps, requiring these scan portions to be excluded from the analysis.

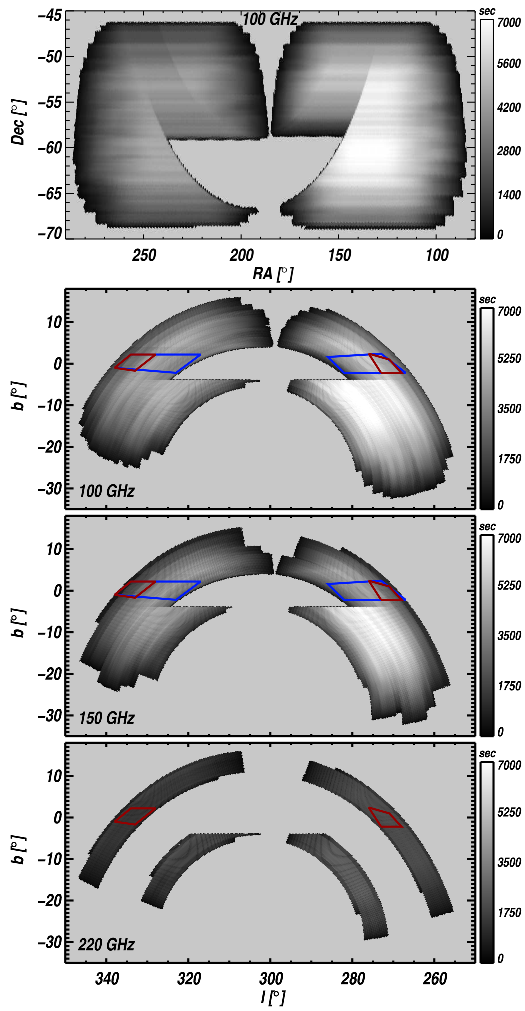

Figure 1.5: Integration time per 0.25° `Healpix` map pixel for 100 GHz (top: Celestial coordinates, second from top: Galactic coordinates), 150 GHz (second from bottom; Galactic Coordinates), and 220 GHz (bottom; Galactic Coordinates) derived from all three seasons co-added over all four boresight angles of BICEP observations. The wedge-shaped cuts in the map without integration time are from the omission of parts of scans with extrapolated polynomial fits (Section 1.3.4). The 100 GHz celestial coordinate map is an example of the native observation reference frame from the South Pole. The red outlined area (called the "220 GHz analysis region") is an area of the sky where analysis at all three bands can be carried out. This region is a subset of the blue outlined area on the 100 and 150 GHz maps (called the "100/150 GHz analysis region") where the final analysis can only be carried out at 100 and 150 GHz (See Section 1.4).

The A and B bolometers are assumed to be nearly perpendicular, so the pair-sum gives the total intensity to a very high precision. If γ is also assumed to be equal to one, then $\alpha_{\pm}$ and $\beta\pm$ simplify to {0, cos($2\psi_A$)} and {0, sin($2\psi_A$)}. However, γ is closer to 90%, and can differ by several percent between a given pair of bolometers within a feed, so no simplification is made during mapmaking using the pair-difference signal. After the spectral gain mismatch is corrected and after the sum and difference are taken, the resulting pair-sum and pair-difference timestreams are polynomial filtered as discussed in Section 1.3.4.

The I, Q, and U maps are given by:

$$m_{(I,Q/U)} = (A_T N^{-1} A)^{-1} A_T N^{-1} d_{(+,-)}, \tag{1.12}$$

which is a noise weighted linear least squares regression where m is the set of map pixels for a given Stokes parameter, N is the noise covariance matrix, and A is the pointing matrix. Since $d_{(+,-)}$ are filtered timestreams, the resulting sky maps $m_{(I,Q/U)}$ are also filtered. For this work, it is sufficient to assume that the noise is uncorrelated, making N diagonal and simple to invert. The variance associated with samples in a single half-scan is assumed to be time-independent, and is calculated from the samples lying outside the Galactic mask after polynomial subtraction. For the pair-sum data, the pointing matrix consists of ones and zeros, indicating whether or not the telescope is pointing at a particular map pixel. This simplifies Equation 1.12, only requiring the calculation of the weighted mean of d_+ to determine the total intensity map m_I (see Equation 5 in Chiang et al. (2010)). To determine the polarization maps $m_{Q/U}$ from the pair-difference data d_-, the pointing matrix consists of a combination of the α's and β's and Equation 1.12 can be written as:

$$\sum_{i=1}^{S_j} w_i \begin{pmatrix} \alpha_i d_i \\ \beta_i d_i \end{pmatrix} = \sum_{i=1}^{S_j} w_i \begin{pmatrix} \alpha_i^2 & \alpha_i \beta_i \\ \alpha_i \beta_i & \beta_i^2 \end{pmatrix} \begin{pmatrix} Q_j \\ U_j \end{pmatrix}. \tag{1.13}$$

The "-" subscript has been dropped from the d, α, and β terms for clarity. Equation 1.13 holds true for each band separately where d_i is a single pair-difference timestream sample, w_i is the inverse variance for a single sample, index j corresponds to a given map pixel, and S_j is the total number of samples from all the feeds per band in a given map pixel. After summing over i, the matrices per pixel per band are inverted to solve for

Q and U. For each map pixel, the seven quantities used to recover I, Q, and U are the pair-sum weights and pair-sum weighted data, pair-difference weighted data multiplied by α and β, and weighted α^2, β^2, and $\alpha\beta$. An eighth quantity, integration time per pixel, is also recorded in order to measure noise properties and observing efficiency.

1.4 Results

The BICEP polarimeter produced high signal-to-noise maps of the Galaxy in three different band including a qualitative discussion of the map features, investigation into map statistical and systematic uncertainties, a direct comparison to the maps observed by the WMAP satellite, and a quantitative analysis of the properties in the maps. For quantitative calculations, two analysis regions were defined (Figure 1.5). The "100/150 GHz analysis region" consists of 147 one degree `Healpix` map pixels that have intensity values greater than zero, located at less than two degrees in Galactic latitude, and a polarization fraction magnitude less than 20%. Since there were only two 220 GHz feeds installed in BICEP, this limited the sky coverage for that band. Therefore, a "220 GHz analysis region", using 53 of the 147 pixels from the 100/150 GHz analysis region, defines a subset of map pixels that can be analyzed at all three bands.

1.4.1 Intensity and Polarization Maps

Figures 1.6-1.9 show BICEP Galactic maps in three different bands, binned into 0.25° `Healpix` pixels, using second-order polynomial filtering while masking data $|b| < 4°$. Polarization angles are defined counterclockwise from the meridian at the map pixel, in accordance with the IAU definition (Weiler, 1973; Hamaker & Bregman, 1996). BICEP absolute calibration casts the maps in thermodynamic temperature (Mather et al., 1994; Bennett et al., 2003), which shows CMB anisotropy with the same value at all frequencies. This unit is convenient for CMB analysis and gives a consistent reference frame for emission from sources other than the CMB.

The total intensity maps in Figure 1.6 show the large contrast between the CMB temperature anisotropy ($|b| > 5°$) and the emission near the Galactic plane. The noise in the intensity maps is not white; however, it is barely visible at either 100 or 150 GHz, even off the plane, except at the edges of the map. The map pixels at the lower elevation have a lower signal-to-noise ratio due to the `Healpix` pixelization scheme that bins data into equal area pixels, while the scan strategy follows a Mercator projection. This effect is most readily visible in the 220 GHz maps when comparing the upper and lower portions of the map.

The total intensity maps overlaid with polarization vectors in Figure 1.7 show that the brightest Galactic emission is within two degrees of the plane and consists of smooth large scale features and compact sources along the plane. The maps show that the intensity signal dominates over the noise in the plane at all three bands and the polarization vectors are mostly perpendicular to the plane.

Figure 1.8 shows there is U signal in the plane corresponding to polarization vectors that are not perfectly perpendicular to the Galactic plane. There are regions of positive U polarization in the plane at all three bands. However, there is a region in the 150 GHz maps near Galactic longitude $\ell = 322^\circ$ that shows a significant amount of negative U signal that is not an artifact of the filtering or systematics. The noise appears mostly white over the whole observing region with some residual striping along the scan direction at this map resolution.

Figure 1.9 shows there is no significant negative Q polarization in the Galactic plane, which would have produced polarization vectors generally parallel to the Galactic plane. The noise is nearly identical in nature to the noise in the U maps because both are derived from the same pair-difference data with identical filtering.

1.4.2 Map Quantities and Polarization Fraction Model

The map quantities studied are I, the pixel intensities (Section 1.4.5); q, the polarization fraction perpendicular to the Galactic plane; η, the exponent of a simple power law describing the relationship between q and I(Section 1.4.6); and θ, the polarization angle in Galactic coordinates (Section 1.4.7). The derived variables q, u, p, and θ are given by:

$$q \equiv \frac{Q}{I},\ u \equiv \frac{U}{I},\ p \equiv \sqrt{q^2 + u^2},\ \theta \equiv \frac{1}{2}\tan^{-1}\left(\frac{U}{Q}\right) \tag{1.14}$$

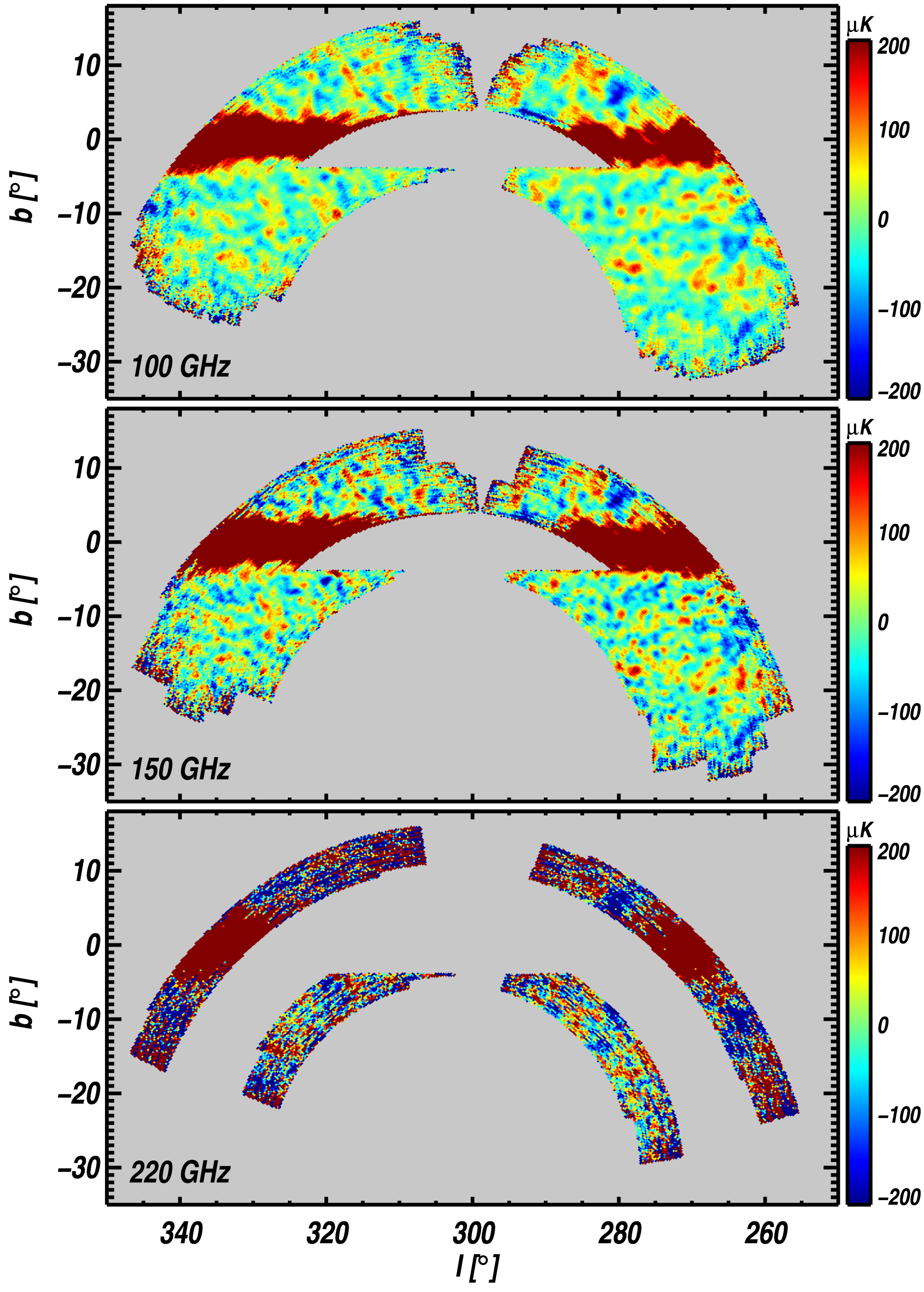

Figure 1.6: BICEP intensity maps from all three seasons co-added over all four boresight angles at 0.25° `Healpix` resolution, in Galactic coordinates, at 100, 150, and 220 GHz from top to bottom respectively. The color scale has been chosen to emphasize the CMB anisotropy, which is visible in all three bands.

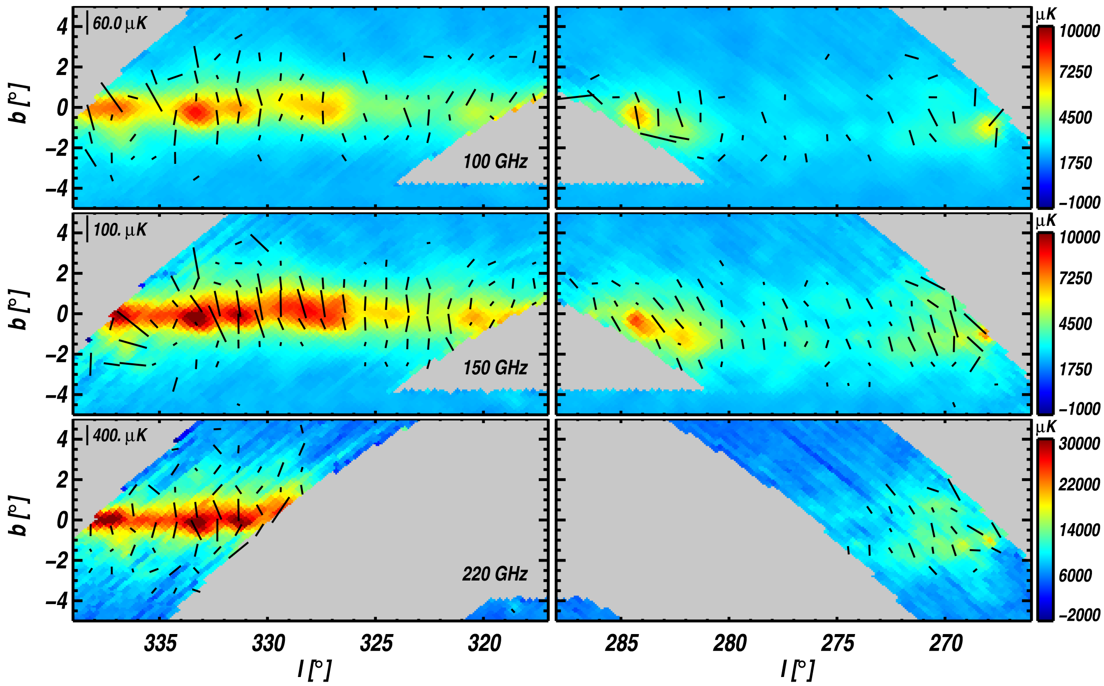

Figure 1.7: BICEP intensity maps from all three seasons co-added over all four boresight angles with polarization vectors, in Galactic coordinates, at 100, 150, and 220 GHz from top to bottom respectively. The color scale is chosen to emphasize the emission in the Galactic plane. Polarization vectors are only displayed if the map pixel has a signal-to-noise ratio above 10 for the unpolarized intensity, I, and above 4 for polarized intensity, $P = p \times I$. Polarization vectors are predominantly perpendicular to the Galactic plane, implying that the magnetic field in the medium sampled by BICEP is parallel to the plane of the Galaxy. While intensity values can't physically be negative, the observing and analysis strategy filters the maps, causing negative values in the maps as can be seen near higher Galactic latitudes. To convert thermodynamic temperature units, μK, to differential intensity units, MJy/sr, multiply the 100, 150 and 220 GHz map values by 0.22, 0.40, 0.48 respectively.

The main polarization quantity studied is q as opposed to p or u, because p suffers noise bias being a positive definite quantity, and there is relatively little signal in u.

It is known that the observed polarization fraction from an astronomical source will be lessened by disorder in the magnetic field. To explore the Galaxy's magnetic structure, BICEP maps are fit to a phenomenological power law as:

$$q = q_{(I_{median})} \times \left(\frac{I}{I_{median}}\right)^{\eta} \tag{1.15}$$

where I_{median} is calculated from the map pixels in the 220 GHz analysis region, η is the slope parameter and $q_{(I_{median})}$ is the overall polarization fraction normalization parameter. The parameter, η, approximately represents the disorder in the magnetic field which is traced by millimeter-wave polarization.

The simplest Galactic magnetic field model to compare BICEP data to is one where $\eta = 0$, which has no disorder in the field. The measured polarization is a direct imprint of the intensity signal, related by a constant polarization factor q_0.

Other models describe the Galaxy's magnetic fields as being much more random. For example, a simple toy model for this case is one where the Galaxy is uniformly thick and consists of a constant polarized (q_0) diffuse component emitting with a weak intensity, I_0. Scattered throughout are dense star forming regions with random polarization angles which, when integrated along the line of sight or over the beam width, will integrate down to very low net polarization but will contribute to total intensity with I_1. In this case the polarization fraction would be:

$$q = \frac{q_0 \, I_0}{I_0 + I_1} \propto I^{-1}. \tag{1.16}$$

In this case $\eta = -1$, implying increasing dust column density that contributes no additional polarized intensity.

While both of the models here are strictly empirical, other studies have used similar methods. These methods involve fitting starlight polarization to a similar power law model; the exponent for polarization by absorption is related to the power law exponent for polarization by emission in the millimeter-wave band by $\eta_{em} = \eta_{abs} - 1$. Fosalba et al. (2002) fit starlight polarization data to p vs. $E(B-V)^{\eta_{abs}}$ finding $\eta_{abs} = 0.8$, which implies $\eta_{em} = -0.2$. Fosalba et al. (2002) then relates this fit parameter to a magnetic field model from Burn (1966) using the assumption above, namely that the polarization fraction is a product of the ratio of uniform and random components of the magnetic field. Jones (1989) fits starlight polarization data to p vs. $\tau_K^{\eta_{abs}}$, finding $\eta_{abs} = 0.75$, which implies $\eta_{em} = -0.25$. Jones (1989) takes the fitting process a step further and runs Monte Carlo simulations for observing Galactic magnetic field arrangements with varying level of randomness and claims a more accurate fit than using an analytic equation. Lastly, these other works study polarization fraction p, while in this paper q is studied, which does not necessarily follow the same power law trend as p. For example, a Galaxy with completely random magnetic field directions would predict a polarization fraction given by a power law exponent of $\eta = -0.5$; however in this scenario, q would oscillate about zero and give an average $\eta = 0$.

1.4.3 Noise and Systematic Error Evaluation

To confirm the integrity of the maps presented here, they were cross-checked with an independently written pipeline. The two pipelines produced nearly identical `Healpix` maps, reducing the possibility of coding errors or other non-physical errors. For example, taking the difference between the two pipeline's 150 GHz Q maps gave a pixel *rms* level five times smaller than the noise level, with no obvious signal features left.

The data have $1/f$ noise from atmospheric fluctuations, electronic readout drifts, thermal instabilities, and scan-fixed contamination. The polynomial subtraction removes most of this contamination but the polynomial masking allows some of this noise to leak back into the Galaxy maps. The polynomial fitting is only applied to data outside of the Galactic plane mask, causing χ^2 not to be minimized with respect to the noise within the mask. However, since the noise is correlated, the polynomial fit well-approximates the noise close to the mask edges, but decreases in effectiveness the further the pixels are from the edge of the mask. Therefore, the larger the mask used, the worse the polynomial fit inside the mask approximates the noise, because there is a larger gap over which the polynomial must be extrapolated. The smaller the mask used, the better the fit approximates the noise; however, this also increases the filtering of the signal in the plane.

Optical imperfections, such as beam mismatch, cross-polarization, depolariza-

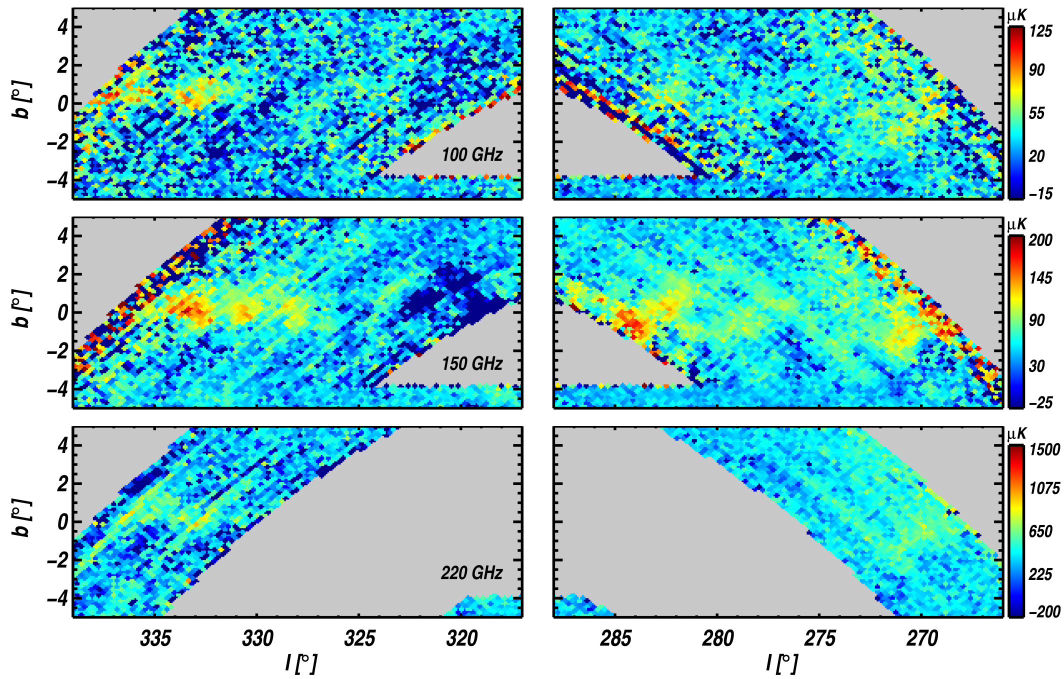

Figure 1.8: BICEP U polarization maps from all three seasons co-added over all four boresight angles, in Galactic coordinates, at 100, 150, and 220 GHz, from top to bottom respectively. Galactic $+U$ polarization corresponds to a polarization vector in the $+b$ and $+\ell$ direction. Power can be seen in all three bands indicating areas where the Galactic magnetic field is not exactly aligned with the Galactic plane. The significant detection of negative U power in 150 GHz map at Galactic Longitude 322° is physical and not an artifact of filtering or other systematics.

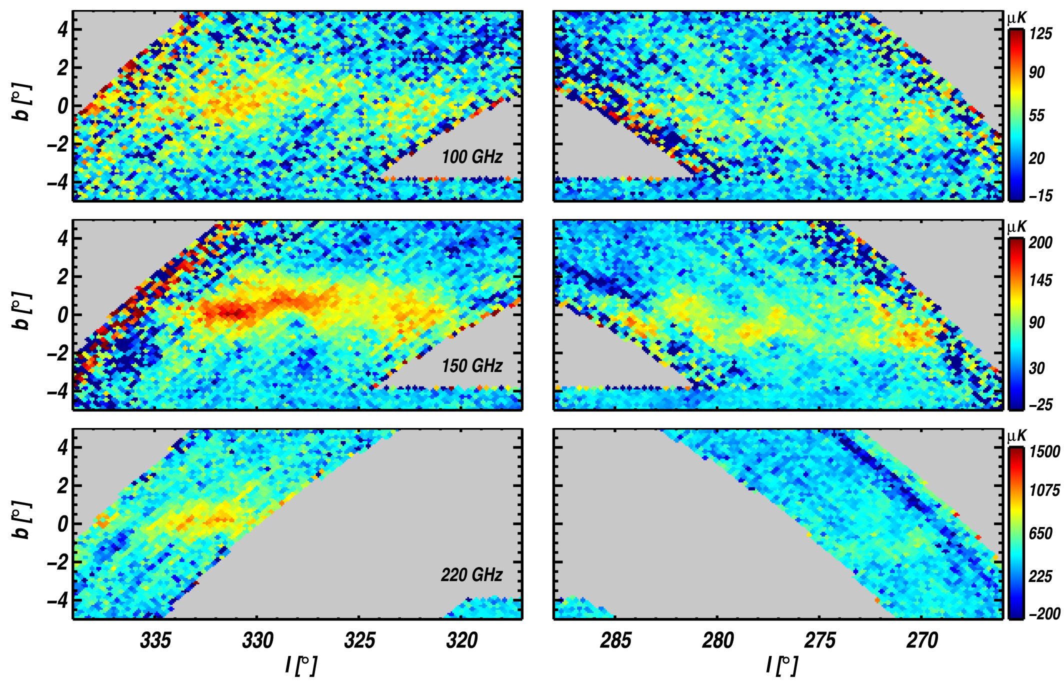

Figure 1.9: BICEP Q polarization maps from all three seasons co-added over all four boresight angles, in Galactic coordinates, at 100, 150, and 220 GHz, from top to bottom respectively. Galactic $+Q$ polarization (red), corresponding to a vector that is perpendicular to the Galactic plane, dominates the maps.

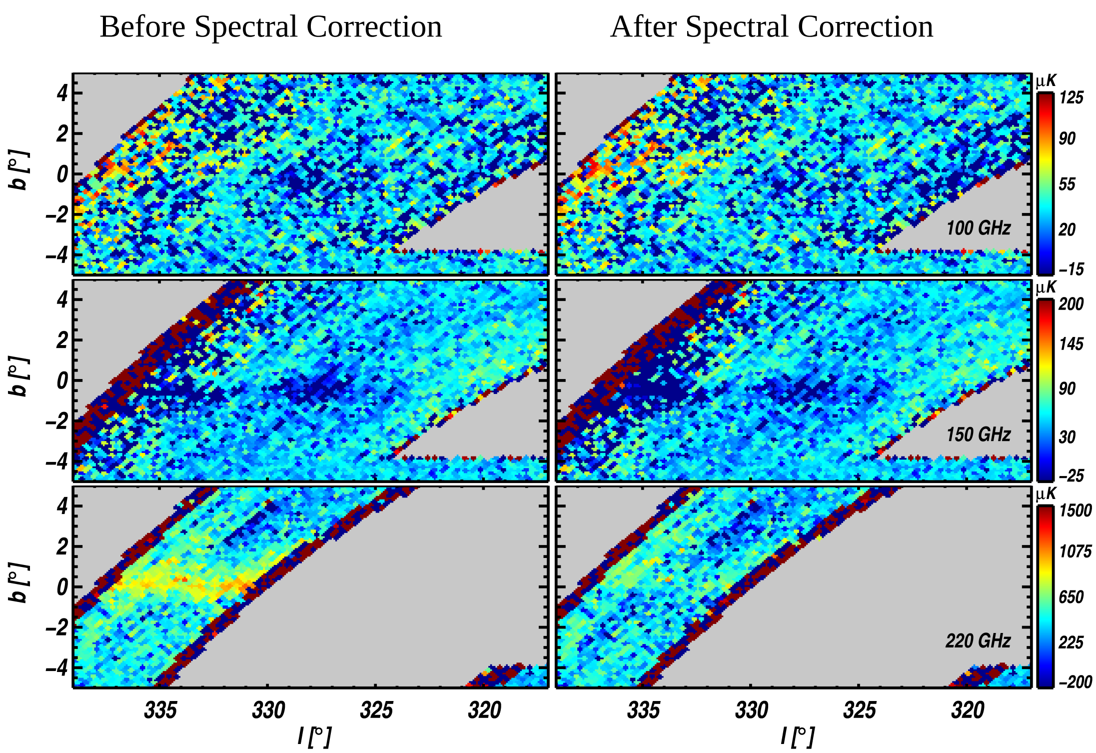

Figure 1.10: Difference between Q Gal-bright maps made at boresight rotation angles {0, 315} and {135, 180}, divided by two, in Galactic coordinates for 100, 150, and 220 GHz from top to bottom respectively. The left hand plots are the difference maps uncorrected for spectral gain mismatch while the right hand plots have been corrected. Some of the features in these raw jackknife maps are due to differences in integration time and polarization coverage such as near the edges of the observing area. Other features, such as the negative excess centered near $\ell = 327^\circ$ and $b = 0^\circ$ in the 150 GHz map arise from scan-fixed or telescope systematic contamination. Most of the excess at 220 GHz is corrected by accounting for spectral gain mismatch while there is marginal change in the 100 and 150 GHz maps. There is some faint striping nearly orthogonal to the Galactic plane in the 150 and 220 GHz maps from residual $1/f$ noise leaking through the polynomial mask.

tion, and sidelobe response can cause systematic changes in the maps. These "telescope systematics", studied and characterized by Takahashi et al. (2010) for the CMB B-mode analysis, are controlled very well partly because of BICEP's simple, compact design. The overall magnitude of the telescope systematics and $1/f$ leakage in the Galactic maps are estimated by splitting the data into two halves, according to the telescope's orientation angle about the boresight. Angles 0° and 315° are called "boresight map A", while 135° and 180° "boresight map B". Since there are only two 220 GHz feeds, 220 GHz boresight map A is determined from a single feed, while 220 GHz boresight map B is determined from the other feed. This split is the most probative for the polarimeter because the Galactic sky coverage in each half comes mostly from a different set of feeds, taken at different times, under different weather conditions, and with the telescope oriented differently with respect to gravity. For this study the two BICEP boresight maps per frequency band are studied in this paper, which can be used to gauge the general level of residual systematic contamination in the maps.

1.4.3.1 Boresight Difference Maps

To illustrate the efficacy of the boresight difference maps, Figure 1.10 shows the difference between the two groups for the Q maps for all three bands, both before and after spectral gain mismatch correction. This is a qualitative jackknife test, as it does not test quantitatively against the expected noise or signal leakage. Figure 1.10 shows some power in the Q boresight map jackknife at all three bands, which is representative of all the Galactic jackknife maps. The residual power in the 220 GHz raw maps was used to validate the spectral gain mismatch model and the post-corrected maps show the level of correction achieved. While there is still some residual power in the 100 and 150 GHz channels, it does not affect the results claimed in this paper. The post-corrected 220 GHz maps give consistent polarization results between the two detectors; however, there is still uncertainty in the spectral gain mismatch parameter due mostly to changes in atmospheric conditions.

1.4.3.2 Uncertainty due to Spectral Gain Mismatch

Simulations were run to show the level of uncertainty induced on the quantitative parameters analyzed in this paper due to uncertainty in the spectral gain mismatch calculation. Two sets of simulations were run; one based on the uncertainty in the atmospheric conditions and one based on the uncertainty in the measured spectral response.

The average spectral response and measurement uncertainty were calculated from the eight separate spectral response runs per detector (Section 1.3.3). The uncertainty in atmospheric conditions was derived from computing the spectral gain mismatch using Austral winter and summer conditions, using a low precipitable water vapor (pwv) value, a median value, and a high value for different observing angles. The mean and standard deviation of these conditions were computed, where the mean values are the nominal spectral gain mismatch and the standard deviation is used as the uncertainty. The pwv conditions used were quite conservative and actual observing conditions most likely had a much smaller range of weather conditions.

Simulations were performed by generating random spectral gain mismatch parameters for each feed, creating a modified list of spectral gain mismatches. Using the modified list, the entire set of mapmaking steps of Section 1.3.4 and 1.3.5 are repeated, and $q_{(I_{median})}$ and η are found. This procedure was repeated ten times for both the atmospheric and spectral response measurement uncertainties, giving average parameter values and an uncertainty on each average.

The percent error computed from the simulations based on different atmospheric conditions is $\frac{\delta q_{(I_{median})}}{q_{(I_{median})}} = [1.0\%, 1.3\%, 3.6\%]$ and $\frac{\delta\eta}{\eta} = [8.9\%, 15.\%, > 100\%]$ for 100, 150, and 220 GHz bands. The uncertainty from spectral measurement errors is $\frac{\delta q_{(I_{median})}}{q_{(I_{median})}} = [0.2\%,\ 0.2\%, 0.3\%]$ and $\frac{\delta\eta}{\eta} = [2.4\%, 1.8\%, 41.0\%]$ for 100, 150, and 220 GHz bands. The uncertainty on the 220 GHz parameters are larger than the other two bands because the two 220 GHz feeds have the largest spectral gain mismatch and the smallest measured η value. The spectral measurement uncertainties are five to ten times smaller than the uncertainties from the various weather conditions. The combined spectral gain mismatch uncertainties are relatively minor for the determination of $q_{(I_{median})}$; however, these uncertainties provide the largest single source of error on η at all three bands.

1.4.3.3 Uncertainty due to Polynomial Filtering

Polynomial subtraction removes signal as well as noise, causing systematic filtering effects. To estimate the filtering effects, simulations are carried out to compare maps before and after various filtering strategies as well as to compare to the real data. The general algorithm for the simulation was to use an intensity map and Galactic model parameters to generate I, Q, and U maps. These maps are then filtered in various ways and compared to the original maps and actual data filtered in a similar manner to find the resulting effects and uncertainties of filtering on the maps.

The simulations used WMAP 94 GHz DA 1 (Section 1.4.4) and FDS (Finkbeiner et al., 1999) to make two separate intensity maps per frequency band. The WMAP intensity map was first deconvolved with the beam function provided by WMAP and convolved with the BICEP Gaussian beam at a given band. Then, the maps were downsampled from 0.125° `Healpix` pixels to 0.25° pixels. An additional simulation was carried out using the higher resolution pixels, but this caused less than a 5% change in the resulting simulation values. For the FDS simulation, tools are provided to predict the power over the entire sky at an arbitrary frequency[2]. A full sky prediction is made at 0.016° `Healpix` pixel resolution for each BICEP band for each measured spectral bandpass data point (approximately 200 separate frequency points per band), which can then be summed together to make three full sky simulated BICEP band dust maps. The maps are convolved with the BICEP beam at each band and downsampled to 0.25° `Healpix` resolution.

Using these intensity maps, simulated polarization maps are generated using Equation 1.15 with parameters found from the BICEP maps. For the simulations the polarization fraction magnitude was always chosen to be 2% at the median intensity and the power law exponent η was varied between -0.75, -0.50, and -0.25. The polarization angle is set to 7°, the approximate average polarization angle found in the 220 GHz analysis region, which sets the value of U in the simulation. Using this model, the polarization fraction has the possibility of taking unphysical values, therefore, the maximum polarization fraction allowed is set to 10%. A value of 25% was also implemented but this did not change the results appreciably.

[2]http://astro.berkeley.edu/dust/index.html

BICEP pointing was used to extract I, Q, U values from the simulated maps to generate the simulated timestreams. The simulated timestreams were processed with the same filtering as described in Section 1.3.4, leading to identical coverage as the real data. In addition to the nominal 4° polynomial mask, separate simulations were performed using 2° to 9° polynomial masks for the WMAP simulations. Mask values above 5° gave marginal improvements in recovery of studied parameters but these higher mask values also decreased the amount of mapped area and also created more map pixels near the edges of the observation area with abnormal properties. Polynomial masks ranging from 2° to 5° were also applied to the real data. Then, for each map, the same pixels were fit to Equation 1.15 and the average angle and standard error in the angle were computed.

Figure 1.11 shows the results of the WMAP simulation (FDS simulation results not shown) and compares the resulting average map parameters to the real data. The changes in derived parameters due to polynomial-mask size are generally smaller than the changes in the parameters between filtered and unfiltered maps. The level of filtering effects on the maps and uncertainty in the map correction factor can be judged from the different simulations and the comparison to the real data. The filtering effects and correction factors are smaller and better understood for some parameters such as the intensity I, but are larger and not as well understood such as for η. The conclusion from the simulations and comparison to the real data in Figure 1.11 is that while the BICEP maps have been systematically filtered, the magnitude of this effect is small enough not to affect the general results from the analysis of the maps. However, these effects do prevent additional quantitative analysis of the maps beyond what is performed in this paper as a whole.

The uncertainty in the filtering correction for the intensity data is $\pm 5\%$, which comes mostly from the variation of results from the WMAP and FDS simulations rather than variations within the simulation parameters. The uncertainty in the polarization filtering correction is only known to $\pm 25\%$, which comes equally from variations of simulation polarization parameters across each band and from the difference between WMAP and FDS simulations. The average correction factors for I, $q_{(I_{median})}$, η calculated from these simulations for the 220 GHz analysis region are 11%, 37%, 39%. The average correction factor for computing the average q is 23%. These values are used to correct results for further analysis in this paper.

1.4.3.4 General Map Noise

Background photon and detector noise dominates the white noise floor in the maps. The average polarization map pixel sensitivity can be calculated by taking the calibrated timestreams and computing the periodogram for each half scan. The average periodogram per feed for each frequency band is then calculated (Figure 1.12). The pair-sum data suffers from increasing levels of $1/f$ atmospheric contamination from 100 GHz to 220 GHz. Most of the $1/f$ atmospheric noise is removed from the polarization data by pair differencing within a feed, resulting in nearly white noise at all three bands above 0.1 Hz. Averaging the pair-difference periodogram from 0.1 Hz to 1.0 Hz (corresponding to an angular size of $\approx 0.5^{\circ} - 5^{\circ}$) gives Noise Equivalent Temperature (NET) per detector values of 520, 450, and 1040 $\mu\mathrm{K}\sqrt(s)$ for 100, 150, and 220 GHz respectively. After accounting for polarization efficiencies, these correspond to NEQ per feed values of 410, 340, and 880 $\mu\mathrm{K}\sqrt(s)$ for 100, 150, and 220 GHz respectively. There is very good agreement between the noise estimate from the periodograms in Takahashi et al. (2010), which used two years of third-order polynomial filtered data from the CMB region, and this calculation using three years of data from the Gal-bright and Gal-weak regions that has second-order polynomial filtering.

The noise in a given map pixel is calculated using the NEQ per feed values, the integration time per 1° pixel, and assuming the integration time is split evenly between the Q and U maps. The average sensitivity for Q or U map pixels in the 220 GHz analysis region is 2.8, 2.8, 16.0 μK-rms for 100, 150, and 220 GHz respectively.

Another method to gauge the noise in the maps is to split the data in half and take the difference, which cancels off the signal and leaves the residual noise. Maps were made from right going and left going scans separately, and then differenced. This split is used to test for detector time constant mismatch or general telescope thermal effects; however, it tends to be one of the least probative for BICEP because the two halves are taken at nearly the same time, under the same weather conditions, and with the same set of feeds. Pixels from the Q and U differenced maps, with a significant

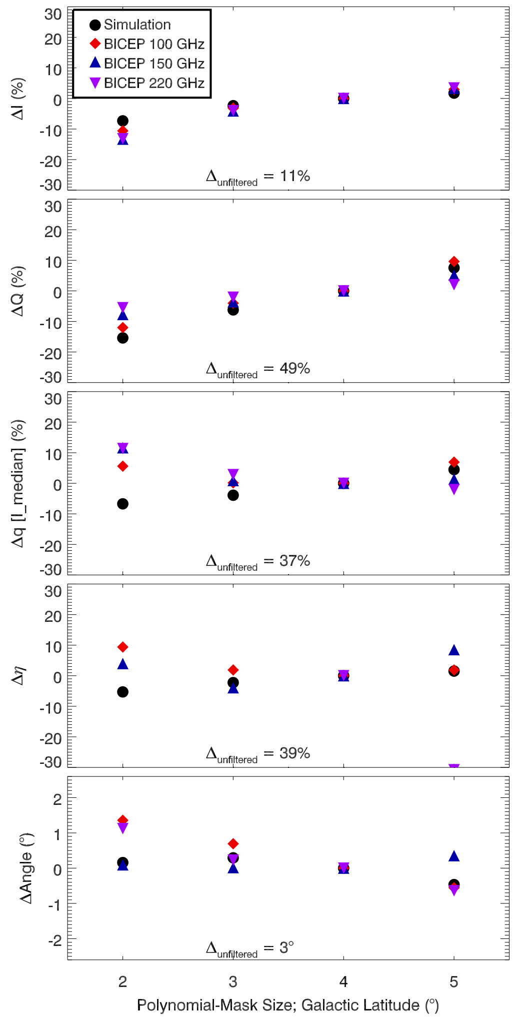

Figure 1.11: Fractional change in the average map parameters vs. polynomial-mask size for 100 GHz (red diamonds), 150 GHz (blue triangles), 220 GHz (purple upside-down triangles), and the 150 GHz WMAP simulation (black circles) showing the size of, and general level of uncertainty in, the filtering effects on the maps. The parameters studied are intensity I, Q polarization, Q polarization fraction at the median intensity, η, and polarization angle. The units are relative percent difference (angular difference for the bottom plot) between a given average map parameter, X, and the 4° polynomial-mask average map parameter, X_{4°; $\Delta X = (X/X_{4^\circ} - 1)$. At the bottom of each plot is the fractional difference, $\Delta_{unfiltered}$, in the parameter value derived from the average values of unfiltered simulation maps compared to that from filtered simulation maps with a 4° polynomial-mask.

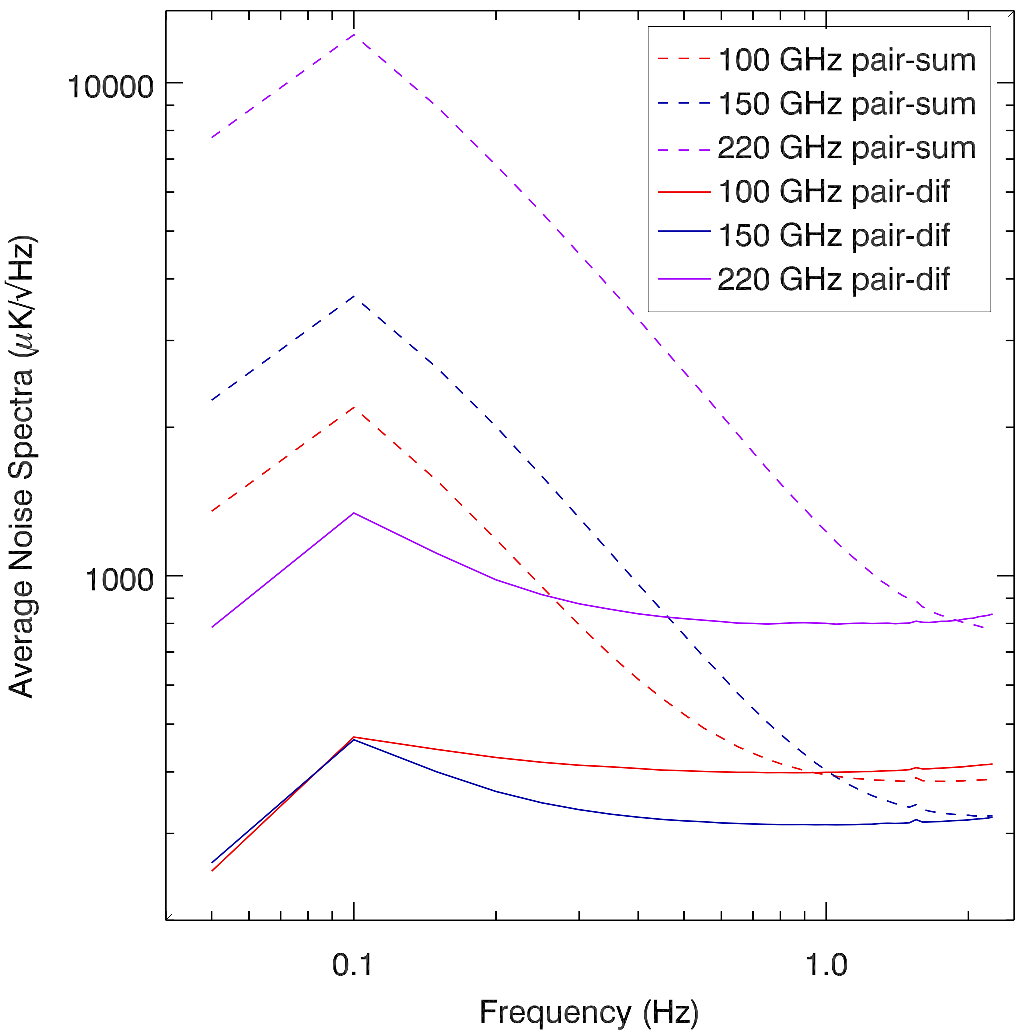

Figure 1.12: Average periodogram for the pair-sum and pair-difference timestreams from all of the Galactic scans, after second-order polynomial removal. The second-order polynomial filtering is apparent at 0.05 Hz (the lowest frequency bin), where the power is lower than the white noise level. The rise at high frequency is due to the deconvolution of the detector and system time constant.

amount of integration time, were multiplied by the square root of integration time per pixel and the standard deviation of all the pixels was computed. This was done for all the pixels and the 220 GHz analysis region pixels. Using all the pixels, the average noise values are 420, 320, and 930 $\mu\mathrm{K}\sqrt{s}$ for 100, 150, and 220 GHz respectively, which are comparable to the NEQ per feed noise estimate from the periodogram method indicating good agreement between the two methods. The noise for the 220 GHz analysis region pixels as compared to the entire map is 20%, 40%, and 45% higher for 100, 150, and 220 GHz respectively, due to excess $1/f$ noise leaking inside the mask.

1.4.4 WMAP 94 GHz Band Comparison

WMAP is a millimeter-wave satellite that has ten differencing assemblies (DAs), all producing I, Q, and U maps over the whole sky using one channel at 23 GHz, one at 33 GHz, two at 41 GHz, two at 61 GHz, and four at 94 GHz. The combination of BICEP data with WMAP data provides frequency coverage in the 220 GHz analysis region from 23 to 220 GHz. As an important cross check on the validity of the BICEP observations, a direct comparison is made between the WMAP 94 GHz band and BICEP 100 GHz intensity maps.

There are two systematic differences that prevent direct comparison. First, the BICEP beam is a different size than the WMAP beam and the maps are filtered as described in Section 1.4.2. Therefore, to make a direct comparison, each WMAP DA map is smoothed to BICEP's beam resolution, sampled into BICEP-like timestreams, and filtered. For consistency, sampling of the WMAP maps was performed using both 0.0125° maps, and the nominal 0.025° maps. Since both sets of maps are filtered, there is no need for systematic filtering correction in this case.

Secondly, there is a difference in spectral bandpass between the two experiments. BICEP is calibrated to WMAP by comparing the CMB fluctuations in the low astronomical foreground region. However, Galactic emission has a different spectrum than the CMB, and combined with the different bandpass response, this could cause a systematic difference between the two experiments. In a very similar manner to the spectral gain mismatch calculation in Section 1.3.3, the expected miscalibration is calculated using the average BICEP 100 GHz spectral response, the average WMAP 94 GHz band spectral response, the CMB anisotropy spectrum as seen from space and from the South Pole, and the typical Galactic source spectrum as seen from space and the South Pole.

Different atmospheric observing conditions were simulated for BICEP(Section 1.3.3) to compare to WMAP, which is in space and is not affect by a change in atmospheric conditions. The mean and standard deviation of spectral gain mismatch from the different atmospheric conditions between BICEP 100 GHz and WMAP 94 GHz band is $0.322\% \pm 0.001\%$ (the positive sign indicates an increase in BICEP power relative to WMAP). The small difference results from the shape of the emission spectra being nearly identical for the CMB and the typical Galactic source spectrum at this particular band (this is not true at other bands), so even though BICEP and WMAP have relatively different bandpasses, there is no spectral gain mismatch between the experiments. The extremely small standard deviation on this quantity results from the insensitivity of the BICEP 100 GHz band to different atmospheric conditions, especially the emission lines outside the band. Instead of using the average 100 GHz spectra, this calculation was repeated for each individual detector's spectral response giving an average and standard deviation of anomalous gain factors of $0.315\% \pm 0.055\%$, consistent with the first method.

The data from the two experiments were compared in a similar manner to the absolute calibration routine from Chiang et al. (2010), except the comparison was performed using maps (called "MAP") instead of spherical harmonic transform coefficients ($a_{\ell m}$). The anomalous gain factor comparing the BICEP 100 GHz and WMAP 94 GHz band intensity maps is calculated as

$$g_{ijk}^{anom} = \frac{\langle MAP_{\mathrm{WMAP_j}} \times MAP_{\mathrm{BICEP_i}} \rangle}{\langle MAP_{\mathrm{WMAP_j}} \times MAP_{\mathrm{WMAP_k}} \rangle} - 1 \tag{1.17}$$

where the angle brackets represent a weighted average of the 220 GHz analysis region pixels using the BICEP integration time as the weights. The index (i) for BICEP corresponds to the two boresight maps and the indices (j,k) for WMAP corresponds to the four DAs at 94 GHz where $j \neq k$ so the noise in a given map is not rectified. As a consistency check on this method, the gain was computed for the CMB observing region and compared to the absolute calibration numbers from Chiang et al. (2010), which found the gains using the angular power spectrum, gave consistent results. The two boresight maps give values of 5.0% and 4.7% gain increases using the 0.25° maps and 4.2% and

4.0% gain increases using the 0.125° maps. Each has a 0.5% statistical error derived from using the different combinations of WMAP 94 GHz band DA maps.

To check the uncertainty based on pixel selection or sky variance, a simulation was done using all pixel values $|b| < 3°$ in the BICEP observing region (335 one degree pixels) for the 0.125° maps. For each of 1000 different trials, 53 pixels were chosen at random and the anomalous gain was computed. The mean and standard deviation of the distribution gave 3.1 ± 2.1% and 2.5 ± 1.9% for the two boresight maps. For comparison, the same procedure was repeated for the 253 one degree pixels between $-3°$ and $-6°$ in Galactic latitude giving anomalous gain values of 1.0 ± 8.5% and -5.0 ± 6.5%

Chiang et al. (2010) quotes the absolute gain uncertainty to be 2% for the BICEP maps, which decreases the relative significance of the anomalous gain factor found here. The difference in anomalous gain factor due to the bandpass differences was calculated to be a very small; however, this calculation used a simple two-component continuum Galactic spectrum. The real Galactic spectrum is undoubtedly more complicated, which could lead to a larger spectral factor difference. Another likely cause of anomalous gain is from systematic uncertainties in the processing of raw to BICEP-filtered WMAP maps (Section 1.4.2), either from the beam correction or flat interpolation procedure. Regardless of the underlying cause, the 4% gain difference does not represent a significant detection of a deviation between the two experiments in the Galaxy. A larger difference was found between WMAP and QUaD (Culverhouse et al., 2010), despite the similarity between the BICEP and QUaD instruments and analysis approach. However, QUaD's high-frequency cutoff is higher and low-frequency cutoff lower than either BICEP or WMAP, making it sensitive to certain emission lines to which BICEP and WMAP are insensitive.

1.4.5 Intensity vs. Frequency

By studying the spectrum of the unpolarized and polarized emission for a given point on the sky, it is possible to understand the composition of the ISM across the sky. The spectral response plots of intensity vs. frequency can show the fraction of dust and synchrotron in the Galactic plane. WMAP provides a vast amount of information on this topic; however, their highest frequency band still has an appreciable amount of synchrotron emission. Above 150 GHz, most Galactic emission comes from dust, which is where BICEP's 150 and 220 GHz channels add unique information.

A common unit for distributed astrophysical millimeter-wave emission is differential intensity as opposed to thermodynamic temperature, where the conversion factor from thermodynamic units can be calculated as:

$$dI = \left.\frac{dB}{dT}\right|_{2.725\ \mathrm{K}} \times dT,$$

and B is the Planck blackbody function. The derivative with respect to temperature is:

$$\frac{dB}{dT} = \frac{2k_B\nu^2}{c^2}\frac{z^2e^z}{(e^z-1)^2}; \text{ where } z = \frac{h\nu}{kT}.$$

Using the values of the physical constants and the BICEP band centers, the conversion factors are:

$$\frac{dB}{dT} = 0.22, 0.40, 0.48\ \frac{\mathrm{MJy/sr}}{\mathrm{mK}}, \tag{1.18}$$

for 100 (95.5), 150 (149.8), and 220 (208.2) GHz bands respectively, where the true band centers are shown in parenthesis. Similarly, the conversion values are 0.016, 0.033, 0.049, 0.10, 0.22 for WMAP's 23 (22.8), 33 (33.0), 41 (40.7), 61 (60.8), and 94 (93.5) GHz channels and are used in Table 1.2. Figure 1.13 and the subsequent spectral analysis in this section uses BICEP, WMAP, and FDS data in these differential intensity units.

Figure 1.13 shows a plot of the mean and standard error of the mean intensity of the analysis area pixels from both BICEP and WMAP, calculated from each of the ten WMAP DAs and two boresight maps for BICEP's three bands in differential intensity units. BICEP maps have been filtered by the mapmaking process, systematically lowering the intensity values. To correct for this, each BICEP point and error bar has been increased by 11% (Section 1.4.3.3). The error bars for the FDS points and other bands come from sky variance, not measurement errors. BICEP has two data points per band that are computed from the two boresight maps. The fact that two data points are nearly identical indicates that the systematic uncertainties are not the dominant source of uncertainty for the average intensity of the maps, even for the 220 GHz channels, consistent with the discussion in Section 1.4.3. WMAP points are from each DA separately, which can indicate the approximate level of residual systematic uncertainty in a given band.

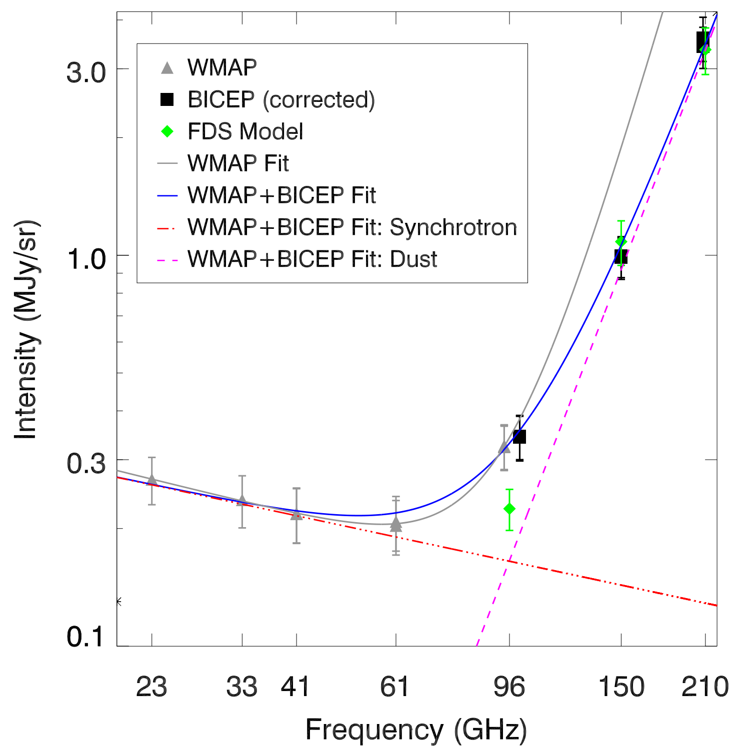

Figure 1.13: The mean intensity as a function of frequency for the 220 GHz analysis region for WMAP's ten DAs (gray triangles) and BICEP's two boresight maps for each of the three bands (black squares). BICEP's 100 GHz points are shifted to the right 5 GHz from the calculated band centers for clarity. WMAP points come from raw, unfiltered maps, downsampled to 1° resolution. The noiseless FDS model 8 (Finkbeiner et al., 1999) predicted dust maps (green diamonds) have been beam smoothed, spectral bandpass filtered, and downsampled to 1° to match BICEP's bands but not polynomial filtered. The fit to Equation 1.19 using only WMAP points (gray) gives a dust spectral index $\zeta_d = 5.06$, larger than when BICEP data (blue) are included, which gives $\zeta_d = 3.70$. The pink and red dashed lines are the individual positive and negative spectral index components from fitting to both WMAP and BICEP points.

The points in Figure 1.13 are fit to

$$I(\nu) = A_s\, \nu^{\zeta_s} + A_d\, \nu^{\zeta_d}, \tag{1.19}$$

a simple two-component power law model where $A_{s,d}$ are the magnitudes of the synchrotron and dust components and $\zeta_{s,d}$ are the power law exponents for the synchrotron and dust components. BICEP's points and error bars have been increased by 11% using the systematic filter correction found in Section 1.4.3.3. The best fit spectral index parameters and errors from using only the WMAP points in Equation 1.19 are $[\zeta_s, \zeta_d] = [-0.36, 5.06] \pm [0.02, 0.33]$, while if BICEP data is included then $[\zeta_s, \zeta_d] = [-0.39, 3.70] \pm [0.07, 0.11]$. For reference, FDS model 8 predicts $\zeta_d = 3.5$ in the frequency range 23 - 220 GHz in the same analysis region. From signal simulations, the uncertainty in systematic filter correction could be as large as 5%; however, this factor has a relatively minor effect on the fit. For example, a 5% uncertainty in this correction factor leads to an uncertainty in ζ_d of $\sigma_{\zeta_d} = 1\%$. This reduced sensitivity to input uncertainty is due partially to the non-linear nature of the fitting model but also due to the WMAP points not suffering from BICEP's filtering bias. Repeating the fit procedure with only one set of boresight maps, causes a change in ζ_d of $\sigma_{\zeta_d} = 2\%$. Splitting the map into the Gal-bright and Gal-weak regions gave $\zeta_d = [3.81, 3.27]$ with $\sigma_{\zeta_d} = [0.14, 0.15]$ indicating a difference in dust spectral index between the two regions at 2.7 sigma significance.

Therefore, in this case, the uncertainty in this fit itself is larger than the uncertainty due to systematic contamination from weather or telescope systematics which is larger than the uncertainty due to systematic filtering bias uncertainty. Analyzing the WMAP DAs separately is a way to include systematics from that experiment. However, the separation between points in any WMAP band (See Figure 1.13) is smaller than the uncertainty in the average value from that band, making systematics minimally important.

The simple two-component model fits the data well; however, additional components are not excluded. The plot shows the importance of measurements at higher frequency bands to fully understand the composition of the ISM. At 95 GHz, using the two-component fit parameters, dust makes up 51% of the total emission, while at 150 GHz it makes up 87% and at 220 GHz it makes up 97%. Finkbeiner (2003) gives a template for the full sky free-free emission based on H_α measurements. Taking their input map at 0.0625° resolution, downsampled to 1° resolution, converted to MJy/sr using the factors given in their table 1 at 100 GHz, the average map pixel value in the 220 GHz analysis region is 0.004 MJy/sr. Therefore, free-free is approximately 40 times smaller than either the dust or synchrotron component in BICEP maps. Further measurements at intermediate frequencies with finer spacing would also provide useful information about the transition from the synchrotron to dust dominated regime and give more information about other possible emission sources.

1.4.6 Polarization Fraction vs. Intensity

The Galactic magnetic field cannot be measured directly, therefore measurements of the field's effect on the intervening interstellar matter are crucial. The Galactic magnetic field produces polarization on large and small scales across the electromagnetic spectrum. Millimeter-wave polarization measurements probe emission that spans the full extent of the Galactic plane making it possible to exclude or motivate models for the Galactic magnetic field structure.

1.4.6.1 Polarization Fraction Data

One prediction of most Galactic magnetic field models is a trend of observed polarization fraction as a function of unpolarized intensity (Miville-Deschênes et al., 2008). To determine if there is a trend and what the nature of the trend may be, Figure 1.14 shows scatter plots of q vs. I for the various BICEP maps with two WMAP channels also shown for comparison. The plotted map pixels for both BICEP and WMAP are from the 100/150 GHz analysis area except for the 220 GHz map pixels, which use the 220 GHz analysis area. The error bars are calculated using the noise per band or DA and the integration time per pixel. Over-plotted on the scatter plots is the weighted linear least-squares fit following Equation 1.15 and the weighted mean q. Since the white noise floor value is used, all of the fits had reduced-χ^2 values much greater than one, indicating, to some extent, the total absolute uncertainty, including genuine variation about this trend across the sky. To better approximate the total absolute uncertainty in the resulting fit parameters, the uncertainty for each fit parameter is multiplied by the

$\sqrt{\chi^2_{reduced}}$, which are the error bars used in Figure 1.15. It is important to note that all of the BICEP maps detect a trend of decreasing polarization fraction with increasing intensity at more than three sigma; except BICEP 220 GHz, which has ten times fewer feeds than BICEP's 100 or 150 channels.

Figure 1.14 may not sufficiently support the hypothesis that there is a significant trend of decreasing polarization fraction with increasing intensity as opposed to a constant model for q. The difficulty is that the error in polarization fraction increases as the intensity value decreases because the uncertainty in q is proportional to I^{-1}, weighting the q values measured more strongly at higher I. However, the fact that there is a slope detected for all bands from 23 GHz to 150 GHz favors a sloped model over a flat one (See Table 1.2).

1.4.6.2 Model Fit Parameters

Figure 1.15 shows a plot of the fit parameters from Equation 1.15 for BICEP's two boresight maps (so there are two data points per band) and WMAP en DAs separately (which can give some idea of possible systematic uncertainty in a WMAP band). Table 1.2 lists the average parameters with uncertainties from three sources and band properties. One type of uncertainty is from the nonlinear regression covariance matrix, and these uncertainties have been increased by $\sqrt{\chi^2_{reduced}}$ to better approximate the true parameter uncertainty and include other noise sources such as genuine spatial variation across the sky. This type of error can be decreased by including more map pixels (possible at 100 and 150 GHz, but not at 220 GHz) or by increasing integration time or detector sensitivity.

Second, there is uncertainty due to the dispersion of different maps within a band, the two boresight maps for BICEP and the various DAs for WMAP. This uncertainty, especially for BICEP, indicates the approximate level of systematic contamination from the atmosphere, instrument thermal properties, and telescope systematics other than spectral gain mismatch. This type of uncertainty is prevalent at all three bands and hinders further quantitative analysis of η.

Third, there is uncertainty from spectral gain mismatch that is quantified from simulations in Section 1.3.3 using different atmospheric conditions. This type of un-

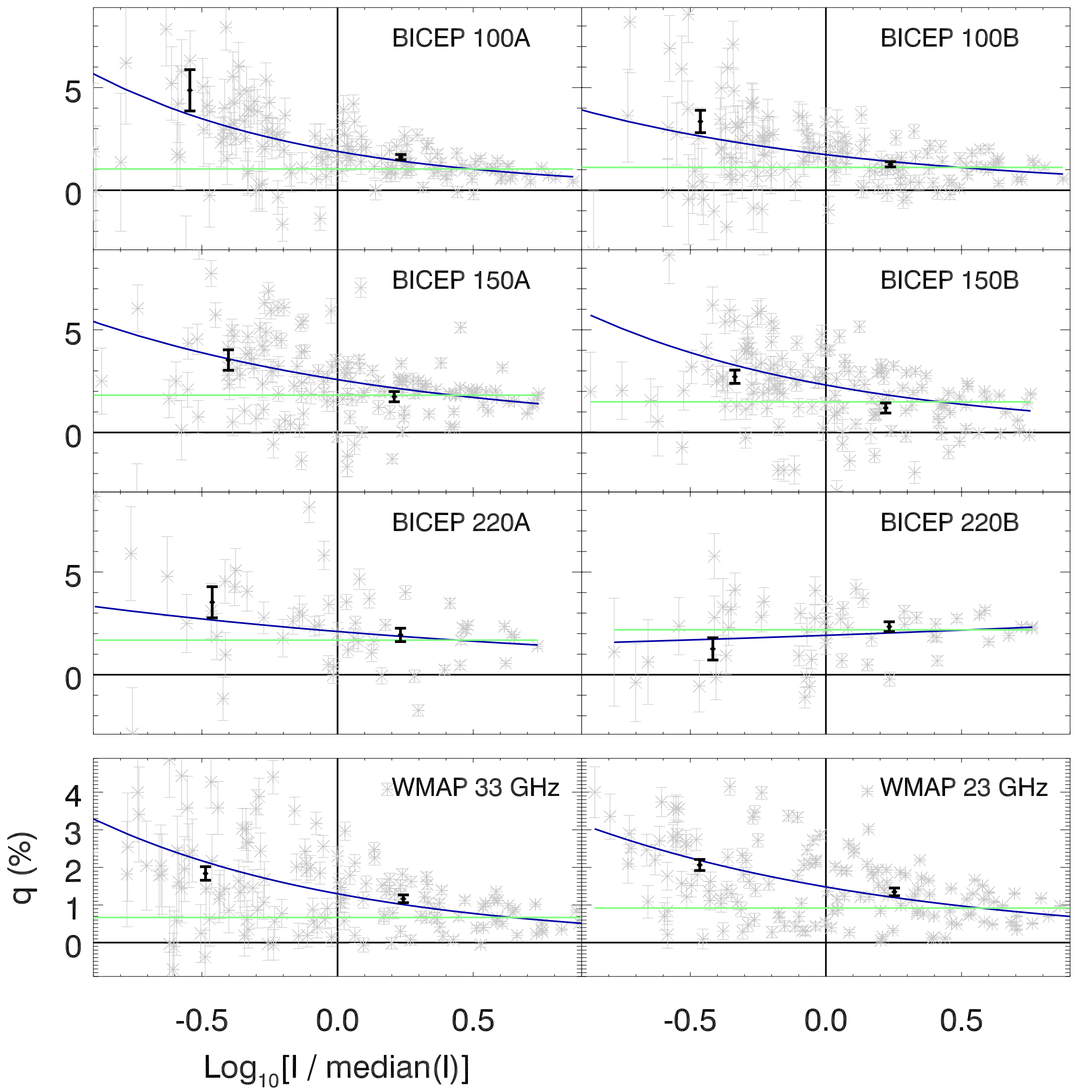

Figure 1.14: Polarization fraction, q, as a function of total intensity, I, using 147 one degree `Healpix` pixels (gray) from BICEP's three bands and two boresight maps along with WMAP 23 and 33 GHz bands. Out of the 147 pixels, 53 were used for the BICEP 220 GHz detectors because of the reduced observed region available at that band. The error bars are those due to the white noise in the maps and do not account for systematic errors due to the atmosphere, instrumental systematics, or filtering. The best fit line (blue) and constant model (green) are shown. The weighted average and uncertainty (black) of q for pixels less than the median value and greater than the median value clearly show the trend of decreasing polarization fraction as intensity increases.

certainty compared to the other two is only important at 220 GHz. Overall, there is a strong detection of $q_{(I_{median})}$ at all three bands and a significant detection of η at 100 and 150 GHz. There is not a detection of η at 220 GHz due to the combination of all three types of uncertainties exacerbated by the fact that BICEP only has two 220 GHz feeds for only two of the three observing seasons (See Appendix 1.8.1 for more information). Fitting for η is somewhat biased by the uncertainty in each pixel being proportional to I^{-1}, as the higher intensity pixels tend to dominate the fit. For example, it is difficult to tell whether a third parameter is needed to fit the data properly or whether there are separate effects happening for lower intensity pixels that some models would predict.

The top plot of Figure 1.15 shows a trend of increasing $q_{(I_{median})}$ vs. frequency with a sharp increase between 60 and 100 GHz. The two boresight map points per band are close to each other relative to the error bars indicating that the general level of systematic uncertainties is not the dominant uncertainty for $q_{(I_{median})}$. At higher frequencies where dust emission dominates the polarization fraction is above 2.5%, rather than below 1.5% at lower frequency where synchrotron emission dominates. The polarization fraction is nearly constant as a function of frequency in the dust dominated bands predicted by Hildebrand et al. (1999) and expanded upon by Hildebrand & Kirby (2004); Vaillancourt (2007); Draine & Fraisse (2009).

The observations of low polarization fraction for synchrotron or higher relative polarization fraction for dust may seem to be in contradiction to standard theory or observation (Rybicki & Lightman, 1979; Kogut et al., 2007); however, standard values are typical of high Galactic latitude regions, not necessarily in the Galactic plane. In addition, while synchrotron emission theory predicts a maximum polarization fraction near 75%, this has not been observed and values closer to 20% are commonly found off the plane where the emission efficiency should be the highest. Line-of-sight and beam size effects can further degrade the observed polarization fraction. Unpolarized emission mechanisms, such as free-free or spinning dust emission, contribute to the measured intensity but not the polarization also lowering the measured polarization fraction. Although Section 1.4.5 indicates that free-free does not contributes significantly for the BICEP bands and sky coverage region. Comparison to Figure 5 from Kogut et al. (2007), which shows a histogram of polarization fraction from pixels within the Galactic plane, shows the polarization fraction levels for the WMAP map pixels chosen here are in agreement with the lowest histogram bin of values within the Galactic plane. This is consistent with the BICEP observing region being very close to the Galactic center.

The bottom plot in Figure 1.15 shows η as a function of frequency; however, no model of this function is proposed in this paper. The two boresight map points per band show a comparable level of systematic error relative to the statistical error from the error bars. This is consistent with the discussion in Section 1.4.3 but is approaching an unacceptable level. One important point is that η changes the relative positions of the points in q vs. frequency. For example, since the average η value at 220 GHz is close to zero, the value of q at 220 GHz is relatively constant as a function of total intensity. Therefore, if q were evaluated at a very large value of total intensity and the plot of q vs. frequency remade, then it would appear that the polarization fraction increases relative to 150 GHz, even though the actual polarization fraction value at 220 GHz was nearly constant.

The weighted mean and standard error of η across all bands, assuming the BICEP data points are corrected for filtering, is $\eta = -0.47 \pm 0.05$. A simple, flat polarization model, $\eta = 0$, is ruled out as is the simple toy model of unpolarized embedded sources in a uniformly polarized background in the Galaxy, from Section 1.4.2, $\eta = -1$. A more complicated Galactic magnetic field model is needed to explain the measured value. A comparison of q and η between the Gal-bright and Gal-weak regions was performed, but there was no detectable difference between the two regions.

An inherent problem in analyzing the q vs. frequency plot is that it depends on the intensity value at which q is evaluated. While evaluating q at the median intensity gives a q value at a moderate level of intensity, other methods, such as computing the average of q, effectively results in finding q at the weighted mean intensity, as in Figure 1.16. The average has two advantages: a model including η is not needed and no value of I needs to be chosen at which to evaluate q. For this plot, the average from all the data is shown, neglecting different boresight angles and DAs. As opposed to Figure 1.15, this figure uses only map pixels from the 220 GHz region, simplifying the comparison of 220 GHz vs. the other bands. While the minimum q occurs near 40 GHz in this plot, depending on what value of intensity q is evaluated, this frequency can

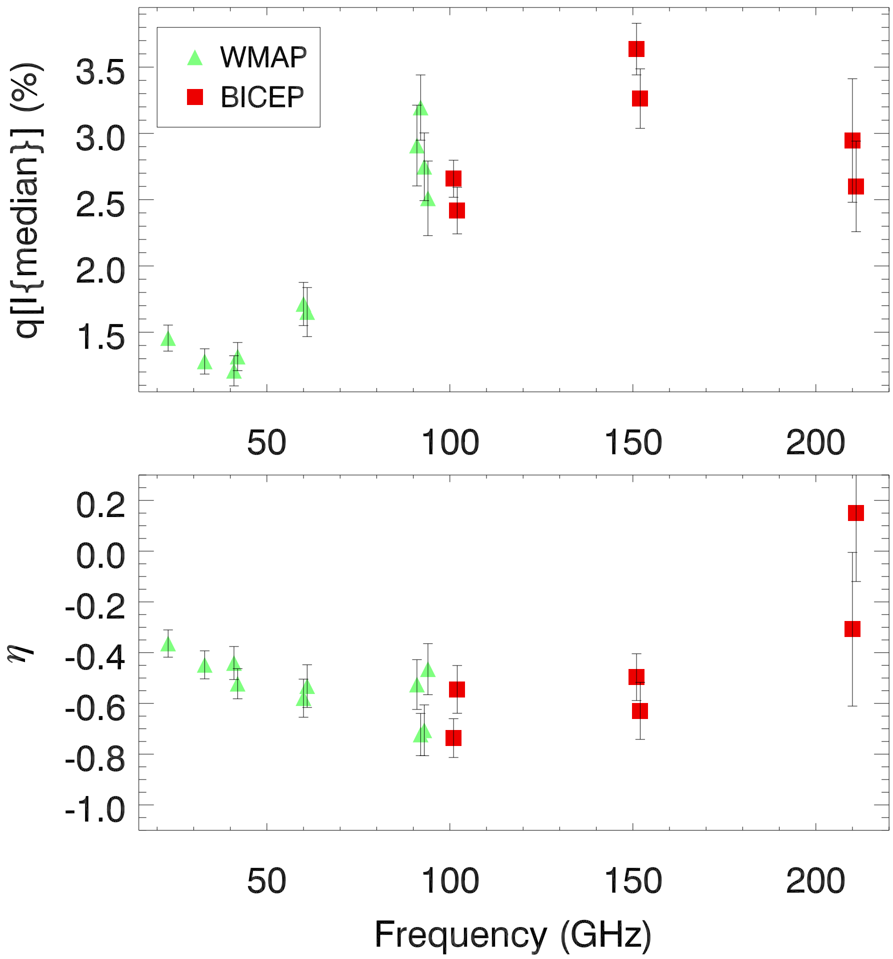

Figure 1.15: $q_{(I_{median})}$ and η as a function of frequency using BICEP (red) and WMAP (green) data. All frequencies use the 100/150 GHz analysis region except for 220 GHz, which uses pixels from the smaller 220 GHz analysis region. The error bars are the quadrature sum of fitting errors and the uncertainty from atmospheric conditions. BICEP's points have been corrected for filtering effects, increased by 37% and 39% for q and η respectively, based on signal simulations. The trend of increasing q with increasing frequency is apparent while there is no statistically definitive trend for η.

Table 1.2: Raw fit parameters for q vs. I

Average fit parameters and errors for Equation 1.15 using map pixels from WMAP and BICEP in the 100/150 GHz analysis region (except for 220 GHz which uses pixels from the 220 GHz analysis region). The BICEP fit parameters have been corrected for filtering effects (Section 1.4.3.3). The systematic errors "A" for the BICEP η parameters come from atmospheric uncertainty on spectral gain mismatch (Section 1.3.3). The statistical errors for both BICEP and WMAP come from the non-linear fits, while the systematic errors, "B" for BICEP come from the two boresight maps and for WMAP, the different DAs. The median intensities are set by taking the median value within the analysis region (53 pixels) at a given band and rounded to two significant figures.

Experiment Channel	Freq (GHz)	I_{median} (μK)	I_{median} (MJy/sr)	$q_{(I_{median})}$ (%)	Δq (%)	η	$\Delta\eta_{stat}$	$\Delta\eta_{sysA}$	$\Delta\eta_{sysB}$
WMAP K	23	8500	0.14	1.5	0.10	-0.36	0.05	N/A	N/A
WMAP Ka	33	3400	0.11	1.3	0.10	-0.45	0.06	N/A	N/A
WMAP Q	41	1900	0.093	1.3	0.11	-0.48	0.06	0.04	N/A
WMAP V	61	880	0.088	1.7	0.17	-0.56	0.08	0.02	N/A
WMAP W	94	800	0.18	2.8	0.27	-0.60	0.10	0.06	N/A
BICEP 100	95.5	800	0.18	2.5	0.16	-0.64	0.09	0.10	0.041
BICEP 150	149.8	1400	0.56	3.4	0.20	-0.56	0.10	0.07	0.063
BICEP 220	208.2	4400	2.1	2.8	0.40	-0.08	0.29	0.23	0.24

change. The polarization fraction approximately quadruples from 41 GHz to 95 GHz showing a relatively large dependence on frequency. No trend in polarization fraction above 100 GHz is visible, although the error bars do not exclude this possibility. In the end, Figure 1.15 demonstrates the systematics levels are small compared to the general trend of q vs. frequency as is evident from either Figure 1.15 or Figure 1.16 (even if the error bars are larger for Figure 1.16 because fewer map pixels were used in the average).

1.4.7 Polarization Angles

The Galactic magnetic field generally causes polarization angles to be perpendicular to the Galactic plane in the millimeter regime. However, BICEP and WMAP

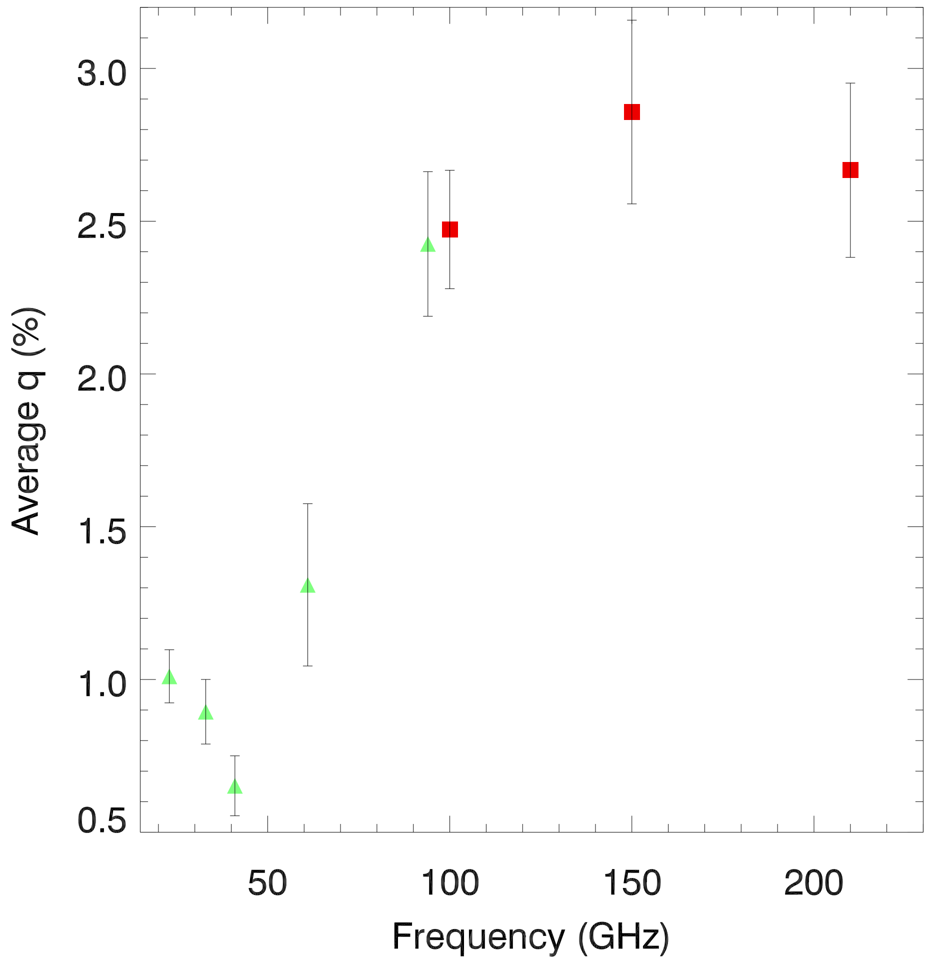

Figure 1.16: The average and error of q from the 220 GHz analysis region pixels combining all the data at each BICEP (red) and WMAP band. This shows a different method of computing q vs. frequency as compared to Figure 1.15, which uses a model to find the value of q, splits the data by boresight angle or DA, and uses a different number of pixels at 220 GHz. Once again a general trend of increasing polarization fraction vs. frequency is found with the minimum q occurring near 40 GHz. There is a steep increase in polarization fraction between 60 GHz and 100 GHz with the minimum fraction occurring near 40 GHz.

measurements show the magnetic field is not exactly parallel to the plane and changes direction between the two observing regions (Figure 1.17). The analysis area is split in half by region, Gal-bright (27 pixels) and Gal-weak (26 pixels), and the weighted average polarization angle for each BICEP boresight maps and WMAP DA is found. The two BICEP boresight maps per band show the general level of systematic uncertainty due to excess noise and telescope systematics. WMAP points are from each DA separately, which can be indicative of possible systematic uncertainty in a given band.

The average polarization angle in the Gal-bright region from both BICEP and WMAP is $6.2^\circ \pm 1.7^\circ$ whereas the average polarization angle in the Gal-weak region is $20.8^\circ \pm 2.2^\circ$ for both BICEP and WMAP. This represents a 5 sigma detection of a difference in polarization angle between the two regions. Note that the BICEP angles have not been corrected for filtering effects.

BICEP and WMAP polarization angles can also be compared to starlight polarization data. Millimeter-wave dust polarization is due to emission from particles that are preferentially aligned perpendicular to the local magnetic field (Lazarian, 2007). A complimentary process takes place in the optical band due to absorption, leading to polarization angle that should be rotated 90° relative to the millimeter-wave polarization. Heiles (2000) compiles a table of stellar polarization measurements and characteristics that can be used to compare polarimetry from the optical and millimeter-wave bands. Out of the 9286 stars, only those with angle errors less than 10° that are within the BICEP observing region were considered. For direct comparison, the starlight polarization angles have the expected 90° difference subtracted off. There were 36 stars with starlight polarization measurements in the Gal-bright region giving a weighted average polarization angle of $-8.3^\circ \pm 3.8^\circ$ while there were 24 stars in the Gal-weak region giving a weighted average polarization angle of $28.1^\circ \pm 2.8^\circ$. One caveat is that the starlight polarization measurements do not exactly track BICEP's and WMAP's measurements in space, as there are multiple stars in some map pixels and none in others. In general, there better agreement between optical and millimeter-wave polarization angles in the Gal-weak region as opposed to the Gal-bright region.

The polarization direction seen in all millimeter-wave bands and by the starlight polarization measurements increases systematically from the Gal-bright to Cal-weak regions. Since the Gal-bright and Gal-weak regions are separated by 60° in Galactic longitude, this indicates the Galactic magnetic field has structure on very large scales. Further small-scale analysis is possible, but results are inconclusive due to the uncertainty in BICEP's current polarization angle measurements. As opposed to q, there is no difference in the average polarization angle between pixels whose intensity is less than the median intensity and greater than the median intensity. No trend in polarization angle as a function of frequency is detected, showing consistent, independent polarization angle measurements from different lower frequencies where synchrotron dominates to high frequency where dust emission dominates.

1.4.8 Visual Optical Depth

In order to compare underlying astronomical objects from the optical to millimeter-wave band, the intensity of the emission can be converted to a common unit used in studies of the interstellar medium, visual optical depth, A_V. Following Equation 1.18 the conversion can be calculated as:

$$\frac{dA_V}{dT} = \frac{dA_V}{d\tau} \times \frac{d\tau}{dI} \times \frac{dB}{dT}\Big|_{2.725\ \mathrm{K}}$$

where the relationship between the emitted intensity and optical depth, assuming an optically thin medium, is given by:

$$I = B(1 - \exp^{-\tau}) \approx B\tau.$$

A relationship to millimeter-wave optical depth, $\tau(\lambda)$, derived by Hildebrand (1983) and Dickman (1978) is:

$$A_V \approx 1900\,\tau(\lambda)\left(\frac{\lambda}{250\ \mu\mathrm{m}}\right)^2$$

Assuming a dust temperature of 20 K, the conversion factor is calculated as:

$$\frac{dA_V}{dT} \approx 1900\left(\frac{\lambda}{250\ \mu\mathrm{m}}\right)^2 \times \frac{1}{B_{(20\ \mathrm{K})}} \times \frac{2k_B\nu^2}{c^2}\frac{z^2e^z}{(e^z-1)^2}.$$

Substituting in the values of the constants, wavelengths, and BICEP band centers this gives conversion factors of:

$$\frac{dA_V}{dT} \approx 14.0, 4.32, 1.48\ \frac{\mathrm{A_V}}{\mathrm{mK}}, \tag{1.20}$$

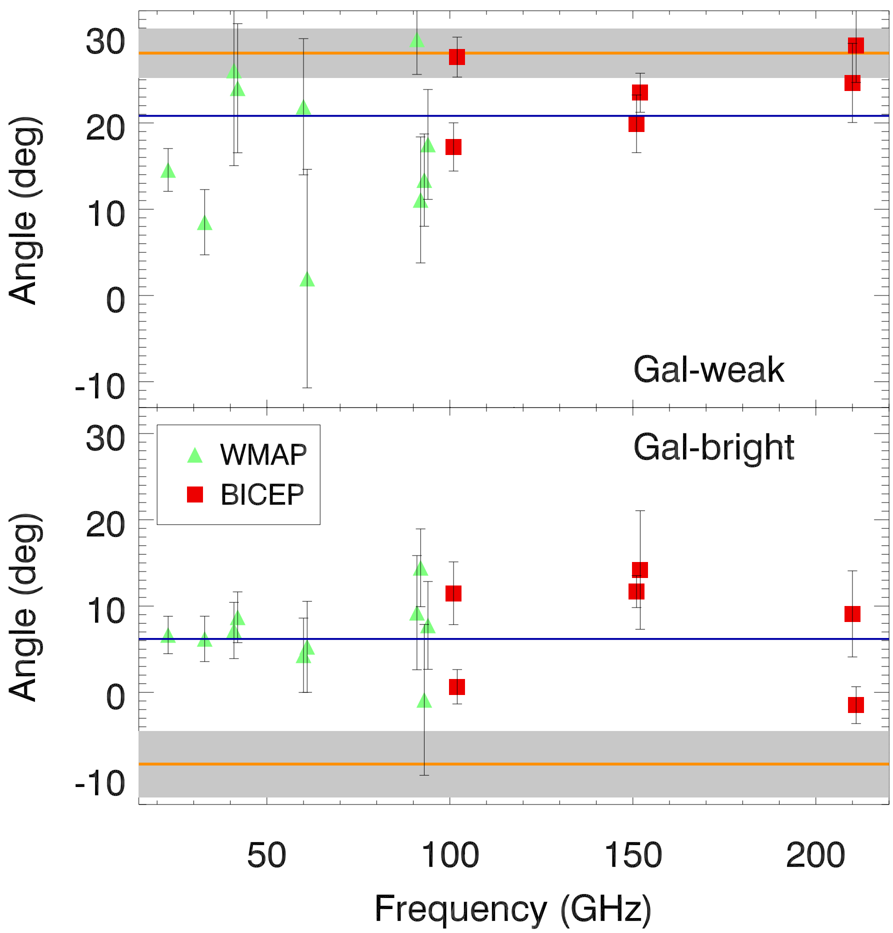

Figure 1.17: Polarization angle as a function of frequency for BICEP (red squares) and WMAP(green triangles) with the average angle over-plotted (blue line) and the average starlight polarization angle (orange line) and uncertainty (gray shaded region) for the Gal-weak region and Gal-bright regions. The polarization angles do not have any trend as a function of frequency in either region showing consistency between the two experiments and different emission mechanisms. There is a net positive rotation of polarization angle from the Gal-bright to Gal-weak regions for all millimeter-wave bands as well as the starlight polarization angles indicating large scale structure in the Galactic magnetic field.

for 100, 150, and 220 GHz respectively. One caveat to this calculation is that the factors are only valid for dust emission. Section 1.4.5 showed that at 95 GHz, 51% of the emission comes from other sources such as synchrotron radiation. Using the factors of [0.51, 0.87, 0.97] from Section 1.4.5, intensity maps from BICEP can be converted to A_V for the dust component in the map as:

$$\frac{dA_V}{dT_{BICEP\ Dust}} \approx 7.14, 3.75, 1.44\ \frac{\mathrm{A_V}}{\mathrm{mK}}, \tag{1.21}$$

for 100, 150 and 220 GHz.

BICEP detections span a thermodynamic temperature brightness range from [0.1, 0.3, 0.7] to [6, 8, 25] *mK* for 100, 150, and 220 GHz respectively. This corresponds to integrated visual optical depths A_V, using Equation 1.21, from [0.7, 1.1, 1.0] to [42, 30, 36]. On average, BICEP probes a component of the ISM which is more diffuse than star-forming regions ($A_V \gtrsim 10$), but is more dense than the medium sampled by optical polarimetry ($A_V \lesssim 2$). Due to the relative beam sizes and dust spectrum, BICEP measurements probe approximately the same density medium at local intensity maxima at all three bands. In principle, experiments such as QUaD and Archeops have the potential to probe even denser cloud complexes because of their smaller beam sizes; however, Archeops had higher noise levels than BICEP and both Archeops and QUaD have so far presented their polarization data with angular resolution $\approx 0.5°$, similar to BICEP.

1.5 Discussion

Continuum polarimetry results can be interpreted with the aid of a model in which the magnetic field for a given patch of sky is nearly constant in magnitude but has an angular structure which is a superposition of a uniform and a random component (Jones, 1989; Miville-Deschênes et al., 2007). The very simplest models, such as a completely uniform magnetic field or a completely random one, are ruled out by BICEP and WMAP which show a statistically significant trend of decreasing Q polarization fraction vs. increasing intensity (Section 1.4.6).

The detection of dust polarization with WMAP, QUaD, Archeops and BICEP constrains the degree of order in the Galactic magnetic field on large scales. An ordered magnetic field nearly parallel to the plane is detected at all millimeter-wave frequencies. The mean polarization angles are nearly constant as a function of frequency, but systematically change direction between BICEP's two Galactic regions. This change in direction is also found in starlight polarization measurements. This change shows structure in the Galactic magnetic field on scales greater than 60° in Galactic longitude.

The average degree of polarization observed in the integrated emission from star-forming cores ($A_V \gtrsim 30$) $p \lesssim 1.5\%$ Stephens et al. (2010), is similar to the degree of polarization observed with BICEP (Section 1.4.6). However, this coincidence does not imply that the observed BICEP polarization arises from a superposition of unresolved star-forming cores, with no significant polarized component emitted by the diffuse medium. While there is some evidence for coherence in the magnetic field across star-forming molecular cloud complexes up to 100 pc in size (Li et al., 2009), as a whole, those complexes and cores have a nearly random distribution of magnetic field directions and there is no evidence for coherence in the dense medium on larger scales (Glenn et al., 1999; Stephens et al., 2010). The contribution from these star-forming complexes to BICEP maps would consist of polarization with a high angular disorder, averaging to very low polarization when the beam encompasses multiple complexes. For example, a BICEP 150 GHz 0.6° beam corresponds to 50 pc for a typical Galactic source at a distance of 5 kpc in the Gal-bright field, and hence poorly resolves molecular cloud complexes. Consequently, because BICEP observes a substantial degree of polarization over the whole Galactic plane at $\sim$1° resolution on average, BICEP must sample a medium outside star-forming cores, one with an embedded magnetic field that retains a significant component ordered on the Galactic scale.

On the other hand, BICEP rules out a model where no additional polarization intensity comes from the higher density ISM. The polarization fraction drops somewhat as surface brightness increases, $q \propto I^{-0.47}$, but the decline is more shallow than $q \propto I^{-1}$ as predicted by the toy model of Section 1.4.2 having bright unpolarized sources embedded in a polarized medium. Therefore, BICEP measurements probe aligned grains and magnetic fields over the full range of observed column densities approaching star-forming cores. Jones (1989) and Fosalba et al. (2002) find an equivalent power law exponent from starlight data closer to $\eta_{em} = -0.25$, implying a more ordered magnetic field than what is implied from millimeter-wave measurements. A caveat to this comparison is those previous works analyzed total polarization fraction *p*, which does not necessarily have the same functional relationship as *q*. No attempt to directly model *q* using magnetic fields is included in this paper.

The detection of statistically significant polarization across the Galactic plane at all intensity levels shows that there are aligned dust grains across the entire map. The η parameter indicates the nature of the Galactic magnetic field and the disorder within the beam and along the line of sight. The polarization fraction *q* increases as a function of frequency, which was somewhat unexpected; other work has indicated that the opposite can be true at higher latitudes due to the much larger polarization fraction intrinsic to the synchrotron emission compared to dust polarization (Kogut et al., 2007). In contrast, BICEP has shown that dust emission can have a higher polarization fraction in the Galactic plane. This could indicate unpolarized emission mechanisms such as spinning dust play a more important role in the map regions analyzed here or it could be an indication that material emitting synchrotron radiation exists in more randomized Galactic magnetic field regions on average, as opposed to dust grains which may lie in more ordered field regions.

The observations discussed here are consistent with a Galactic magnetic field whose structure and order vary inversely with density. The increasing disorder in denser components of the ISM may be due to gravitational or dynamical accumulation of gas and/or feedback from star formation. The high angular resolution and sensitivity of the Planck (Tauber et al., 2010) 350 GHz polarization channels should be able to map this structure with greater precision to discriminate among more detailed models for the neutral ISM.

1.6 Conclusion

BICEP's Galactic observations have added new information and insight into Galactic physics, while also confirming previous measurements. BICEP samples an intermediate optical depth of the ISM and polarization is detected everywhere within a two degrees of the Galactic plane with values ranging up to a few percent at 100, 150, and 220 GHz. BICEP detects a significant trend of decreasing polarization fraction as intensity increases in the maps and increasing polarization fraction as a function of frequency. Polarization angles were found to be consistent from 23 GHz to 220 GHz and in general agreement with polarization angles measured by stars in out observing regions. Adding 220 GHz capability to BICEP helped to refine the understanding of in-plane foreground emission. BICEP data have shown astronomical foregrounds to be complex, and simply modeling polarization as a percentage of unpolarized intensity is insufficient. While polarized foreground models in the Galactic plane are becoming more precise, less is known at higher latitudes and it is not obvious that one can extrapolate models from the plane to these latitudes. Future CMB polarimeters are poised to build upon BICEP's results.

1.7 Acknowledgments

We would like to especially recognize Andrew Lange whose passing has deeply affected everyone on the team and who never saw the culmination of this project. Without his guidance and friendship this paper would not have been possible.

BICEP is supported by NSF Grant OPP-0230438, Caltech Discovery Fund, Caltech President's Fund PF-471, JPL Research and Technology Fund, and the late J. Robinson. We thank our colleagues in the ACBAR, Boomerang, QUaD, Bolocam, POLARBEAR, and SPT collaborations for advice and helpful discussions, Kathy Deniston for logistical and administrative support, and the South Pole Station staff for their support. We gratefully acknowledge support by the NASA Graduate Fellowship program (E.M.B. and H.C.C.), the John B. and Nelly Kilroy Foundation (J.M.K.), the NSF PECASE Award AST- 0548262 (B.G.K.), the U.S. DOE contract to SLAC No. DE-AC02-76SF00515 (C.L.K. and J.E.T.), KICP (C.P. and C.S.), and the NASA Science Mission Directorate via the US Planck Project (G.R.).

1.8 Appendix

1.8.1 BICEP 220 GHz channels

Prior to the second observing season, two feeds designed to observe through the 220 GHz atmospheric transmission window were installed into BICEP. These feeds represent the first attempt to observe CMB and Galactic polarization in this frequency band using PSBs. Due to the relative sensitivity of a 220 GHz channel to thermal dust emission and its polarization over lower frequency channels, the 220 GHz feeds serve a three-fold purpose. First, to constrain the polarization and intensity of the three main millimeter-wave sources (synchrotron, thermal dust, and the CMB) solely from BICEP observations, without an ad hoc foreground model, requires three frequency bands. Second, thermal dust emission and its polarization increase understanding of the physics of the Galaxy. Finally, it was unclear whether the CMB B-modes, BICEP's primary science target, would be contaminated by foreground emission, and would need to be modeled and removed. The 220 GHz feeds can carry more weight, per feed, than the other two bands for measurement of dust polarization due to the steep spectral index of millimeter-wave dust emission. More 220 GHz feeds were planned to be added in 2008 but logistical constraints at the South Pole in 2008 ultimately prevented this, limiting the experiment to using two feeds for the two final observing seasons.

Emission from the Galaxy has the potential to contaminate the faint B-mode signal in all observing fields. Since dust emission follows a thermal spectrum, by monitoring polarized interstellar dust at higher frequency than the primary B-mode bands (100 and 150 GHz), it is possible to monitor dust contamination with higher signal-to-noise per feed. While BICEP's CMB region, located at high Galactic latitude, certainly exhibits minimal dust column-density and therefore low-intensity millimeter-wave emission, this doesn't imply it will exhibit low-polarized emission due to the details of magnetic grain alignment (Lazarian, 2007). Little is known about the polarization properties of thermal dust emission in the high-frequency bands above 100 GHz used for CMB observations. BICEP's 220 GHz feeds are a unique link between the low-frequency CMB polarimetry of WMAP and the high-frequency survey of the Archeops experiment; from centimeter wavelengths to the sub-millimeter. The combination of WMAP, QUaD, BI-

CEP, and Archeops polarization observations of the Galactic plane cover more than a decade of frequency.

BICEP PSBs were only fabricated for 100 and 150 GHz operation. The 220 GHz pixels therefore were modified from 150 GHz PSBs used in the first season observations. The 220 GHz feed installation consisted of replacing two 150 GHz feedhorn stacks with a set of 220 GHz feedhorn stacks. Each feedhorn stack consists of three separate feedhorn pieces, all of which used the same outer-forms as the 150 GHz feedhorns. Two of the feedhorn inner-forms were made with a similar profile to the 150 GHz feedhorns. The most difficult part of the design process was to optimize the feedhorn that couples the radiation to the bolometer. In this case, the 220 GHz coupling feedhorn and corrugation profile had to be matched to the existing 150 GHz bolometer and housing. Using HFSS[3], the feedhorn-to-bolometer housing coupling, co-polar beam shape, total throughput, and cross-polarization beam response were optimized. Specifically, a straight 220 GHz feedhorn profile inserted into the 150 GHz housing resulted in the best overall simulated performance (Figure 1.18). The lower frequency cutoff of the 220 GHz band is defined by the feedhorn waveguide cutoff while the higher cutoff is defined by a set of metal mesh filters, borrowed from the ACBAR experiment (Runyan et al., 2003).

1.8.2 Telescope Characterization

Summarized here are the characterizations of parameters in Table 1.1 not mentioned previously. For more information, see Takahashi et al. (2010). The detector polarization angle, ψ, is measured with a 0.7° uncertainty across all three bands, while the relative angle uncertainty in the pair is measured with a 0.1° accuracy (Takahashi et al., 2010). Nominally this is the mechanical orientation of the bolometer web in the focal plane, however in practice, this is a parameter characterized after deployment for more precise analysis. The ability to measure this parameter with such low statistical and systematic error is one of BICEP's design advantages.

The average cross-polarization response, ϵ, measures the relative magnitude of the residual signal in the orthogonal or cross polarization direction given a purely po-

[3] Ansoft's HFSS: http://www.ansoft.com/products/hf/hfss/

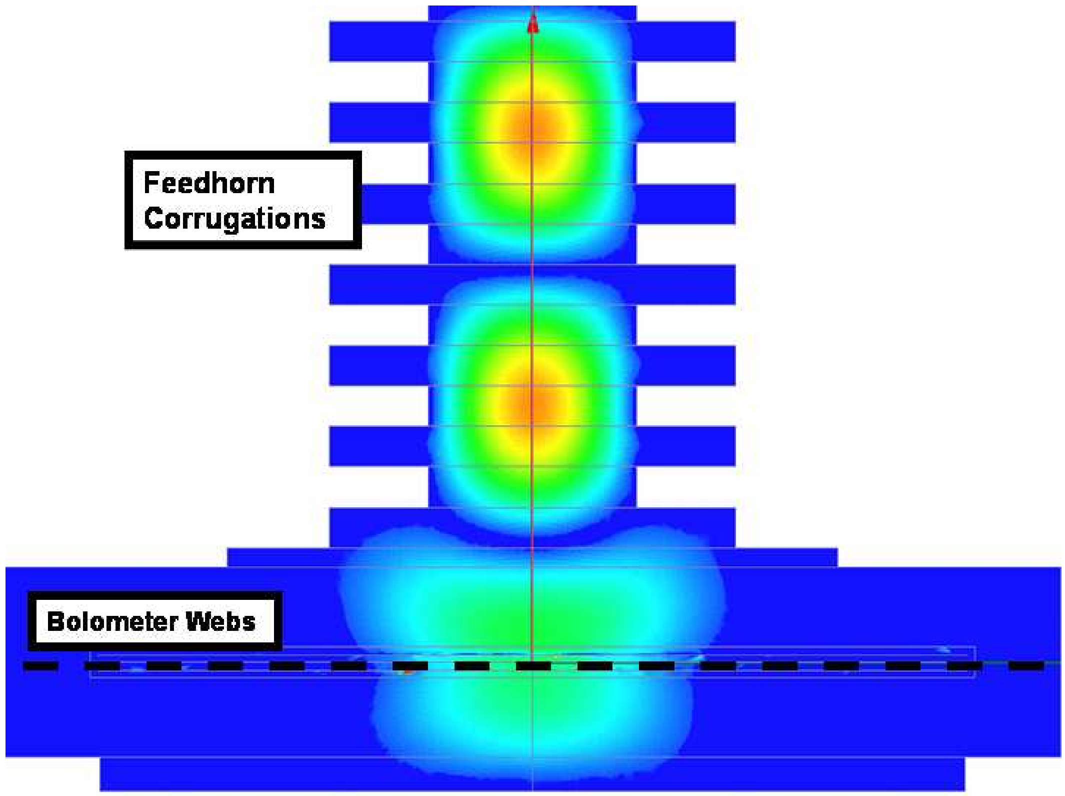

Figure 1.18: HFSS simulation of the 220 GHz coupling feedhorn to 150 GHz bolometer. The color scale represents the electric field intensity. The phase was chosen to maximize the field intensity at the bolometer webs. The shape of the coupling feedhorn and distance between the last corrugation in the feedhorn to the position of the bolometer webs is optimized to increase the coupling efficiency and minimize the cross-polarization response.

larized input in the co-polar direction. The HFSS simulations predicted the 220 GHz feeds should have an ϵ less than 0.07, similar to the measured value. Depolarization is larger for the 220 GHz channel due to the coupling effects between the 220 GHz coupling feedhorn and the bolometer and housing optimized for 150 GHz observations. The resulting polarization efficiency, γ, is the loss of polarization signal compared to the unpolarized signal used for calibration. γ directly affects the observed polarization fraction, however, it has been measured to 2% uncertainty, which is much smaller than other errors in the measurement.

The optical efficiencies (OEs) were derived by taking load curves while observing blackbody radiation at different temperatures and give the total end-to-end sensitivity on the sky. While this parameter is not used in the mapmaking pipeline, it is implicitly included in the telescope noise estimates. The OEs for the last observing season were 20.8%, 19.8%, and 15.8% for 100, 150, and 220 GHz respectively. HFSS simulations for the 220 GHz feeds predicted a coupling efficiency over 98% (similar to the 100 and 150 GHz feeds) with 2% reflected power. The OE of the feeds that were converted from 150 GHz to 220 GHz declined by an average of 15%, while the other feeds did not change between seasons. The simulated transmission and reflectivity did not include the lenses, which were optimized for 125 GHz operation (midway between 100 and 150 GHz), not 220 GHz.

The beam functions, $P(\Omega)$, were measured using a circularly polarized broadband noise source for 100 and 150 GHz feeds and Jupiter for 220 GHz feeds. The beam response functions are fit with an elliptical Gaussian giving an average beam full width half max (FWHM) of 0.93°, 0.60°, and 0.42° for 100, 150, and 220 GHz respectively. The differential beam size and ellipticities are very small for BICEP and do not affect the results of this paper. Both polarized and unpolarized sidelobe response are characterized by observations of a broadband source and are determined to be negligible for this analysis.

The absolute telescope pointing is calculated from observations of multiple stars taken by an optical camera mounted to the telescope. The absolute pointing is the same as used in Chiang et al. (2010) and is independent of a given feeds transmission band. Relative radio pointing for each feed is calibrated using individual maps of CMB temperature anisotropy. The differential pointing mismatch between PSB pairs has similar values across all three bands, with a mean of 0.0041°, 0.0046°, and 0.0047° (1.0%, 1.8%, 2.6% of the beam size) for 100, 150, and 220 GHz respectively. The 220 GHz intensity maps show some small evidence for differential pointing between the two PSBs within a feed and between the two feeds.

Reflections in the optical system created a “ghost image” opposite to the primary image with respect to the boresight for each feed. The average ghost image power, as determined by observations of the Moon, was 0.41%, 0.50%, and 1.3% for 100, 150, and 220 GHz respectively relative to the primary image. The magnitudes of the ghost beam images relative to the primary image are nearly identical for a given pair of PSBs in a feed, giving power differences of 0.02%, 0.04%, 0.04% for 100, 150, and 220 GHz bands respectively. Since the Moon’s high intensity lowers the responsivity of the detectors, the ghost image systematics given here are upper limits. These differences are below the noise level in the Galactic polarization maps for all three bands. While this effect has been measured well using a bright source such as the Moon, there is no evidence for ghost effects in the Galactic maps.

A miscalibration of the time-domain impulse response, $K(t)$, would act like a beam size mismatch leaking intensity to polarization. However, the time-domain response for each of the three bands is measured to a very high precision and deconvolved from the raw 50-Hz-sampled timestream. There is no evidence for time constant mismatch from either the Galaxy data or CMB data.

Chapter 2

Galaxy Paper Addendum

Bierman et al. (2011), hereafter "B11", represents the finished product of BICEP Galactic analysis. A significant amount time and resources went into this publication; however, it only represents part of my effort towards this subject. In this chapter, I expand upon that work to include results not included in the journal submission.

2.0.3 Spectral Mismatch vs. Relative Gain

Section 1.3.3 of B11 discussed spectral gain mismatch based on FTS measurements; however, it is important to also derive these calibration parameters from other, complementary methods. Spectral gain mismatch not only leaks intensity into the final polarization maps but that leakage is coupled with scan strategy and can be washed out due to averaging. Spectral gain mismatch primarily leaks intensity into the difference signal, or difference maps.

An ideal source to investigate intensity to polarization leakage is a bright unpolarized astronomical source with a spectrum similar to that of the Galaxy. The Galaxy itself is not a good source because it is polarized and that polarization is the goal of the observations. The next best source would be the CMB dipole, which is similar in brightness to the Galaxy at 100 and 150 GHz but much dimmer at 220 GHz. However, the noise level and observation time needed for this type of observation makes the use of the CMB dipole unrealistic (although these observations were made).

The other possible source is the CMB anisotropy, which is polarized, mostly due to the symmetric polarization field correlations ($\langle EE \rangle$). However, the temperature-polarization correlation ($\langle TE \rangle$) is zero when averaged over ℓ. Therefore the correlations of the intensity and either Stokes Q or U maps should be zero. In addition, the correlations between the raw pair-sum and pair-difference maps, that give rise to Stokes Q and U, should also be zero. The major problem with this method is the CMB anisotropies are an order of magnitude smaller than the CMB dipole necessitating a large amount of integration time. Adding to the signal-to-noise problem is that the leakage needs to be computed on a per-feed basis, so adding more detectors does nothing to help.

My collaborator Dr. Chiang derived the intensity to leakage gain factors correlating the sum and difference maps from each feed in BICEP for the first two years of BICEP observations. The cross spectral leakage gain factor is derived similar to the absolute gain calibration factor by:

$$g_{leak} = \frac{\langle a_{\ell m}^{dif} a_{\ell m}^{sum} \rangle}{\langle a_{\ell m}^{sum} a_{\ell m}^{sum} \rangle} \tag{2.1}$$

where $a_{\ell m}$ are the angular spherical harmonic transform components of the maps made from the pair-sum timestreams (“sum”) and pair-difference timestreams (“dif”), not from the Q and U polarization maps. Figure 2.1 shows a scatter plot of the two data sets. The 150 GHz data show a very good correlation between the two data sets giving confidence that this effect is real. The slope of the scatter plot at 150 GHz is -0.67 where the minus sign is dependent on how the differences are defined. There can also be a factor of two difference based on the definition of cross spectral leakage. Either way, there is still a difference of 40% in absolute magnitude between the two sets for an undiscovered reason. There is a single 150 GHz outlier point (RTC 52), which has spectral mismatch leakage that is highly dependent on the source model used. At 100 GHz there is no general correlation although two feeds (RTC 40 and RTC 36) potentially show some effect. The reason for the poor correlation at 100 GHz could be entirely due to the higher noise level at 100 GHz compared to 150 GHz. Overall, this comparison showed additional evidence of intensity to polarization leakage and that the values computed using FTS measurements were a viable diagnostic.

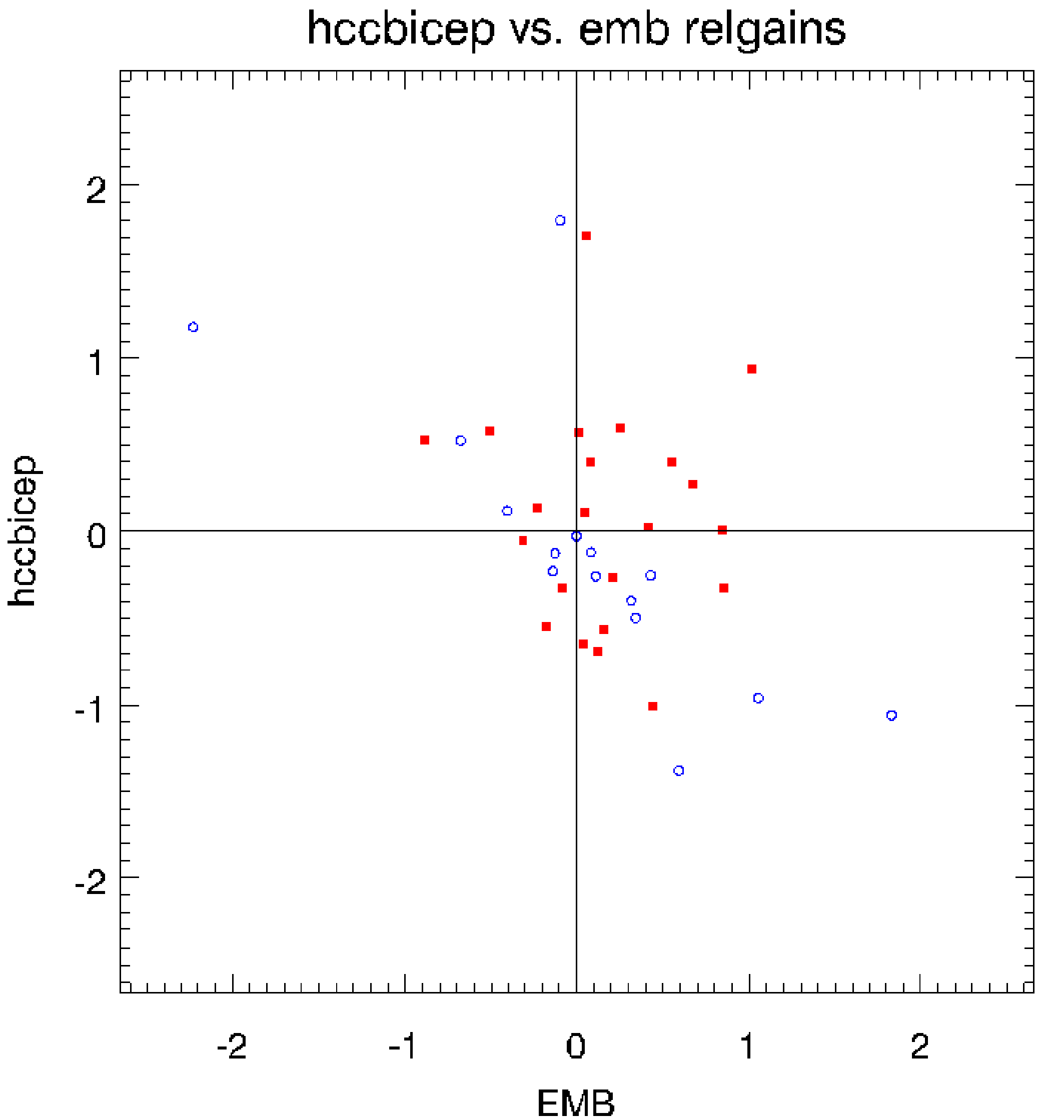

Figure 2.1: Spectral mismatch leakage (EMB) vs. cross spectra leakage (hccbicep) from BICEP's second observing season for the 100 GHz (red squares) and 150 GHz (blue circles) feeds. The cross spectra leakage is derived from CMB anisotropy measurements while the spectral mismatch leakage values are calculated using measured spectral responses and models of the atmosphere and CMB anisotropy spectral response. Both effects leak intensity into polarization, so these are two independent measurements of the same resulting effect. There is very good correlation between the values at 150 GHz, and less so at 100 GHz.

2.1 Az360 scans

One interesting scan strategy attempted using the BICEP telescope was to spin the telescope in a complete circle relative to the South Pole. The scan length in azimuth was 360° (called Az360 scans). Scanning in local coordinates like this makes a map projection in Galactic coordinates similar to a doughnut, with the Galactic South Pole in the center. These long scans allow lower frequency modes to be recovered and also provide a longer baseline to remove contamination in the Galaxy.

2.1.1 CMB Dipole

The most common way to refer to the magnitude of the CMB anisotropy is that it is 10^{-5} of the 2.725 K monopole signal. It is true that the cosmological anisotropies are this small; however, the CMB also has a relatively large dipole signal that is 3 mK peak-to-peak over the full sky caused by the relative motion of our Galaxy relative to the last scattering surface. Satellite and balloon experiments must take time to consider this mode and remove it carefully so that it does not contaminate measurements of other sources. For ground experiments, the noise coherence on this large scale usually prevents detecting this signal. Also necessary for detection of the dipole is a telescope that can observe a large fraction of the sky. BICEP's Az360 scans fulfill both of these requirements.

In order to detect the CMB dipole, the Az360 scans must minimally filter low frequency modes. For each Az360 half-scan, consisting of 1080 samples, the mean and variance are computed. Just the mean is removed as opposed to higher order polynomials or a scan-fixed signal. The inverse variance is still used as the weight to co-add the scans.

The CMB dipole can be discerned in the raw maps at both 100 and 150 GHz; however, there is not enough sensitivity at 220 GHz to see it. The dominant feature in these basic maps are large striping features. To remove this, the destriping method from Culverhouse et al. (2010) is employed. The general principle of this method is to make a final map using minimal filtering, then remove the striping by because this false signal power occurs at very high frequencies perpendicular to the scan direction in the final two-dimensional map. The final minimally filtered map is low-pass filtered, removing the striping and producing a filtered map that can be used as a basis to more effectively separate signal and noise in the raw timestreams. Timestreams are generated from the destriped map and subtracted from the raw timestreams, removing true signal and allowing a better estimate of the low frequency noise to be removed from the raw time streams. The improved noise modes estimates are removed and the timestreams are added together again to give a destriped final map. Theoretically there is some loss of signal in this method, but only at higher frequencies and only in one direction. Note that this method effectively removes striping features but does not remove scan-fixed signal. These are the main sources of uncertainty on large scales in the Galactic maps from Chapter 1 necessitating the polynomial removal with masking.

Figure 2.2 shows the BICEP Az360 maps from this processing and a plot of the CMB dipole found by the WMAP satellite. Even with the more advanced processing, the dipole is still not visible at 220 GHz. A visual review of the raw time streams shows a large scan fixed signal; however, this eventually averages down at both 100 and 150 GHz to see the CMB dipole. While these final maps look good from visual inspection, a review of the boresight jackknife maps still show some residual power consistent with scan-fixed contamination. Regardless, the images at 100 and 150 GHz are still both dominated by the CMB dipole signal. One could potentially use these maps as a calibration tool for the experiment as opposed to the CMB anisotropies. The problem is that the 1/f noise is higher where the CMB dipole is observed in the audio band relative to the almost white noise level where the anisotropies are observed. It would require a large amount of data to average down far enough to get good signal-to-noise on the dipole, which is the opposite scan strategy needed when trying to observe cosmological B-modes. If an experiment were trying to observe the cosmological reionization B-mode peak at an ℓ~10, observing the CMB dipole would be a natural strategy.

2.1.2 Filtered Az360 Scan Maps

Another possible method to filter the Az360 scans is to apply the nominal Galactic processing strategy (Section 1.3.4). Figure 2.3 shows these scans at all three bands using the nominal Galactic filtering strategy using a four degree Galactic latitude mask,

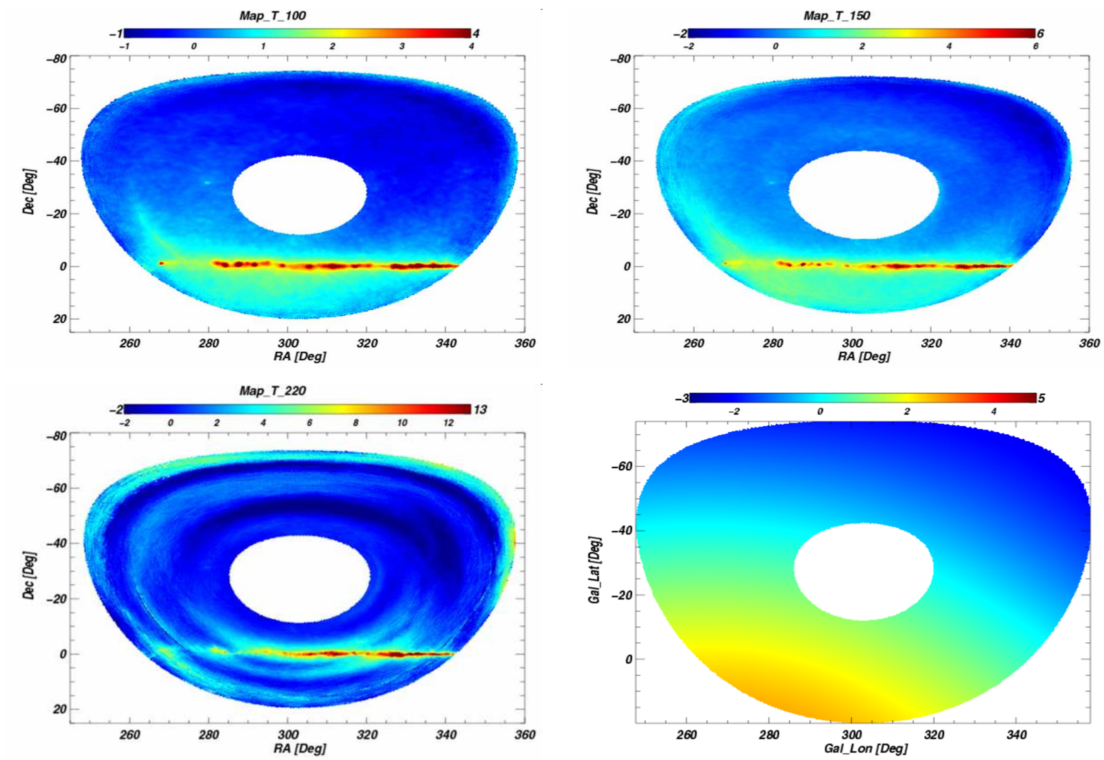

Figure 2.2: BICEP intensity maps from all three seasons co-added over all four boresight angles from 360° scans. The maps have a DC component removed and then are destriped with the technique from Culverhouse et al. (2010). The lower right panel is the CMB dipole, fit to by WMAP (Bennett et al., 2003), and plotted in the BICEP observing region. At both 100 and 150 GHz the dipole signal is visible while at 220 GHz the noise still dominates. The scan fixed signal has not been removed and does contribute some to these maps; however, the dipole signal is still the dominant feature.

except a fourth order is used instead of a second order polynomial. The contrast level is chosen to emphasize the CMB anisotropies. The lowest integration time occurs at the lowest elevation centers, which shows up at the edges of the Galactic “doughnut region”. The 220 GHz maps suffer from only having two pixels in the focal plane and higher noise, therefore resulting in a marginal detection of anisotropies for these scans at this map resolution. Both 100 and 150 GHz clearly show the anisotropies. The size of the Galactic signal can be seen to increase rapidly as a function of electromagnetic frequency in these plots.

Since these maps were not used for quantitative studies of the Galactic plane, it was useful to remake the maps in a way that completely minimized non-white noise at the cost of removing more signal. To accomplish this, a technique similar to Chiang et al. (2010) is used. A scan fixed template is made from each hour of data and subtracted from each scan. Instead of 100 scans from Chiang et al. (2010), this data set only had 22 scans per hour because the scan length was so much longer. In addition to the ground subtraction, a tenth order polynomial was removed. No masking is used to make the maps in Figures 2.4, 2.5, and 2.6 so there are some artifacts due to ringing apparent.

In making these maps I discovered that using the linear regression method with normal polynomials up to tenth order gave unstable results. The source of the instability is the matrix that is inverted to find the coefficients can have very large off-diagonal elements. To counteract this, I developed my own code to generate orthogonal polynomials up to a general order and scan length. Using these orthogonal functions as the column vectors that make up the fitting matrix, automatically sets the off-diagonal elements of the inverted matrix to zero, thereby stabilizing the matrix inversion. Using this procedure, polynomial fitting can be reliably accomplished up to a very large polynomial order. One limitation is that the orthogonal polynomial basis could not be made to a high enough precision to be a complete basis for a given scan length. For example, a normal scan has 200 points, therefore orthogonal polynomials up to 199th order (the DC component is the zeroth order) are necessary to form a complete basis. However, even using double precision, the polynomials at the highest order still could not be made orthogonal. For a 200 point basis, I was only able to make orthogonal polynomials up to approximately 125th order. For the Az360 scans of length 1080, polynomials above

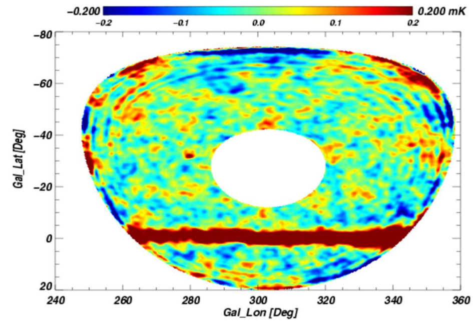

(a) 100 GHz

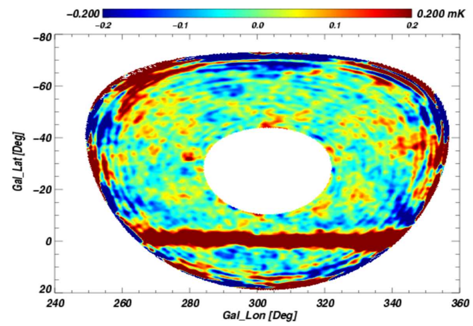

(b) 150 GHz

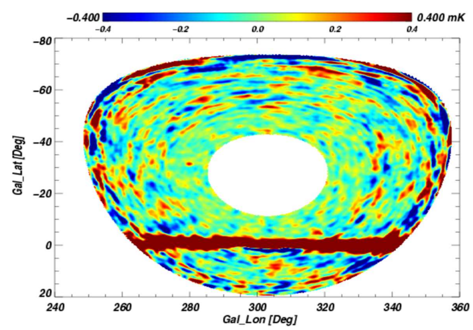

(c) 220 GHz

Figure 2.3: BICEP intensity maps from all three seasons co-added over all four boresight angles from Az360 scans for 100, 150, and 220 GHz from top to bottom respectively. The filtering method is similar to the nominal Galactic paper filtering scheme. The color stretch saturates the Galactic plane but allows the CMB anisotropies and some low level Galactic signal to be seen. The CMB anisotropies are clearly visible at 100 and 150 GHz while only marginally visible at 220 GHz due to fewer feeds and integration time at that band. The large Magellanic cloud can be seen at ℓ = 280° and b = −30° at all bands and seems to be nearly constant in brightness similar to the CMB anisotropies.

500th order are possible. Fortunately, this high a degree was not needed for the Az360 scans.

Figure 2.4 shows the Galactic plane signal in celestial coordinates, which can be seen clearly and with almost all white noise features. At this contrast level the higher level filtering causes visible effects in the map. Figure 2.5 and Figure 2.6 show the same maps in Galactic coordinates for Q and U polarization. These maps, in addition to being visually pleasing maps with large map coverage and low noise, are useful to check whether certain features in the less filtered maps may be real or are just artifacts. The increase or decrease in signal strength from one band to another is also visible.

2.2 Elevation Scans

Normally, the telescope scans are at a fixed elevation to minimize effects due to atmospheric loading changes, gravitational effects, and changing thermal properties of the telescope. In addition, any scan strategy in elevation must also deal with more complicated geometrical projection effects and shorter scan lengths. One instrumentation problem is the elevation drive is not designed to do elevation scans whereas the azimuthal drive system is exactly designed to give smooth and continuous motion over long lengths and long time intervals.

Given all these problems, elevation scans may not be a hopeless endeavor. With changes in atmospheric loading also comes a better unpolarized calibration source. Essentially, elevation scans are just very large el-nods, which are used as calibration tools. Scanning in elevation and staying fixed at a single azimuthal center lets the sky drift by, observing every map pixel by every focal plane feed. Since BICEP's feeds have polarization angle sensitivity that changes for every feed (by design), this means elevation scanning gives a nearly continuous polarization angle coverage for each map pixel. This increased coverage allows leads to optimum removal of beam and telescope systematics. To do this with azimuthal scans would take significantly more elevation centers.

While these are all advantages for elevation scans, the main motivation behind elevation scans is to get orthogonal information on the sky compared to azimuthal scans. Low frequency modes are inevitably filtered out and removed because they are contami-

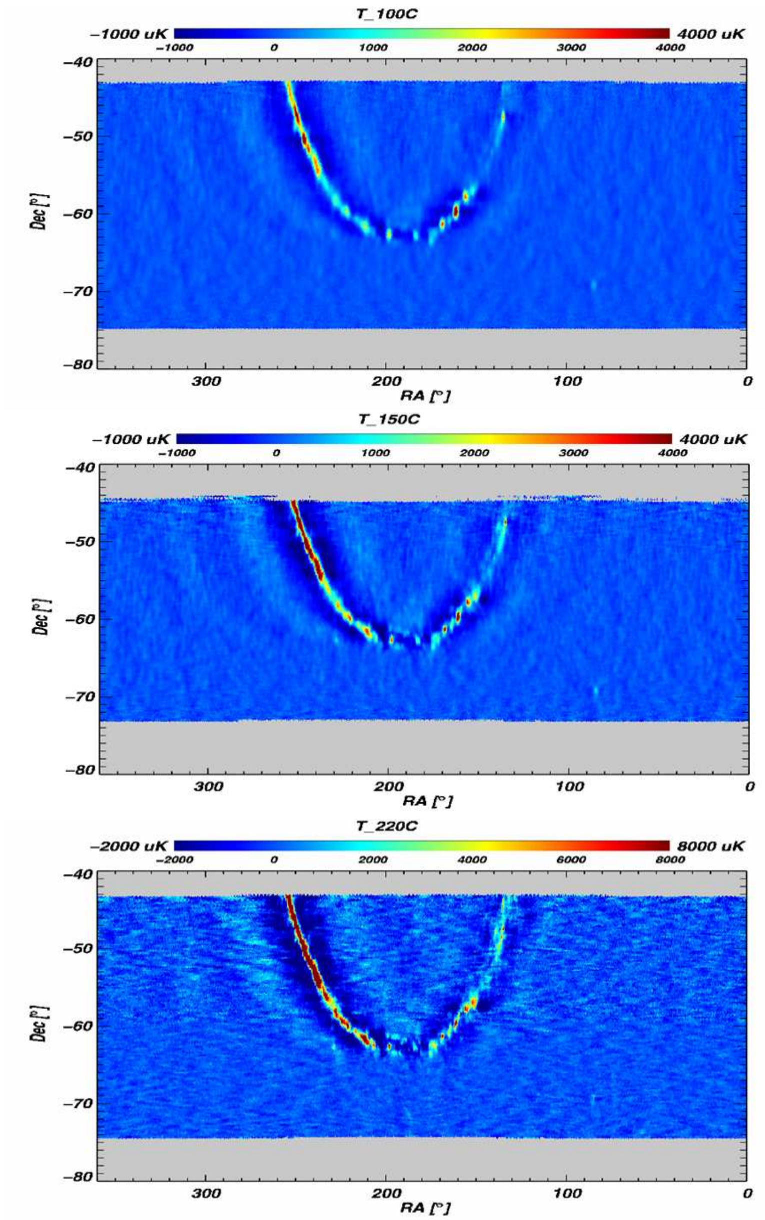

Figure 2.4: BICEP intensity polarization maps from all three seasons co-added over all four boresight angles from 360° scans shown in celestial coordinates for 100, 150, and 220 GHz from top to bottom respectively. A set of tenth order orthogonal polynomials has been removed along with a scan-fixed template. The 220 GHz maps still seem to have noticeable 1/f noise features due to less integration time, but the 100 and 150 GHz maps have very high signal-to-noise at this contrast level.

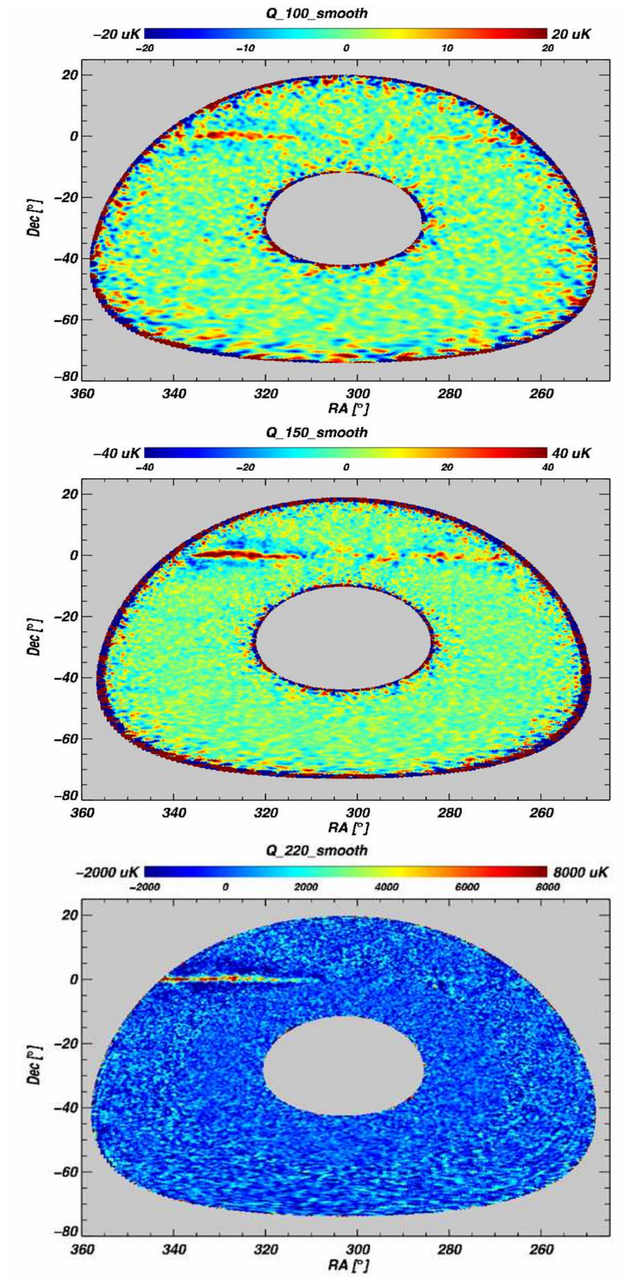

Figure 2.5: BICEP Q polarization maps from all three seasons co-added over all four boresight angles from 360° scans for 100, 150, and 220 GHz from top to bottom respectively. A set of tenth order orthogonal polynomials has been removed along with a scan-fixed template. Q power is mostly positive (perpendicular to the plane) in all three bands due to the Galactic Magnetic field direction. Some features that seem to exhibit $-Q$ power, such as in the Galactic plane at 150 GHz near $\ell = 295°$.

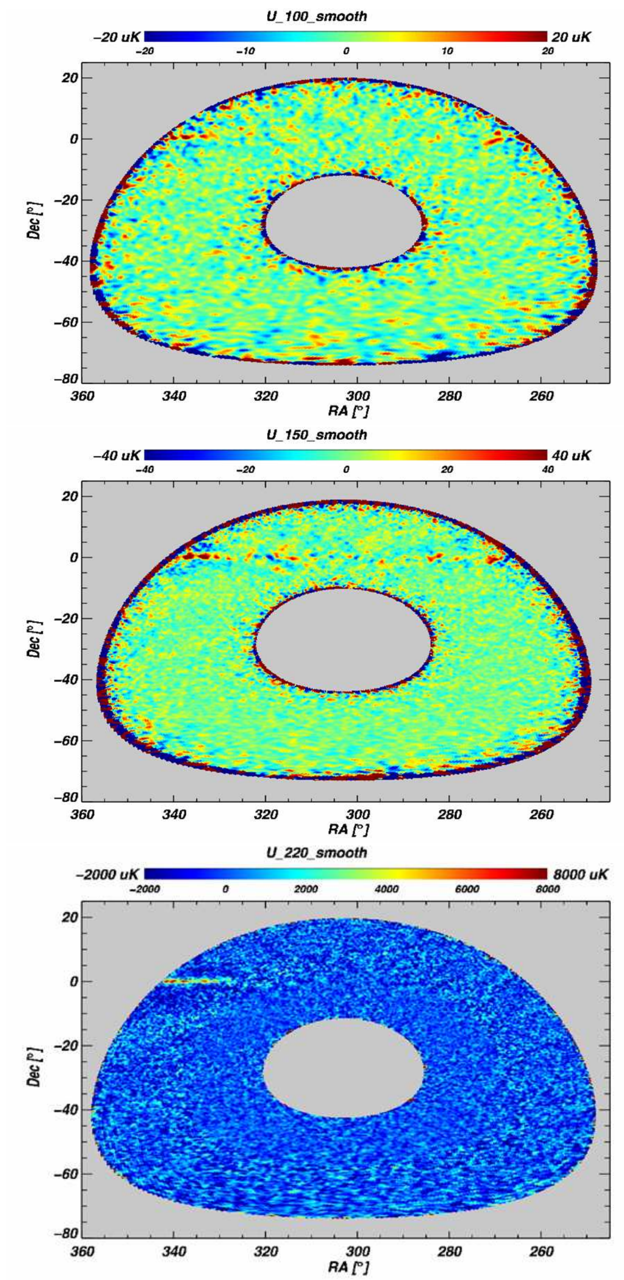

Figure 2.6: BICEP U polarization maps from all three seasons co-added over all four boresight angles from 360° scans for 100, 150, and 220 GHz from top to bottom respectively. A set of tenth order orthogonal polynomials has been removed along with a scan-fixed template. There is a non-zero U power at all three bands, mostly in the Gal-bright regions.

nated no matter what the scan direction happens to be. Therefore, by scanning in orthogonal directions, it is possible to recover the low frequency modes lost in one direction by using the maps made from the other direction. The term, "cross-linking", is most commonly used for this principle.

The easiest way to think of this is in the two-dimensional Fourier plane. Each set of maps from azimuthal and elevation scanning can be filtered in Fourier space by setting the low frequency modes in either the horizontal or vertical directions to zero. Then the two maps can be averaged together and the zeros replaced with information from the maps made in the other direction. The only frequency that can never be filled is the lowest central one at $k_x = k_y = 0$, because that one is filtered in both directions. While this principle seems very promising, the data analysis of the BICEP elevation scans never progressed far enough to show the possibilities of full implementation.

The scan strategy for elevation scans is similar to azimuthal scans, except the azimuthal and elevation drives are switched. The telescope stayed fixed at a single azimuthal value while doing 30° sky dips. As the sky rotates, the map area increases and polarization angle coverage per map pixel improves. The data analysis pipeline I wrote used similar methods from the azimuthal scans but with a few changes. I deconvolved the bolometer time constants, downsampled, and found all the half-scans similar to azimuthal scans. For elevation scans there is no need to do el-nods before and after the scans because a change in atmospheric loading occurs naturally. For each half-scan in the elevation direction, I fit the data to a cosecant-elevation model exactly like the operation performed on el-nods. I used these fit values, averaging over adjacent values, to produce a full atmospheric model for the entire scan period, which is removed from the data per channel. For the initial processing, the Galaxy is not masked and there is no evidence this adversely affected the fits. Using these now calibrated half-scans with the atmospheric effects removed, I subtracted a seventh-order orthogonal polynomial and a scan-fixed template from each scan without masking the Galaxy. All the scans are co-added from all the telescope boresight angles using the inverse variance of each half-scan as the weight.

Intensity and integration maps from the initial run are shown in Figure 2.7 and Figure 2.8. Looking at the integration time map gives some idea of the geometrical effects involved in these elevation scans and the resulting consequences. The Galactic signal is seen at all three bands, showing that at least the intensity data can be recovered with elevation scans. Figure 2.8 shows the Galactic Q signal found from these initial observations, which shows no visual evidence of any sky signal. The lack of a detection is probably not due to inherent problems in elevation scanning but rather the analysis pipeline. Each bolometer is calibrated per half-scan for the entire scan time, possibly calibrating out the polarization signal. As further evidence of this, there is a hint of polarization signal in the 220 GHz maps at the level of the spectral gain mismatch problem discussed in Chapter 1. Spectral mismatch would not be calibrated out from performing the elevation fitting because the bolometers are not matched spectrally and would still leak temperature into polarization. A potential future project would be to upgrade the pipeline and re-analyze the elevations scan data, hopefully showing their full efficacy.

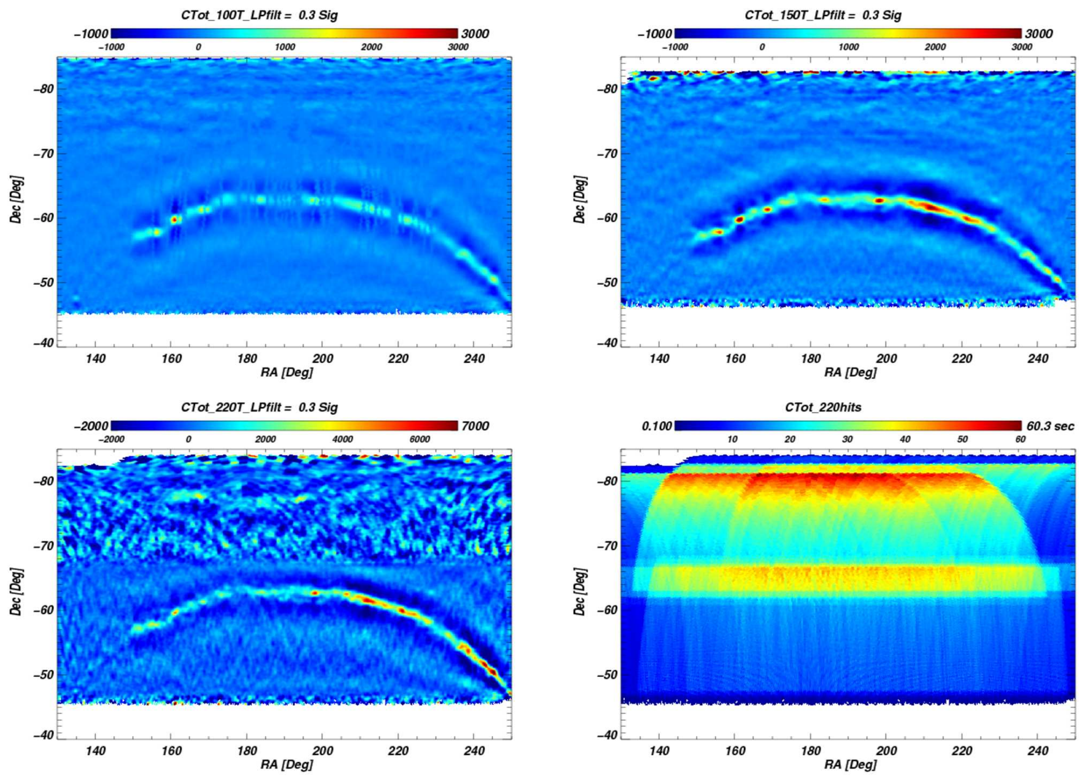

Figure 2.7: BICEP intensity maps from four elevation scan phases for 100, 150 and 220 GHz along with the 220 GHz hits map. A seventh order orthogonal polynomial has been removed along with a scan-fixed template from each scan. Intensity is seen in all three bands consistent showing that intensity data can be recovered by elevation scanning. The lower right hand plot is the integration time per 0.25° `Healpix` map pixel for 220 GHz demonstrating the projection effects involved in elevation scanning.

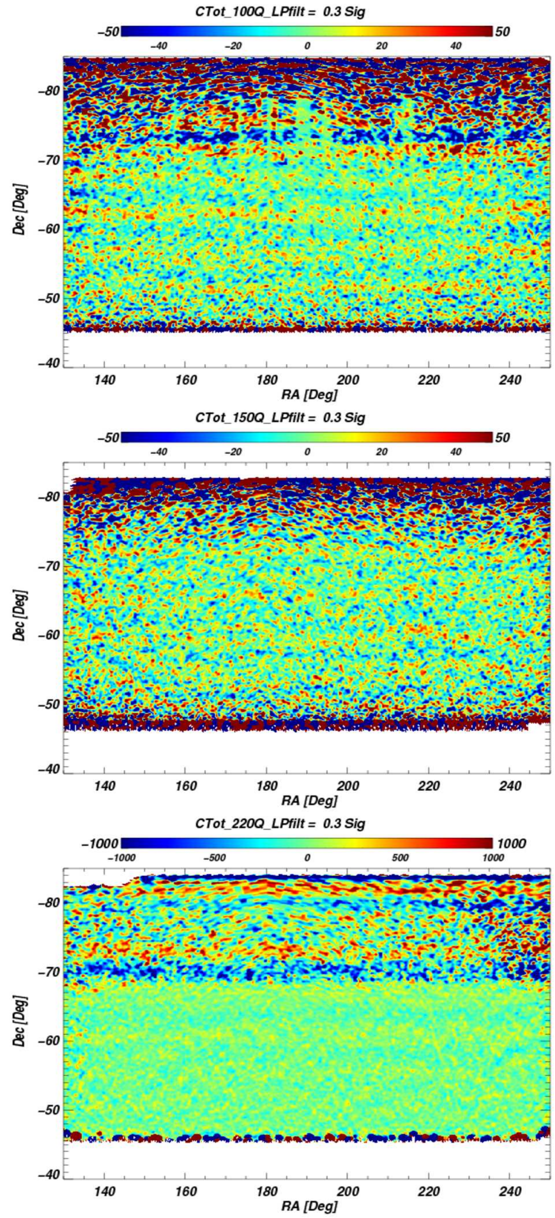

Figure 2.8: BICEP polarization maps from four elevation scan phases for 100, 150, and 220 GHz from top to bottom respectively. A set of seventh order orthogonal polynomials has been removed along with a scan-fixed template from each scan. There is no apparent Q polarization at 100 nor 150 GHz with only a hint of polarization at 220 GHz. The polarization at 220 GHz is believed to be due to spectral gain mismatch, which is discussed in Chapter 1. The lack of signal is most likely due to a sub-optimal data analysis pipeline process rather than a failure in concept.

Chapter 3

The UCSD FTS and BICEP Calibration

Extreme care is needed to fully characterize the properties of a millimeter-wave polarimeter. While this is not a glamorous task, the importance of this characterization was not lost on the BICEP team. A vast amount of personnel and resources were spent on agonizing over every aspect of the BICEP telescope. Most of my personal contributions to Chiang et al. (2010) come from participating and carrying out numerous characterization procedures. This is especially true of the spectral measurements that not only were used for Chiang et al. (2010) but also turned out to be crucial for the Galaxy publication and the 220 GHz channels. For this Chapter, I highlight my work on the UCSD FTS and the Far Field Flat runs used to characterize BICEP's beam properties.

3.1 UCSD FTS

In order to characterize the spectral response of all of BICEP's feeds and FRMs, a Fourier Transform Spectrometer (FTS) was built at UCSD. The basic idea of the spectrometer is an interferometric setup where varying the path length leads to characterization of different frequencies (Martin & Puplett, 1970). One factor making this construction easier is the precision of alignment and construction of parts is not as high at millimeter wavelengths. This wavelength size at this band also means the spectrometer is proportionally larger than at other bands as well.

3.1.1 FTS Design

The design requirements of the FTS are not fully defined by quantitative modeling and simulation but also needs personnel with previous experience using similar devices to set the size and functionality requirements. The general design process started with a review of the Case Western Reserve University device ("Ruhl FTS") built by Professor Ruhl and others (Matsuo et al., 1998; Bin et al., 1999), and modifying it for our needs. In the end, the entire layout was changed to optimize the ability, portability, and adaptability of the UCSD FTS. The moving arm was lengthened, the input and output ports rearranged for more portability, and the optical elements were standardized as much as possible.

While not a strict design requirement of the FTS, higher power and throughput are desired to expedite the characterization of dual-polarization feed telescopes such as BICEP. In these types of telescopes each feed has two orthogonally oriented polarization sensitive bolometers (PSBs). For sake of time and ease, they are characterized simultaneously by directing the polarized radiation from the FTS into each feed at 45° relative to PSBs such that each arm has one-half of the maximum optical power. Therefore, the trade-off to faster and simpler characterization is that higher throughput is needed.

The layout of the FTS is shown in Figure 3.1. A Martin-Puplett polarizing FTS is now a standard device in the millimeter-wave field. The source for the FTS is a broad-band thermal source ("FTS source"), usually highly emissive material (eccosorb) cooled to cryogenic temperatures with liquid nitrogen. The general design calls for the emission from the source to be polarized by a small free-standing wire grid ("polarizing grid") and collimated by the first mirror ("collimating mirror").

While I did try this configuration, it did not have the desired throughput; therefore construction of larger wire grids became the standard. I changed the design in Figure 3.1 by switching the order of the mirror and polarizing grid and attaching an external hot lamp source (GE sunlamp tanning bulb, T 2000°). The hot lamp provided a much brighter source for the system by almost an order of magnitude (~30 mV as opposed to ~5 mV). It also had the advantage of not needing cryogens and not being cold, which causes ice or condensation to form. The location of the collimating mirror was moved to the location of the old source and a new 12 inch polarizing grid was moved to the location of the old collimating mirror. The ability to construct large wire grids allowed the collimating mirror to come first in the optical design, making for a more compact system.

The next element of the UCSD FTS is the second free-standing wire grid (“splitting grid”), also 12 inches in size, which splits the polarized source into two components. This is the second splitting of the emission from the unpolarized source, so one fourth of the initial power is sent in orthogonal path directions. In both directions there is an optical element (“roof mirror”) that reflects the light and rotates the polarization direction sending the light back towards the splitting grid. Since the light’s polarization orientation is now rotated, light that was initially reflected down one arm now passes straight through to the output, and light that passed straight through to the other arm is now reflected towards the output as well. One of the roof mirrors is fixed and the other is placed on top of a moving stage. The fixed roof mirror is placed at the approximate center of the moving track, “the white light” fringe position. This is where the path length is equal in each direction, giving maximum constructive interference of the light from the two arms.

The last required optical element is the third free-standing wire grid (“combining grid”) which splits the output light into two polarization directions going to two separate ports. By splitting the outgoing light, the two polarization directions are summed (“sum port”) and differenced (“difference port”). Operationally, both output ports can be used as the main FTS signal. For some configurations, one port is used as a reference while the other is used to characterize a specimen. The UCSD FTS is nominally set to use only the differencing port, although this can be changed if need be.

The final element of the UCSD FTS is not required for the FTS to work properly, but is used to properly couple the light to the external system being tested. The large diameter collimated polarized beam propagating from the combining grid can either be directed or focused out of the FTS. If the simple collimated beam is required, a flat reflecting mirror is placed at the exit port to direct the light out of the FTS box. If a focused beam is required, a second mirror (“focusing mirror”) is placed at the output port. The initial UCSD test cryostat needed a focused beam and so two identical mirrors were made that could be used interchangeably as either the collimating or focusing mirror.

One modification I wanted to implement (but did not have the time and resources to do so) was to add two roof mirrors on either side of the polarizing grid. The polarizing grids splits the unpolarized broad band source into its two polarization directions, using one for the system and throwing away the other polarization. By replacing the eccosorb covered walls on either side of the polarizing grid with two roof mirrors, the other polarization direction could have been rotated and redirected through the system, doubling the total throughput. Maximizing the throughput of the FTS is important because deployment in the field requires a very bright source. Also, if a bright enough FTS source can be made, it would be possible to spectrally characterize multiple telescope feeds at one time, instead of the current procedure requiring they be done one at a time.

Two numbers to keep in mind are the minimum and maximum frequency that can be measured by the system. If one were able to build a system of infinite length and infinite resolution, this would not be a concern. However, any actual device will have a minimum and maximum frequency due to the scan length and step size, respectively. The step size of system relates to the maximum frequency in the spectral response function (assuming perfect polarizing grid efficiency) as:

$$\nu_{max} = c/(4 \times minimum\ step\ size), \tag{3.1}$$

and the maximum single-sided throw gives the minimum frequency as

$$\nu_{min} = c/(4 \times one\ sided\ scan\ distance), \tag{3.2}$$

where the factors of 4 come from Nyquist sampling and the light traverses the path length difference twice because it is reflected back. A useful unit selection for the speed of light in these equations is c = 300 mm-GHz. For example, using equation 3.1 and knowing the minimum step size is 1 mm, it is very straight forward to calculate the maximum frequency of this hypothetical FTS would be 75 GHz. Specifically in IDL the frequency axes in the plots are found as:

$$Frequencyarray = i \times \frac{c}{N \times S \times 10^{-6} \times 2d} \times 10^{-9} \tag{3.3}$$

where i is the index of the sample starting from zero, c is the speed of light, N is the total number of samples and S is the step size from the encoder or inferred from the sample timing and motor speed.

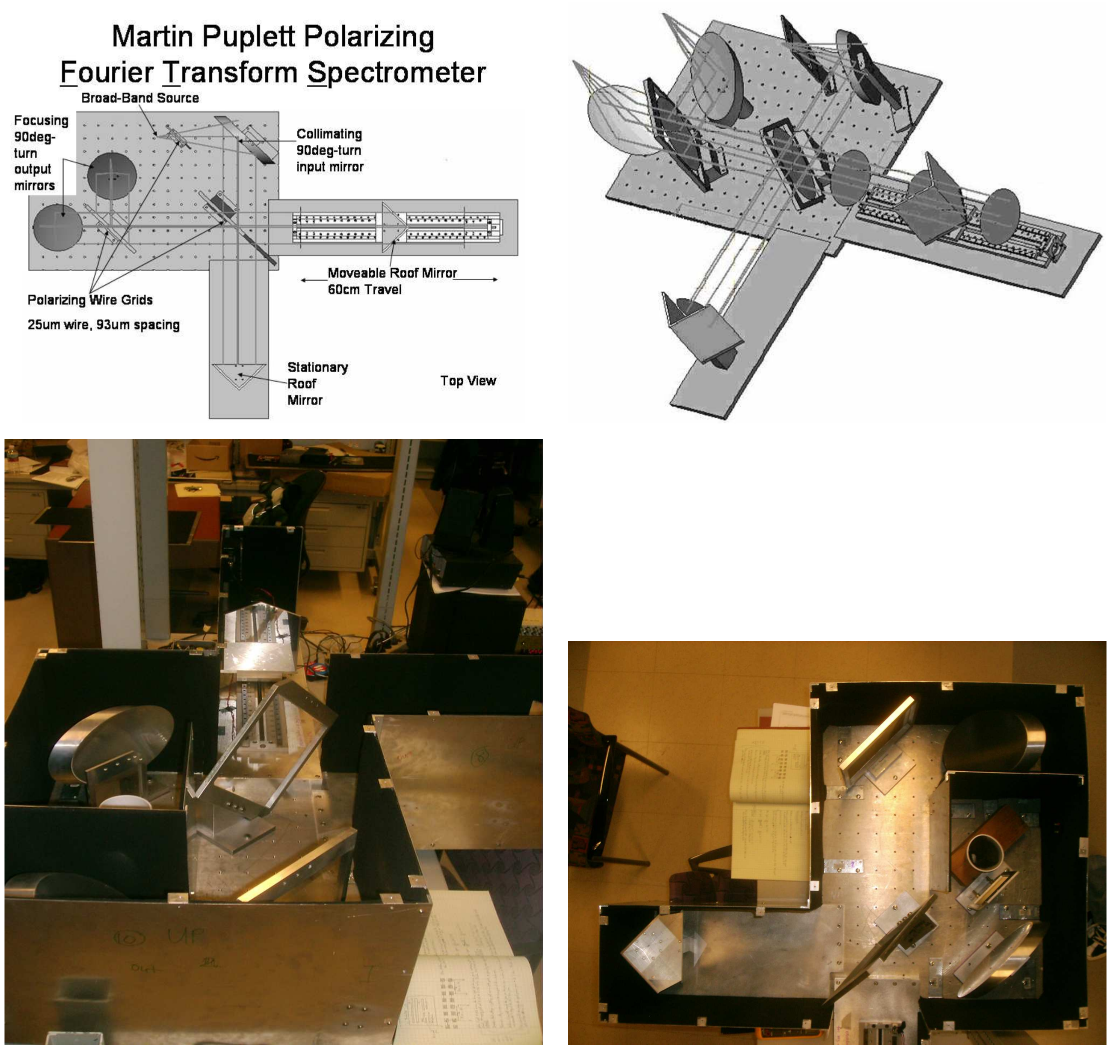

Figure 3.1: Optical design and mechanical layout of the UCSD FTS with two pictures of the actual device. The upper left hand picture shows the layout of the main optical elements including the three polarizing grids, the two roof mirrors, the moveable stage, and the two possible output port positions. The upper right hand picture is a Code V ray tracing diagram used to model and predict the properties of the FTS. Both of these images were made in a cooperative effort with Dr. Thomas Renbarger. The two lower pictures were taken after the device was initially built showing what the real parts looked like, including the walls coated with absorbing eccosorb to cut down on reflections. In the final incarnation of the device, the source (cup of liquid nitrogen-cooled eccosorb) was replaced by a mirror that reflected light from an external hot lamp source.

In practice, the minimum step size is generally smaller than what is needed to reach the maximum frequency for a system. If it is not, it is always possible to decrease this number by getting a better linear encoder system or slowing the motor down and using faster timing circuits. Rather, the grid efficiency and other optical elements limit the maximum spectral response of the system. The minimum frequency measured by the system is more difficult to design because it is determined by the scan distance of the moveable mirror and cannot be changed once the system is built. In order to get a longer travel length, the system also needs to have sufficient throughput. There is no point in having a ten mile long track length if the source is not bright enough to be seen. The other FTS parameter setting system requirements is the frequency resolution of the spectral response. While it would be nice to have 1 MHz spacing, that level of resolution is not needed and would require the track length to be 150 meters long. In the end, the track length was chosen based on the relative resolution of other devices and the practicable device size.

3.1.2 FTS Construction

All optical components for the FTS were made at UCSD while the motor[1] (MDI23), stage[2] (lps_24-20), and external linear encoder[3] (LIDA 477) were made by external vendors. The motor came with some encoder capabilities but the external encoder is much more precise, down to a maximum precision of 1 micron. The main optical stage was donated by Dr. Buffington's group, which had one left over from a previous experiment. The bases for the two arms were designed in Solidworks and fabricated at the UCSD physics machine shop. The walls for the FTS were made by our group using 1/16 inch aluminum sheet metal coated with Eccosorb-LS30. The two mirrors were designed using Code V to have a 12 inch focus rotate the propagation direction 90°. These mirrors were fabricated and polished by the Scripps Institution of Oceanography (SIO) machine shop.

While the design and construction of the mirrors was not trivial, the most difficult elements to fabricate were the free-standing wire grids. These grids polarize and split

[1]www.imshome.com
[2]www.servosystems.com
[3]www.heidenhain.com

the light, and consist of a solid metal frame wrapped with uniformly spaced wire. This type of optical element is available commercially, but they are very expensive and more importantly we could not find a vendor that produced the desired size. The size of the wire grids sets the throughput of the FTS, because the larger the grid the more light that can be transmitted through the system. This meant we had to construct them ourselves.

The frame design for the grids is straight-forward: a simple rectangular frame with a 10 inch by 12 inch opening is machined with two cut off at 45° and with a series of mounting holes drilled through the edges. The 45° cuts make it easier to get the required relative orientation of the grids. Bare tungsten wire, 0.001 inches in diameter and 2500 m long, was ordered from Alfa Aesar Johnson Matthey (PN: 10405), initially costing only $264. Since then commodity prices have driven up the cost significantly so that spools in May 2011 now cost over $1000. The long edges of the frames were rounded so the wire would not be accidentally cut during winding. The surfaces that were going to be in contact with wire during winding were all also smoothed and polished so the wire would not accidentally snag or be cut during winding. Two wire grids were made and fastened together by a set of screws so that for each winding, two sets of wire grids would be made.

Figure 3.2 shows the winding setup used to make the first set of wire grids. The lathe used was chosen because the minimum rotation speed was 30 rpm, much less than most modern lathes allow. I machined a grid holder to smoothly and firmly place the wire grids into the lathe. With the rotation speed at 30 rpm, the cross speed was set so that the wire spacing would be 90 microns, or about three times the wire distance. The most difficult part of the setup was refining the method to transfer the wire from the manufacturers spool to the wire grid. The final method used a smooth ceramic piece, grooved to control the direction of the wire, to feed the wire. The manufacturer's spool was reversed tensioned by a DC motor to provide the correct tension. After the wire grids were finished, a liberal application of epoxy held the wires to the frame so they could be split and used in the FTS. All together I made four separate sets of grids, one smaller set and three larger sets. Figure 3.3 shows images of the first set of small grids that I made. Overall the in-house grid construction quality was very good and allowed for an inexpensive and compact FTS construction.

Figure 3.2: Pictures showing the setup to wind the wire grids for the UCSD FTS. The empty grid frames are mounted into the lathe using an adapter, and as the lathe turns, the cross guide moves the grids longitudinally at the desired rate for a given wire spacing. The spool feed is a home-made ceramic piece designed to smoothly guide the wire from the manufacturer’s spool on to the wire grid. The spool is reverse biased with a DC motor to provide the correct level of tension.

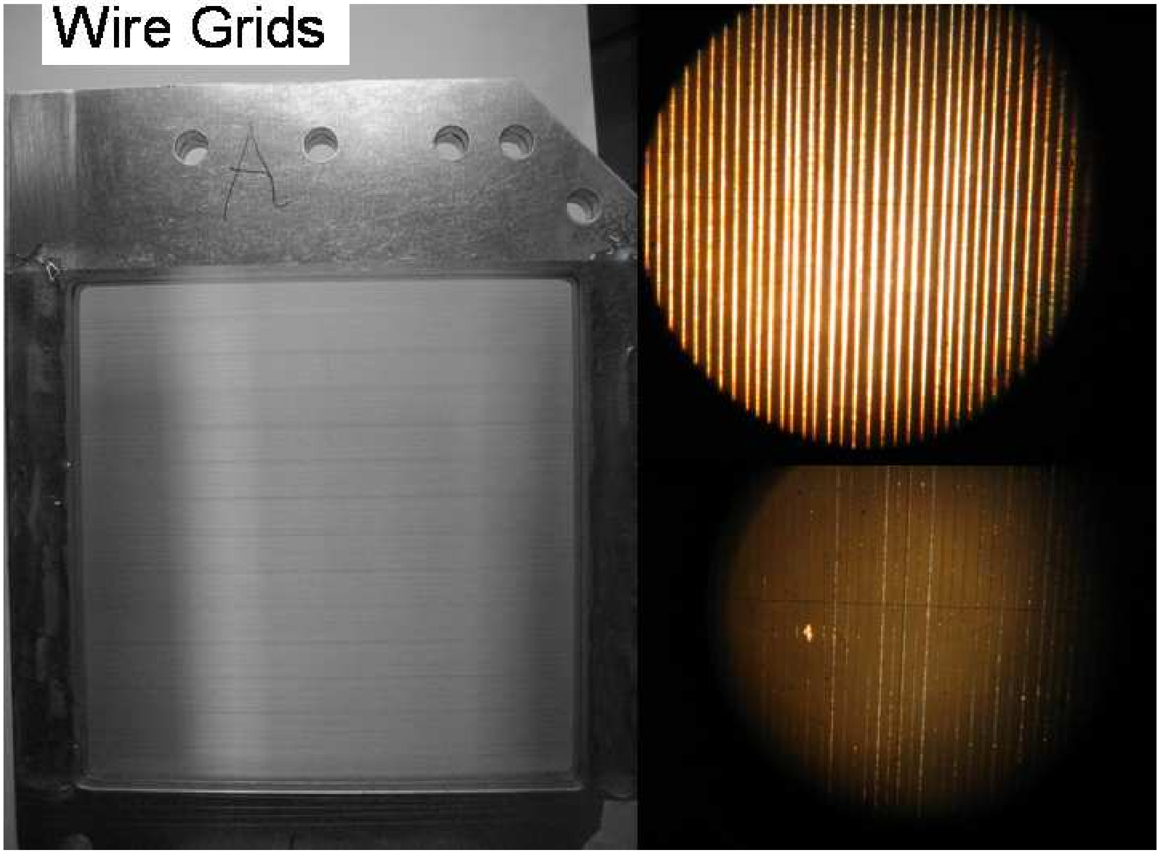

Figure 3.3: The first small grid made at UCSD showing the general shape of the grids and wire layout (left side picture). A digital microscope (upper right) and a measuring microscope (lower right) were used to characterize the quality of the grid and winding process. The average wire spacing is 93 microns with a standard deviation of 23 microns.

3.1.3 FTS Data Analysis

The general operation of the FTS is that of an interferometer. When the two mirror arms are at the same relative distance from the splitting grid, there is no path difference, which leads to all frequencies being constructively interfered. When there is a path-length difference, only frequencies with a full integral number of wavelengths will interfere constructively, while all others will deconstructively interfere to some degree. When a data set is taken using the full track length (Figure 3.4), this will give a measurement of total interference versus distance (called "interferogram"). The interferogram is the time domain partner of the frequency domain spectral response function. Therefore, to get the spectral response function, the Fourier transform of the interferogram is computed. A thorough reading of Bracewell (1986) is recommended for anyone interested in this subject.

There is one confusing point related to coherence. Similar experimental setups are used to test for the coherence length of a light source. Coherence length is the distance light travels while it maintains a given definite phase relationship. If the phase relationship is degraded, it is impossible to get maximum constructive or destructive interference. A spectral response function taken with partially incoherent light is the product of the nominal interferogram multiplied by a Gaussian function whose width is related to the coherence length. This does not affect the UCSD FTS appreciably because the coherence length for typical millimeter-wave source is long compared to the path length difference.

Three separate pieces of software are needed to produce spectral responses from the FTS. First, the stage motion needs to be controlled and set to move in a uniform continuous state back and forth. If the motor is moved too fast compared to the detector time constant or is not moved uniformly, this can lead to unnecessary uncertainty in the resulting spectra. One might think that the motor should move the stage, stop at a particular location, observe at that particular stage position, and then move on to the next spot. However, there is typically 1/f noise in the detector system which makes this sub-optimal and also increases both the complexity of the motor motion and the useful operating time. The motor control software used was initially programmed by sending ASCII text commands to the motor itself, but then a Labview program was written to

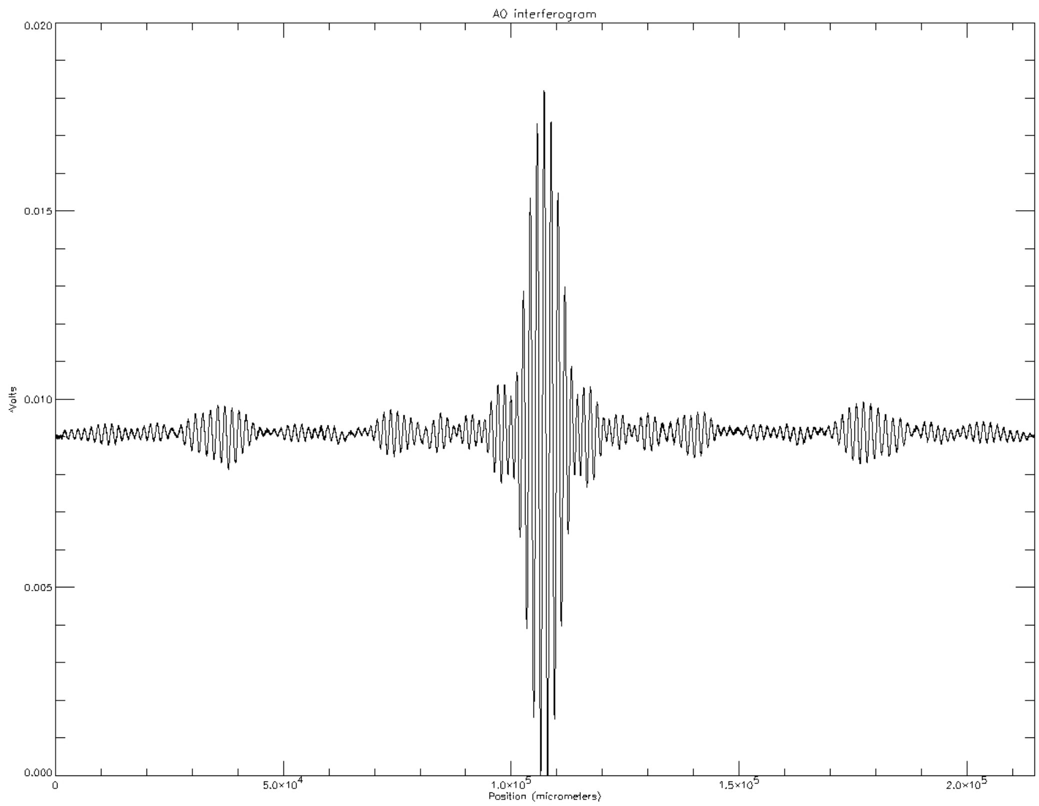

Figure 3.4: An interferogram from the UCSD FTS. The data has been high pass filtered to remove 1/f noise. Ideally, the interferogram is supposed to be completely symmetric about the white-light fringe (peak), but there are small anti-symmetric parts visible. To obtain the spectral response function, the real part of the Fourier transform is computed.

automate and control this process more efficiently. The motor control software need not be run by the same computer as the data acquisition hardware and for all intensive purposes, it is easier to have a dedicated computer system just to control the motor.

The second piece of software reads the external linear encoder and derives the position of the stage. The output of the encoder is a standard two-port quadrature encoder signal. This is similar to sine and cosine giving the phase (direction) and amplitude (location). There is also a home signal that tells the system the stage is at the zero position. Quadrature decoding can be done either in software or in hardware if a suitable board is available. In lieu of a working encoder system, it is also possible to get the approximate position of the stage by using the time stamp of each position and knowing the speed of the motor. This is clearly not optimal but necessary when the encoder system is malfunctioning.

The third piece of software is the detector signal conditioning and Fourier transform. A naive Fourier transform computation from the interferogram will result in highly sub-optimal spectral response function determination. Signal conditioning consists of three components: filtering the data, phase shifting the data, and correcting for non-linear detector response. First, the detector time constant should be deconvolved and the filter applied to the data to minimize the low frequency 1/f contamination. The filtering is a low order polynomial, nominally fourth order. Assuming the motor speed is optimized to place the signal band in a relatively clean part of the audio spectrum, filtering should have minimal effect on the actual measured spectral response function. For example, the BICEP detectors have 1/f knees around $0.1-0.5$ Hz. The time constants of most detectors are around 20ms. These two numbers provided the bounds for the clean part of the audio band signal. For the sake of time and reputability, the scans are done as fast as possible. The lowest electromagnetic frequency of interest in BICEP is no less than 75 GHz. Therefore, the stage is moved at 1 mm/s, placing 75 GHz radiation in the audio band at 0.5 Hz and 750 GHz radiation at 5 Hz. This set the time-scale of one 40 cm scan to be 400 s and nine scans of the same focal plane feed would be one hour.

The data was phase-shifted so that the white light fringe is at zero path length (index number zero in IDL) and the interferogram is symmetric. The symmetric part of the interferogram gives rise to the real part of the spectral response function while the anti-symmetric part gives rise to the complex part. Since the spectral response function is strictly real, any power in the complex portion is noise and can be disregarded. If the interferogram is not phased properly, it is possible to lose real signal or add spurious noise. My phasing algorithm was based on splitting the interferogram in half, computing a χ^2 based on the difference of the two halves, and then doing partial phase shifts in the frequency domain until the χ^2 was minimized. The phase shifting was done in the frequency domain to avoid having to interpolate in the time domain.

Lastly any non-linear detector response was removed. For example, if the source was too bright, the detector responsivity would decrease and would be proportional to the optical power (Q_{opt}) falling on the detector. This can be modeled as a power law:

$$V = AQ_{opt}^{\iota} = AQ_{opt}Q_{opt}^{\iota-1}. \tag{3.4}$$

where by displaying the equation as a product of a linear term and a modified non-linear power term falling on the detector, usage of the convolution theorem is emphasized. A product of two functions of time in real space is equivalent to a convolution of their Fourier transforms or vice versa. This implies the non-linear response creates a harmonic in frequency space with negative power (see Figure 3.5). To remove this effect, one has to assume that there are no actual harmonics of the main frequency response peak and then apply correction factors to the real data that minimized the power at the harmonics of the main frequency peak as seen in Figure 3.5. While this assumption could lead to problems if there were real harmonic leaks in the spectral bandpass, the factors applied are relatively small, ranging from 2% to 4%. Figure 3.5 shows a plot of how the correcting factors affect the raw spectrum and a comparison of a corrected vs. raw spectrum.

3.1.4 2008 FTS South Pole Run

UCSD's Fourier Transform Spectrometer was brought down to the geographic South Pole in January 2008 to take archival spectral responses of all BICEP pixels, derive differential gain factors, find band centers and widths, and characterize spectral leaks. While this goal seems straight-forward, the actual task was not. There was no precedent for how to accomplish the goal and most of the implementation was developed

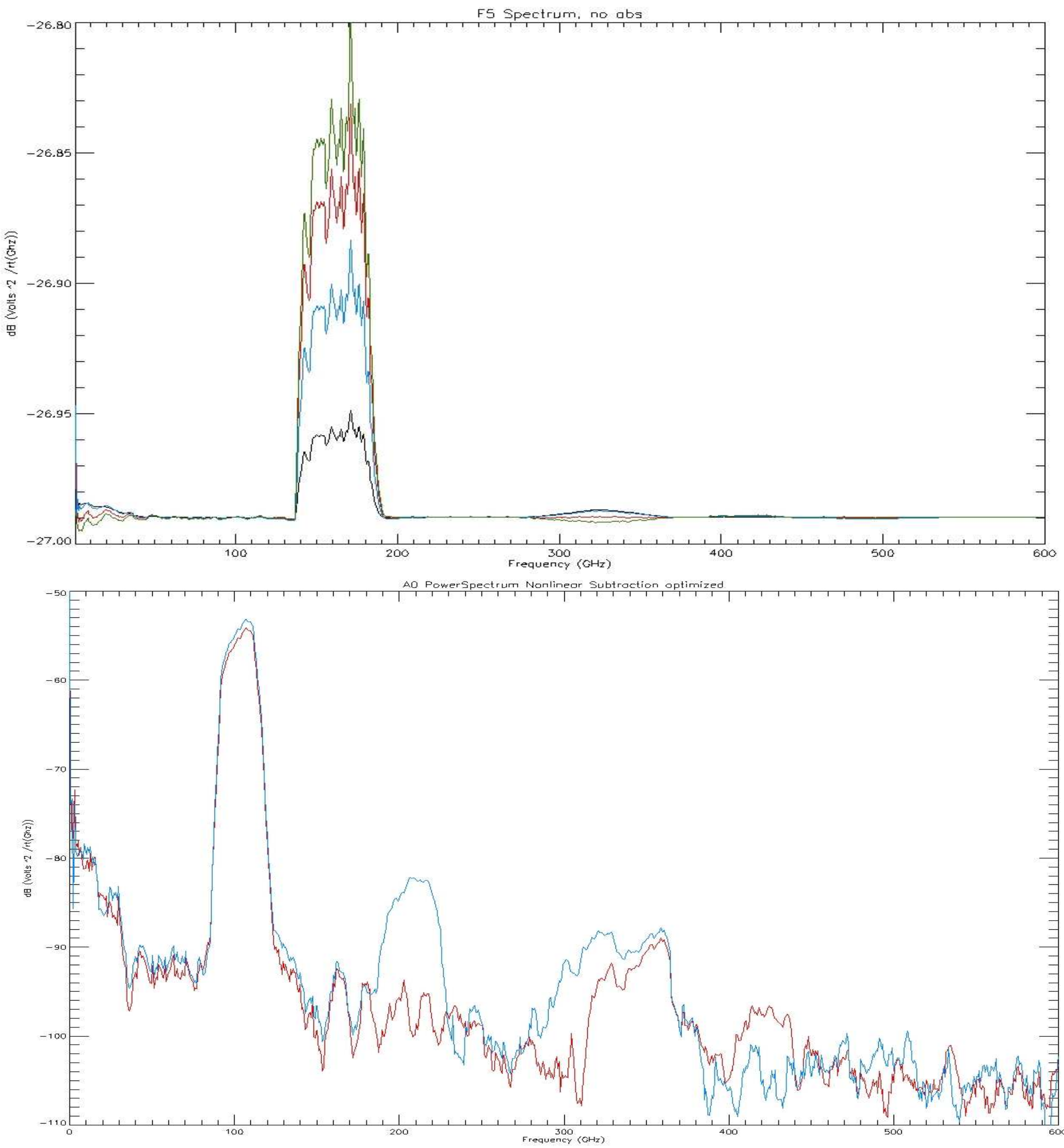

Figure 3.5: Spectral response functions for various non-linear correction factors (top) and a comparison of a raw spectral response (blue) to one (red) optimally corrected for detector non-linearity (bottom). The important point in the top plot is not the amplitude of the main spectral band pass changing but rather the harmonic features that grow in size from a large positive feature to a large negative feature. While it is clear from the bottom plot that most of the large features in the original spectrum (blue) were due to non-linear effects, leaked power at higher frequency remains in the corrected spectrum (red) near 350 and 420 GHz.

on the fly. The issues and solutions devised to successfully implement and use an FTS in the field can be used to improve future FTS deployments.

3.1.4.1 South Pole Setup

The general scheme was to deploy the FTS to the roof Dark Sector Laboratory (DSL), the building housing the BICEP telescope, use a series of mirrors to direct the FTS radiation into the telescope, and use telescope drive to move each feed into proper position (see Figure 3.6). To accomplish this, without damaging the delicate optics and electronics of FTS, it was placed inside of a specially-designed thermal crate to keep it warm. The thermal crate (80” $\times$ 72” $\times$ 36”) was made out of wood and special 3" thick high-R foam called isocyanurate with aluminum foil on both sides. Testing samples of the foam showed it to be fairly opaque at millimeter-waves (even without the foil), so an optical port made of highly transparent zotefoam was patched into the crate on the top. Both a space heater and high wattage heater tape were placed inside to maintain an average temperature of 25° C while the outside temperature was closer to -30° C, or a 55° C (99° F) temperature gradient.

The BICEP telescope does not have the ability to observe at low elevations because of the setup configuration and the fabric boot attached to the telescope, allowing the telescope operator to be inside and warm (seen in the top picture in Figure 3.6). Therefore an oversized “far field flat” mirror (“FFF”, ~4’ by 4’ flat mirror) was constructed and rigidly attached to the telescope mount to reflect the telescope beams down to horizon level. This gave a horizontal beam path out of the telescope, which could potentially directly couple to the FTS if the device was turned on its side or the summing port was used. However, a more elegant solution is to use a “deflection” mirror (30" by 33" flat mirror), attached to the outer ground shield, directing BICEP’s beams down into the thermal box and the FTS crate. The initially setup design called for the deflection mirror to be clamped to the outer ground shield but this did not turn out to be sturdy enough. Instead, the deflecting mirror was attached to a ladder type structure that hung over the ground screen with counterweights and was clamped down for extra stiffness.

The original planned optical setup had a design flaw in that it did not incorporate the parallax of the telescope (Figure 3.7) due to the optical axis not being coincident

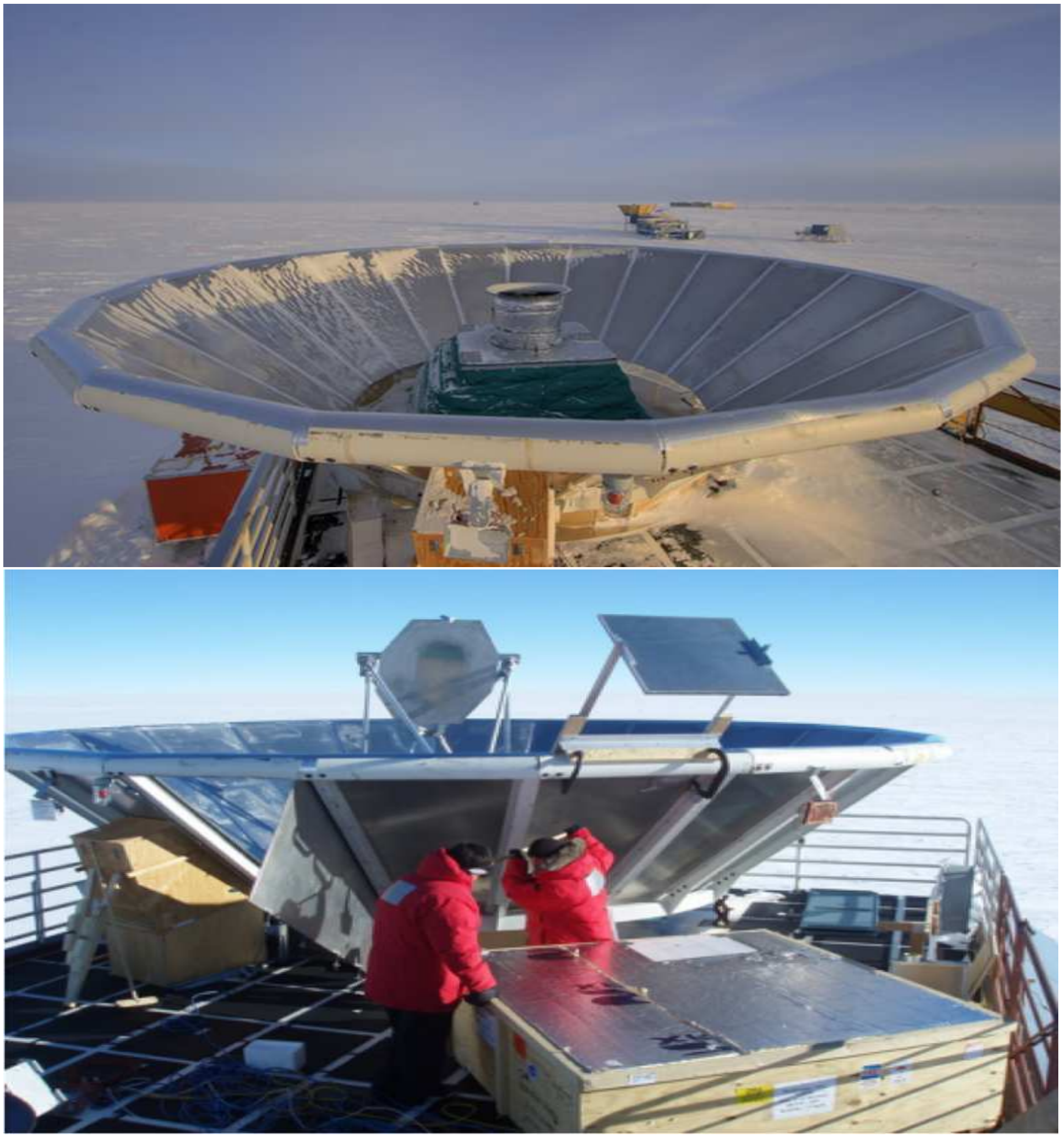

Figure 3.6: Images from the roof of the dark sector laboratory at the geographic South Pole in 2008 showing the BICEP telescope sticking up out of the building with the protective green fabric boot inside of the metal ground screen (top) and the FTS setup (bottom) with its two intrepid operators (Dr. Yuki Takahashi and Evan Bierman). Two mirrors were used to couple the FTS beam to the telescope while the FTS was housed in a thermal crate on the roof to keep the delicate optical and electrical components warm.

with the mechanical axis. This effect is better known from some off-axis telescopes that incorporate this effect to minimize the physical size of a telescopes. The parallax was ~34 cm for the outer pixels compared to the center pixels. This prevented a single optical alignment from being used to characterize all feeds at one time. This effect could be partially mitigated by taking advantage of the degeneracy in the focal plane boresight angle. To a very good approximation, there are six unique radial positions in the BICEP focal plane and 11 unique positions in the focal plane if detector polarization orientation is included (six U positions and five Q positions). However, the set of 100 GHz feeds at 4.1° and 150 GHz feeds at 4.5° were close together and a single focal plane position was used, leaving five unique radial positions and nine unique positions including detector polarization orientation. Each unique position had to be optically aligned separately, making characterization of the entire focal plane more difficult.

The optical alignment procedure is as follows. The center of the deflection mirror was marked and a small circle of eccosorb placed on top while the mirror was tilted up to the sky, thereby giving a large point source signal. The telescope was scanned back and forth in azimuth and elevation until the feed in question was peaked up. The repeatability of this process showed the center of the feed's beam to be aligned to within $\pm 0.1°$.

The next step was to use a plumb bob to find the point directly below the center of the mirror. The eccosorb point source was placed at this point in front of a third mirror directing the beams back up to the sky. The deflecting mirror tilt was changed until the eccosorb source was found. This process consisted of getting the angle approximately correct and then an el-nod was performed to find the change in angle needed to move the mirror. A digital protractor was used to make gross adjustments afterwards. The repeatability of this process showed the center of the feed's beam to be aligned to within $\pm 0.1°$.

Next, the FTS output port was marked on top of the zotefoam window. The plumb-bob mark was used as a guide to move the FTS box into the general correct position (with manual labor help from the South Pole Telescope team). Minor adjustments were made by applying delicate impulses from the knee of the author while Dr. Takahashi relayed the signal size over the radio system. The repeatability of this process

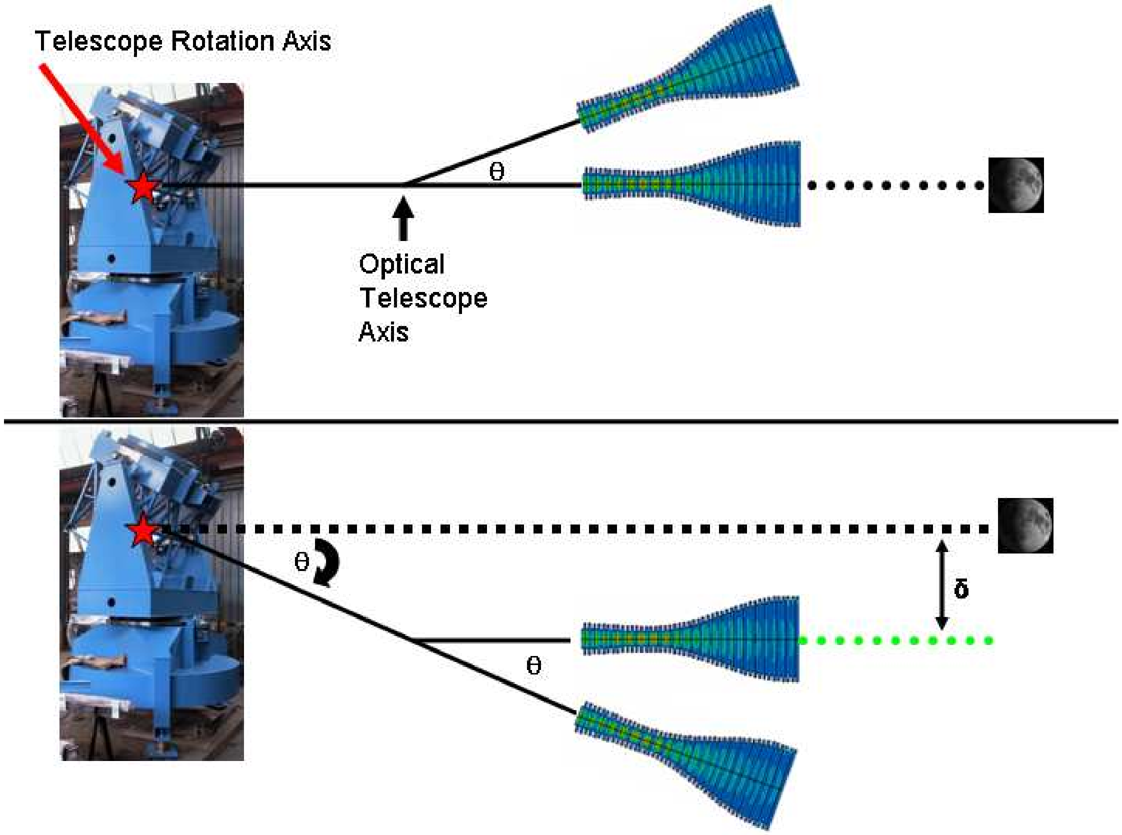

Figure 3.7: Diagram of the telescope parallax caused by the mechanical and optical telescope axes being misaligned. As the telescope rotates from focusing one feed on an object to another, there is a physical translation of the feed, $\delta \sim 34\ cm$. To correct for this effect, the telescope must be rotated by $\phi = \frac{\delta}{D}$, where D is the distance to the source. The angle ϕ is negligible for all astronomical sources, even the Moon, but can cause problems for calibration sources in the near field such as the FTS.

showed the center of the feed's beam to be aligned to within $\pm 0.1^\circ$. From then on, since the FTS was directly below the mirror, it no longer needed adjustments. The angle of the deflecting mirror could then be changed for each unique radius of the focal plane.

Each of the five focal plane radii were optically aligned ("peaked up") by controlling the telescope to point a test feed to the center of the mirror as describe above. The angle of the deflecting mirror was moved to approximately the correct angle by taking the difference between the expected position of the pixel and the measured position of the pixel and dividing by two. The parallax caused the measured position of the feed to be different than the actual position of the feed to hit the same spot on the deflecting mirror. The telescope had to be over-rotated to compensation for the translation from the parallax. This extra rotation angle then had to be corrected for by the deflecting mirror. The angle for the deflecting mirror was half of the full deflecting angle because the beam intrinsically moved by twice the angle the deflecting mirror was moved.

The UCSD FTS has a focusing/collimating mirror as the last optical element (6" diameter, 12" focal length). The spare BICEP back (eyepiece) lens was used to match the beam waist of the FTS to BICEP. A wooden stool was modified to hold the lens, which was placed on top of the thermal crate at the optimal height. The focal length of the back lens was calculated to be 630 mm or 25". However, proper optimal alignment occurred almost 4" further than that calculated distance, a discrepancy that was never resolved. The lens was carefully leveled to 0.1° accuracy using a digital protractor and shims of cardboard.

3.1.4.2 South Pole Setup Troubleshooting

The FTS was disassembled and packed properly for shipping to the South Pole, which meant it had to be reassembled completely upon arrival. For troubleshooting purposes, the FTS was assembled inside the building first, before being deployed to the roof. Immediately it was found that the motor was dead on arrival. Suspected actions of unplugging the serial command cable while the power was still on to the motor is the most likely cause. Unfortunately we had no spare motor so two (one extra as a backup) were ordered and shipped to the South Pole, which took one three weeks (hand delivered by Professor Keating).

The UCSD FTS has an external linear encoder from Heidenhain with standard TTL square waves outputs (called “A”, “B”, and “index”). For noise considerations, A, B and the index all have the inverse signals available with the original signal. The pair are fed into the BICEP Programmable Multi Axis Controller (PMAC) board, which is able to count A pulses and use the B pulse to determine the direction. The count of the index pulse is noted in a separate register each time it is passed and sets the absolute position of the encoder. Calibrating the system before placing it on the roof determined that the precision of running the track back and forth was two microns over a scan of 30 cm. The error was not related to the speed of the stage, but rather the distance, as scans less than 15 cm lost no counts. The velocity of the motor for different settings was carefully checked and calibrated to a very high precision.

Unfortunately, several days after being placed on the roof, the encoder signal became garbled and no longer read useful counts. The origin of this problem was never found but the device did undergo some temperature cycling while initially being placed on the roof. Instead the position alignment was taken from the motor. Microstepping the motor, coupled with the screw pitch, gave a minimum step size of 50 nm (although this was never independently confirmed). Using calibrated motor speed, coupled with the system sample rate of 50 Hz, gave the position of the moving mirror. Since the motor velocity was checked before the device was moved to the roof, the uniformity of the scans was expected to be very close to the predicted positions; however, since the encoder was broken this could not be independently confirmed. Additionally the limit switches for the motor died halfway through the optical setup so extra caution was taken not to drive the motor to the end for fear of damaging the motor. Instead of using the full 60 cm throw of the FTS, only 40 cm scans were done.

Finally, once all these issues were diagnosed and/or solved, and the optical setup of the telescope was done, the FTS placed in the thermal crate and turned on, things were starting to look up. Initial testing of the FTS showed no appreciable signal coming from the device. It was found that the internal optical alignment of the FTS, the height of the moveable roof mirror arm relative to the stationary roof mirror arm (Figure 3.1), had to be shimmed because the metal arms were not completely stiff and the FTS was now sitting on soft foam. Before adjusting the internal alignment of the FTS, the chopped magnitude at the white light fringe was an order of magnitude or so larger than the peak-to-peak size of the white light fringe during a scan. After realignment, the ratio was one-to-one.

The initial spectral responses showed evidence of large non-linearities as the setup with the BICEP telescope is more sensitive than the one used in the UCSD lab. To minimize the non-linearity, the telescope was misaligned slightly so that the total peak to peak interferogram value was no larger than 30 mV. In retrospect, this was a terrible idea as the change in optical alignment can affect the spectral response shapes. Instead, the bulb should have been hooked up to a voltage regulator and the light intensity should have been changed (as suggested by Professor Keating).

After a week of painful manual operation of the telescope and FTS to get detailed spectral responses for each feed, I started the data analysis process. This was clearly a mistake to wait so long but a cursory review of the interferograms and spectral responses showed no initial problems. Figure 3.8 shows plots of some of the problems found in the spectral responses. After changing settings on the scans and reinforcing the deflecting mirror setup, it was found that the deflecting mirror was shaking. The arms holding the mirror had not been made stiff enough causing mircrophonics in the audio band above 400 GHz, making it impossible to fulfill one of the goals to characterize out of band power leakage.

3.1.5 FTS Spectral Response Comparisons

Considering the amount of troubleshooting steps needed to complete the spectral characterization at Pole, the deployment was a success. High quality archival spectral responses of all BICEP feeds were taken, high precision differential gain factors were computed, and the band centers and widths were found. Unfortunately, out-of-band spectral leaks were not characterized with the FTS; however, using the thick grille filter this was determined to be of very little importance. The high precision spectral responses taken for each bolometer showed good repeatability and low statistical error in the measurement process. As a point of emphasis, these spectral responses were key to including the 220 GHz feeds in Chapter 1, showing that hard work can pay off.

Figure 3.9 shows a comparison of the spectral leakage values derived from mea-

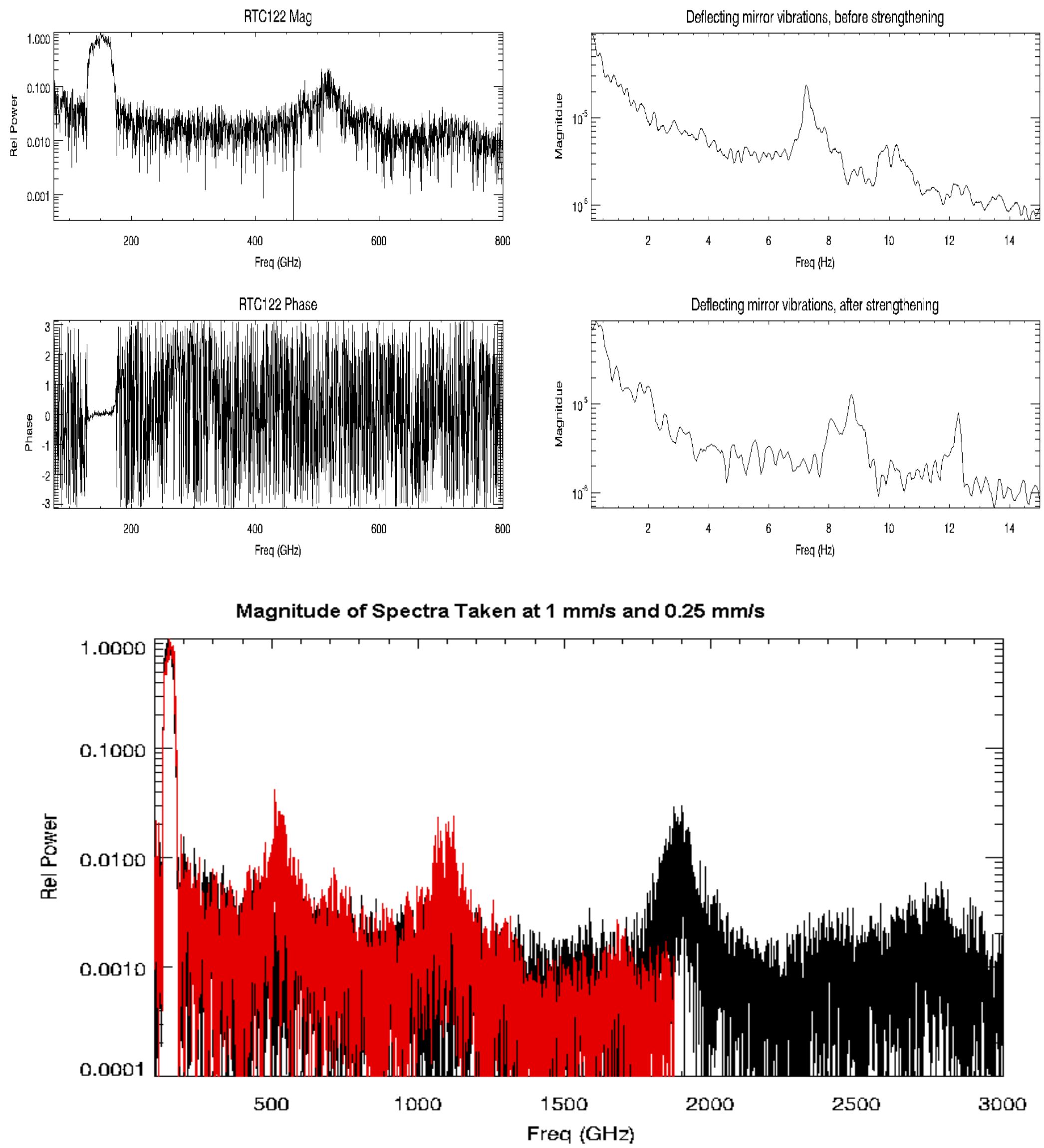

Figure 3.8: Frequency domain plots showing the result of the deflecting mirror setup not being rigid enough. The top left plot shows a sample spectrum magnitude with the phase below it. There is a well-defined phase for the real band pass section but not for the harmonic created by the setup. The upper right shows a zoomed-in view of the feature in the nominal setup configuration and after the setup was solidified more (lower right). Solidifying the setup decreased and moved the feature but it did not eliminate it. The bottom plot shows two spectral responses taken at different scan speeds showing the feature moves with scan speed as opposed to the main spectral response band.

surements at the South Pole as compared to derived from UCSD FTS measurements before deployment. There is no statistical correlation between the two sets showing that either the errors are large on the quantities or there is a systematic change between the measurements. I believe the errors are not the cause of the low correlation because the computed statistical error is small and it was possible to derive a correlation between similar values from CMB anisotropy cross-spectra (Figure 2.1). Rather, this is a good example of how the optical setup and coupling between the FTS and experiment is crucial to having repeatable spectra. Figure 3.9 also shows a spectrum taken by the UCSD FTS and Ruhl FTS before deployment. The difference in FTS resolution is clearly visible comparing the blue and black lines. Even for this single pixel, using a similar coupling setup, there are major differences between the measured spectral response. This problem of a repeatable FTS optical coupling setup is an inherent problem in trying to do the measurements *in situ* as opposed to a controlled environment, such as used with a VNA. Currently there does not exist a reliable alternative method to derive these calibrations.

3.2 BICEP Calibration

My largest and most important contribution to Chiang et al. (2010) was analyzing data taken of the Moon and Jupiter. Mostly, these observations are done to characterize BICEP's beam properties. It is noteworthy to mention that using the Moon for beam calibration is unique to BICEP because the beam widths are so large. For example, it would be nonsensical for the Hubble space telescope to attempt the same process because their beam widths are a tiny fraction of the size of the Moon. For BICEP, the Moon is the brightest and easiest astronomical source to use for beam characterization. Jupiter was also used, and is much smaller in apparent size, but is also much dimmer.

Figure 3.10 shows an example of one set of raw Jupiter observations from one detector and the collage image from all detectors. Many artifacts can be seen the raw image such as imperfect detector time constant deconvolution causing ringing and the ghost image of the main beam. The collage image is made from taking all observations from the entire first season of observing for all detectors and coadding the two arms in a

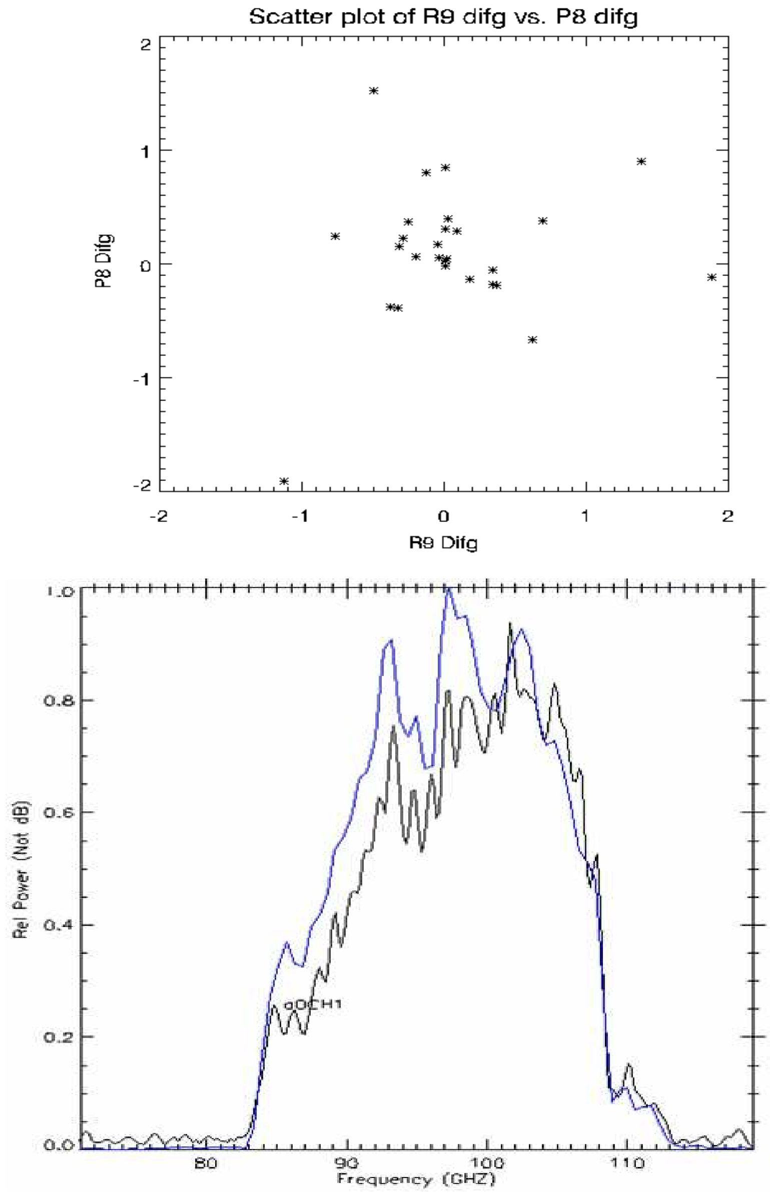

Figure 3.9: Comparison of spectral mismatch for the identical BICEP feeds taken at the South Pole and before deployment (top) and spectral response taken by the UCSD FTS (Black) and Ruhl FTS (Blue) taken before deployment (bottom) for a single feed. The calculated spectral mismatch results from the run at the South Pole and the run before deployment do not agree well. The spectral responses taken with the two different FTS systems before deployment also show many differences. Visual comparison shows the general systematic uncertainty from using different FTS setups, which is a caveat to any system's quoted accuracy.

feed. While the images may seem visually appealing, the signal-to-noise ratio in a given measurement is insufficient to derive precise beam characteristics from Jupiter observations. Specifically, pointing parameters and ellipticities are very difficult to derive, although the main beam size is possible.

The Moon provides a bright astronomical source from which several beam characterizations can be calculated. The brightness of the Moon allowed numerous observations because very little integration time is needed. Each run consisted of eight individual boresight angles maps at 45° intervals. For each boresight angle, the raw data was deconvolved using the time constant transfer functions derived from a different setup by Dr. Yoon and smoothed with Gaussian low-pass filter starting at 10 Hz. The data was split into constant velocity sections and scan direction. The geocentric position of the Moon was used to find the position of the Moon and mask it out while determining a third-order polynomial from each half-scan (see Chapter 1 for more information). The position of the Moon was found by taking each detector, cutting out a window of $\pm 2^\circ$ around the expected Moon center and fitting for a symmetric 2-D Gaussian. This process was iterated once to try and take out any bias from using the "expected Moon center".

While this process sounds straight-forward, I spent nearly two months of time to reconcile the resulting measurements. The left and right going scans had a clear pointing center difference. The cause is due to the detector time constants, which are highly dependent on optical loading. Deconvolving the measured "good" time constants taken under different optical loading conditions was not sufficient to correct these effects in the image. Since no other method of dealing with this problem was found, the average of the left and right going measurements was used. Fortunately, this proved to be quite robust as the resulting point center tracked the boresight angle to a very high degree.

These measurements ended up being extremely important as they showed there was a repeatable differential pointing problem across the entire focal plane. Figure 3.11 shows the collage images of the main Moon beam and the differential Moon beams, which are dominated by differential pointing errors. In addition, the Moon was bright enough to characterize the ghost beam for each feed and even the differential ghost beams, which are mostly dominated by differential ellipticities (Figure 3.12). The dif-

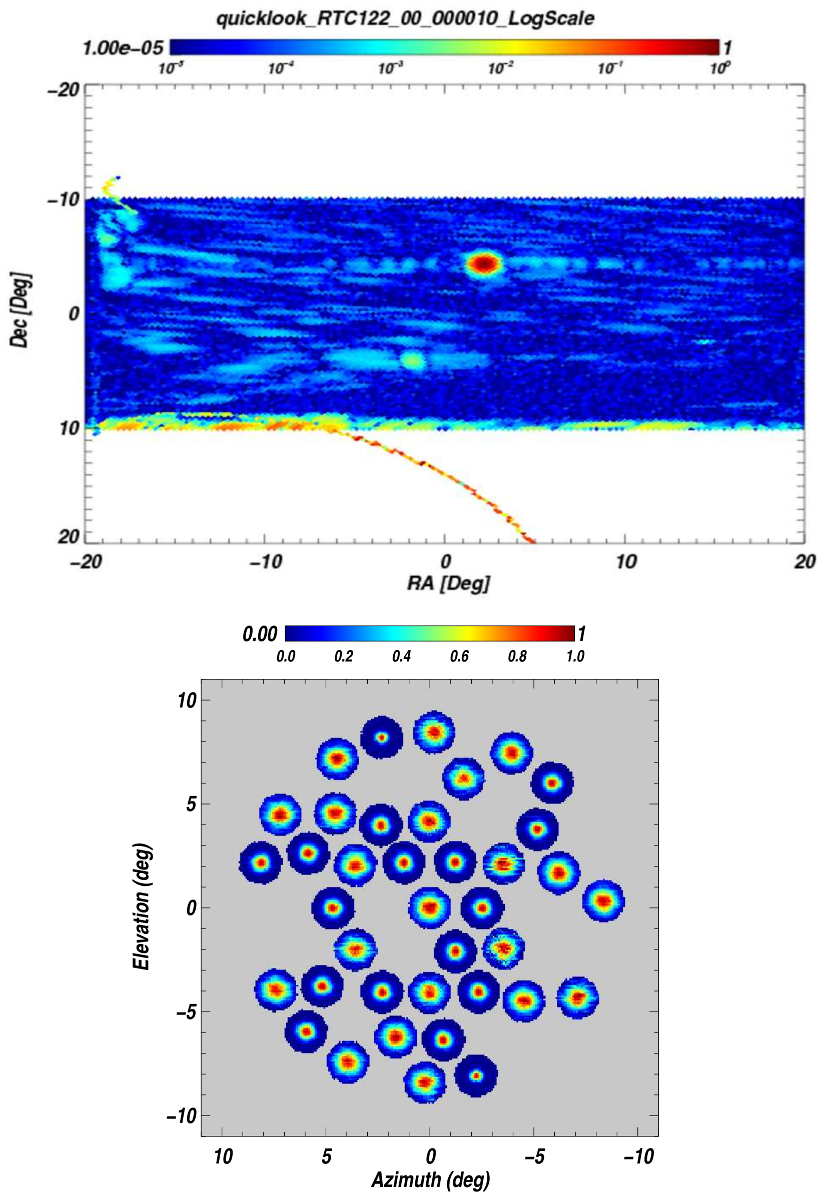

Figure 3.10: Raw observing image from a single detector in boresight subtracted RA and Dec coordinates (top) and collage image of all detectors from Jupiter observations taken with BICEP (bottom). Some of the unusual artifacts in the top image are apparent such as aliased power from the main beam on either side of the main beam due to imperfect time constant deconvolution or the ghost beam power on the opposite side of the focal plane. The collage of the BICEP focal plane (bottom) shows the 100 GHz and 150 GHz feeds are spread across the focal plane, while the two 220 GHz pixels are located at relative RA an Dec of ($\pm 2.5°$, $\pm 9.0°$).

ference in the ghost beam profile to main beam profile due to detector loading differences is apparent from the color scale differences in the figure. The differential pointing parameters taking from this analysis were successfully fed into scan strategy simulations showing that this systematic was a large effect but not quite large enough to hinder BICEP's two-year analysis (Chiang et al., 2010).

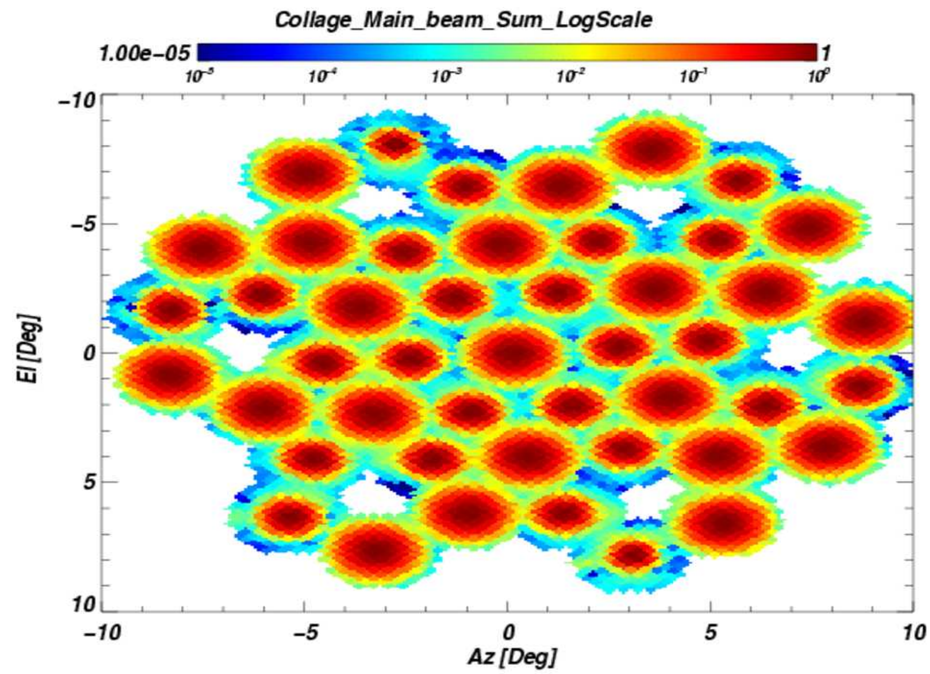

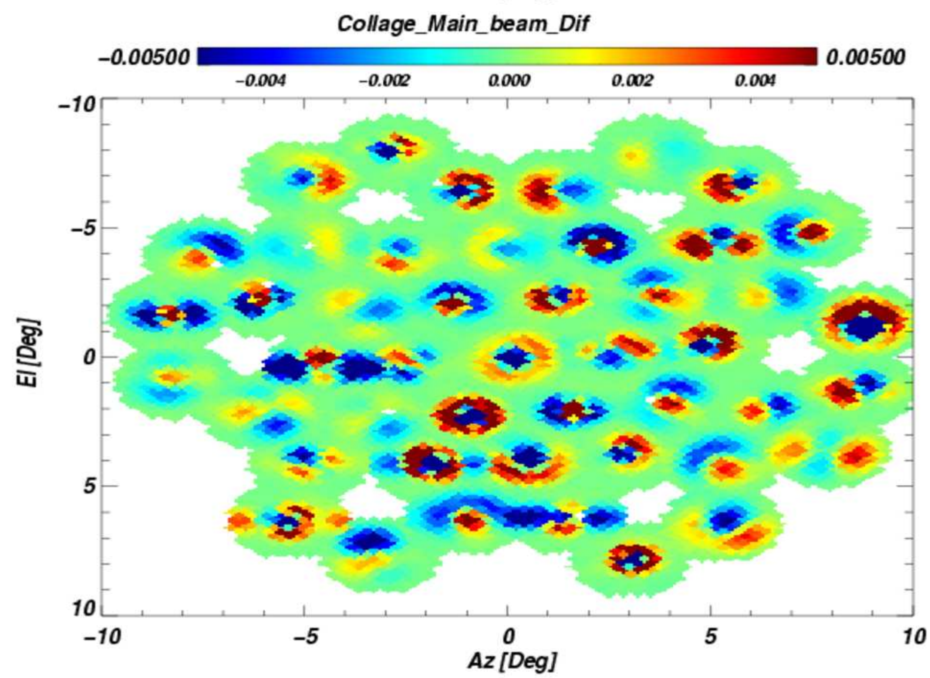

Figure 3.11: Collage image of Moon observations using the sum of the pair of bolometers in a feed (top) and the difference (bottom) normalized so the sum images have a maximum intensity of 1. The difference images are on the same scale as the sum images allowing a direct magnitude comparison. The main beam difference images are dominated by a dipoles feature due to differential pointing.

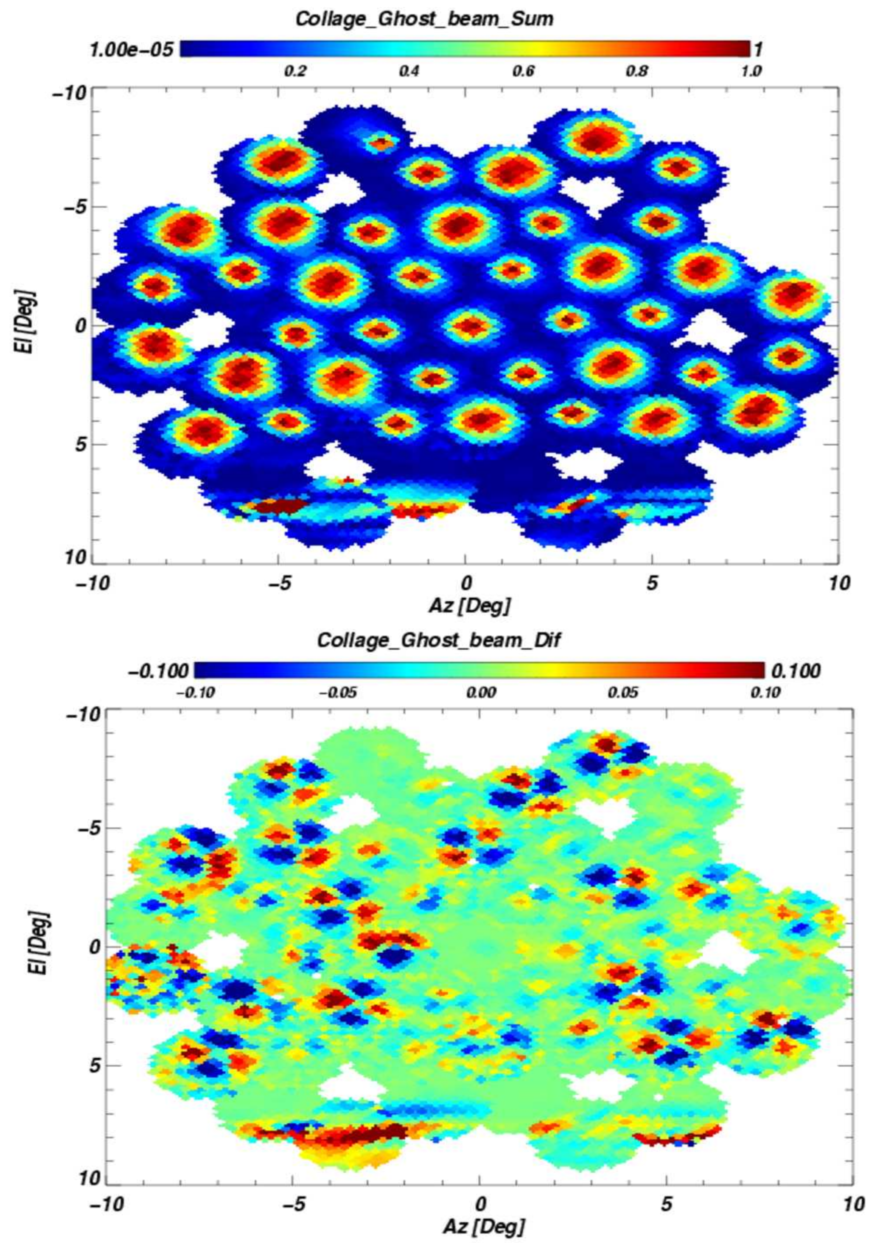

Figure 3.12: Collage image of ghost images of the Moon using the sum of the pair of bolometers in a feed (top) and the difference (bottom) normalized so the sum images have a maximum intensity of 1. The difference images are on the same scale as the sum images allowing a direct magnitude comparison. The main beam difference images are dominated by a quadrupole pattern, most likely due to differential ellipticity. While all of the main images can be seen in Figure 3.11, some of the ghost beam images were obscured because the scan strategy only required the main beam to be visible during.

Chapter 4

Faraday Rotation Modulators and Phaseshifters

Faraday rotation modulators (FRMs) and phaseshifters (Figure 4.1) are devices that use the second-order magneto-optical Faraday effect in materials, first characterized by Michael Faraday in 1845. This effect causes the birefringent properties of a material to change proportional to magnetic field inside of that material. Rotation of an incoming electromagnetic wave's polarization orientation is due to the different index-of-refractions for left and right circular polarizations in the magnetically biased material. The magnitude of the rotation, $\theta = VBL$, is proportional to the intrinsic properties of the material, and characterized by the Verdet constant "V", the strength of the applied magnetic field "B", and length of material traversed by the radiation "L". In devices similar to the FRMs, the magnetic field is applied to a cylindrical ferrite, the active element at the center of the FRM technology, using a superconducting solenoid. The changing field thereby changes the net polarization angle of incoming electromagnetic waves relative to the outgoing waves. The caveat to this is that it is possible to saturate the ferrites such that increasing the magnetic field results in little to no additional polarization rotation. If additional rotation is necessary then only increasing the length of the ferrite or switching to another material can accomplish this.

FRMs in BICEP (Yoon et al., 2006) produce modulation by rotating the radiation's polarization direction relative to the polarization sensitivity of the bolometer in alternating directions. For the phaseshifters in the Millimeter-wave Bolometric Interferometer (MBI,Timbie et al. 2006), the incoming and outgoing polarization angles are automatically set to be 90° apart. Instead of changing the rotation angle, this results in a modulation efficiency that varies from zero (0° rotation) to $> 90\%$ (80° rotation). This defines an absolute polarization angle for the outgoing wave at the cost of decreasing the magnitude of the outgoing wave for imperfect angle rotation. Modulation effected by changing the polarization sensitivity of one arm of the interferometer relative to the other arms. Observing the interference pattern for each combination of polarization directions from all the different arms allows the retrieval of all polarization information possible. The two systems are very different and are employed in different ways but both use the Faraday rotation technology to achieve modulation. The rest of this chapter is focused exclusively on use of the FRMs in BICEP.

4.1 FRM Calibration

4.1.1 Modulation Waveform and Hysteresis

For FRMs, the relative polarization angle can be varied continuously from -80° to $+80^\circ$. To determine the rotation angle, plots of applied current through the solenoid vs. detector voltage (IV curves) similar to Figure 4.2 are analyzed. There are multiple bolometer voltages possible for a given current value because of hysteresis so it is important to fully scan the devices for all possible relationships. Nominally the IV curves can be fit to a model to derive the necessary parameters or, if a suitable source is available, the input polarization can be rotated.

Every magnetic device experiences a memory effect called hysteresis where the changing of the state of the device lags behind due to residual internal forces. This creates a non-deterministic system where for a given current, the rotation depends on the previous internal field state. Clearly this is undesirable for simple FRM operation. For example, if no field is applied to the ferrite, depending on the last state the ferrite was in, it is possible to get up to 20° of rotation in either direction. For continuous polarization modulation, the exact hysteresis curves needs to be precisely characterized for maximum demodulation efficiency. However, the hysteretic effects in the devices were avoided for both FRMs and phaseshifters by biasing with a square wave. A square

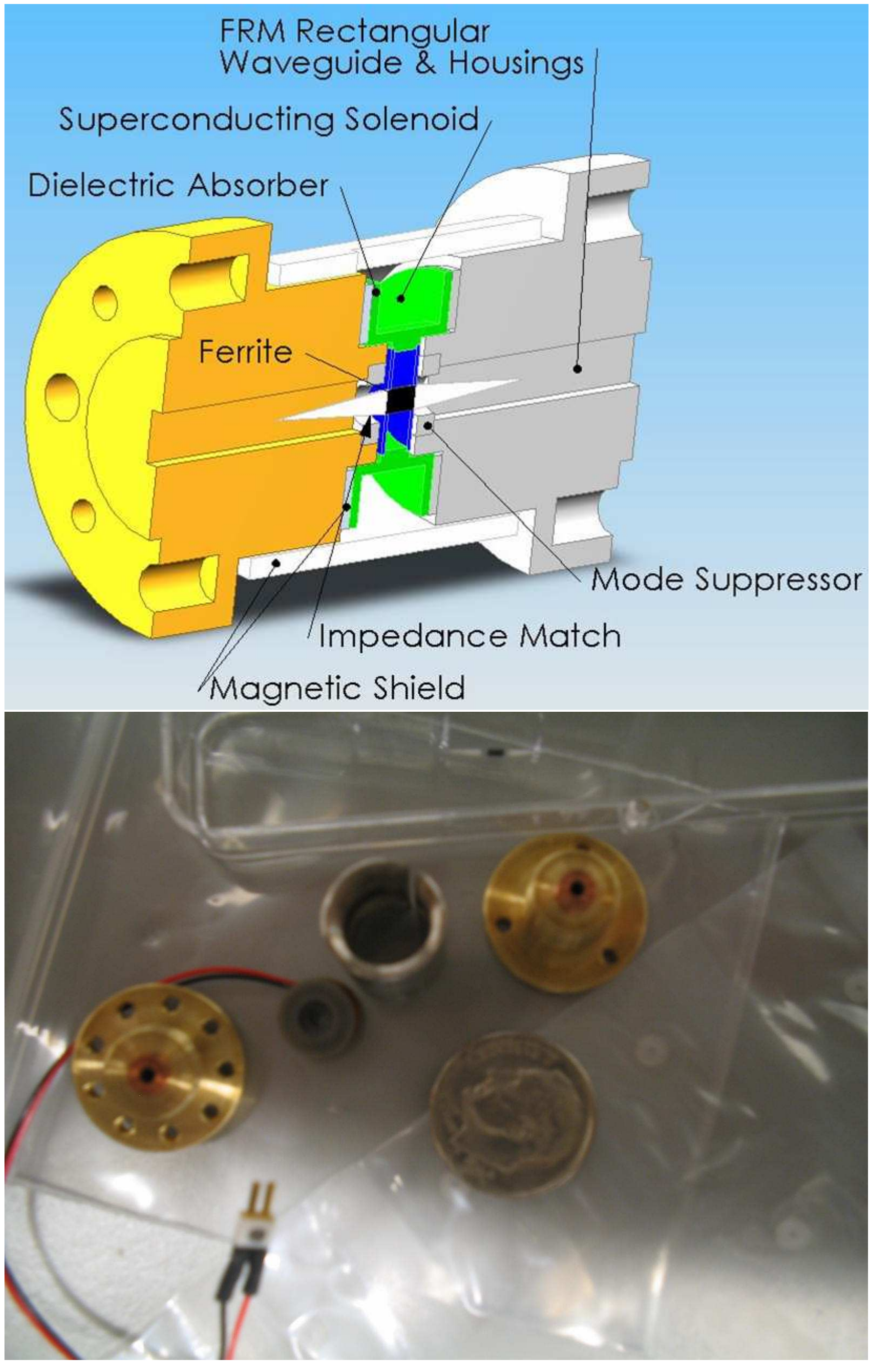

Figure 4.1: Initial Solidworks drawing of the phaseshifter (top) and a picture of the parts of an FRM (bottom). While the phaseshifter has a rectangular waveguide (top), the FRMs have a corrugated circular waveguide housing. Otherwise, the two devices have identical parts and layout.

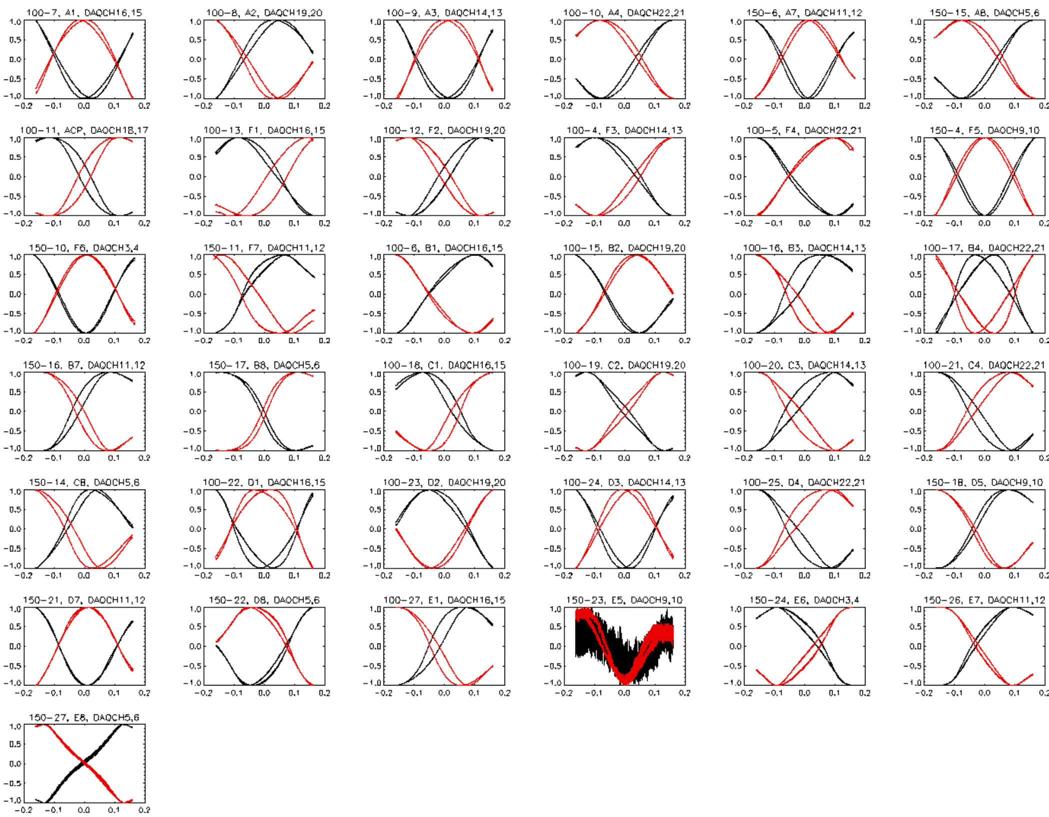

Figure 4.2: Current vs. normalized voltage magnitude (IV) curves for all of the 100 and 150 GHz FRMs during “run 7” (May 2005). The front bolometer (black) is always orthogonal to the back bolometer (red) by design. Hysteresis can be quantified by the gap at zero current between the increasing and decreasing current directions. The input polarization as compared to the bolometer polarization angle sets the overall phase of the curves. Feed E5 is an open circuit so any effect seen is not due to Faraday Rotation. A few feeds, such as F1, have high $1/f$ noise which cause the IV curve to separate at maximum phase.

wave only has two states, thereby removing any uncertainty about the previous state of the ferrite.

The other reason for choosing a square wave is the information transmission efficiency. Classically, a square wave has the maximum information transmission efficiency. For example, a signal $s[t]$ embedded in with white noise $N[t]$:

$$S(t) = s[t] + N[t], \tag{4.1}$$

has a transmission efficiency:

$$\eta = \frac{Signal\ Power}{Total\ Signal\ Power} = \frac{\langle s^2[t]\rangle}{\langle s^2[t]\rangle + 2\langle N[t]S[t]\rangle + \langle N^2[t]\rangle}, \tag{4.2}$$

where the center term in the denominator will go to zero for most signal shapes and noise properties. The average noise can be treated as a constant and pulled out of the expression along with and amplitude for the signal (A) giving an overall normalization factor for the whole expression.

$$\eta = \frac{A}{N}\frac{\langle s^2[t]\rangle}{\langle s^2[t]\rangle + 1}, \tag{4.3}$$

For a perfect square wave with no filtering, $\langle s^2[t]\rangle = 1$ because it is always in an "up" or "down" state giving $\eta = \frac{1}{1+1} = \frac{1}{2}$. For example, this theoretical configuration can happen when the detector sensitivity is 45° relative to the incoming radiation. In comparison, a sine wave ($\sin(\omega t)$) integrates to a value of one-half, giving $\eta = \frac{\frac{1}{2}}{\frac{1}{2}+1} = \frac{1}{3}$.

However, when modulating CMB polarization, the incoming polarization angle is unknown. Therefore, if a square wave is used as the modulation shape there will be moments when the polarization will be modulated between two states of equal value. For example, this configuration happens when the detector sensitivity is in the same direction as incoming radiation. In this case, the transmission efficiency of the square wave is equal to zero because there is no modulation of the signal. The square wave efficiency and resulting transmission efficiency as a function of relative polarization angle (ψ_{rel}) of the detector and incoming radiation is

$$\begin{aligned} \langle s^2[t]\rangle &\propto \sin^2(2\psi_{rel}) \\ \eta &= \frac{\sin^2(2\psi_{rel})}{\sin^2(2\psi_{rel}+1)} \end{aligned} \tag{4.4}$$

giving an average transmission efficiency η = 29% when integrated over all polarization angles equally. If an experiment only chose to measure two polarization angles directly aligned or 45° relative to the radiation the average transmission efficiency would be η = 25%. For a given experiment, the polarization angle coverage will be non-uniform, therefore a simulation of an actual observing strategy would more accurately find the transmission efficiency given a square wave bias and an unknown polarization field for a given experiment. The sine-wave modulation essentially skirts this issue because it already has the loss of efficiency from imperfect polarization alignment taken into account. It does not matter what the detector orientation is for sine-wave modulation because all polarization angles are scanned across. This means that when an unknown, random polarization field is observed, a sine-wave bias for the FRM is more efficient on average than a square wave.

An additional factor not included in the sine wave vs. square wave discussion above is that to generate a perfect square wave bias, an infinite amount of audio bandwidth is needed because there is power in a square wave at higher harmonics than the main modulation frequency. For a sine wave, all power is at the modulation frequency so there is no additional loss of power. Another advantage of a sine wave is that systematic errors due to beam affects or other telescope properties can be mitigated by having full polarization angle coverage. While a sine wave may be more efficient when taken as a whole, a square wave bias has the advantage of being much simpler to implement in practice because it only involves two discrete states, as opposed to the infinite continuous distribution of polarization angles needed for a sine-wave bias.

4.1.2 FRM Demodulation

There are several ways to demodulate a square wave bias, either in the time-domain or frequency-domain. While several methods were attempted in BICEP using various algorithms, the simplest time domain method gave a robust method with decent polarization recovery efficiency. Following is a short discussion of the simple demodulation technique and a few idiosyncrasies specific to BICEP.

The bias signal recorded in the data acquisition system experiences random spikes and dead periods in the time stream. After careful troubleshooting at the South

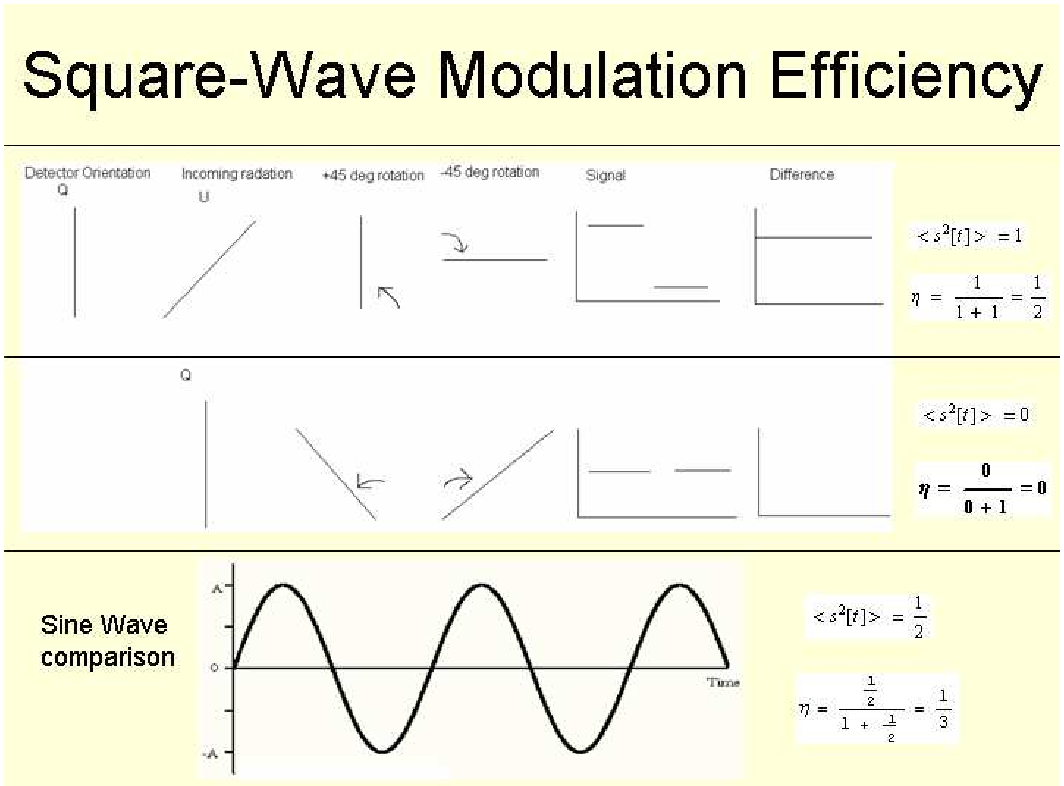

Figure 4.3: An overview of the signal modulation transmission efficiency, $\eta = \frac{\sin^2(2\psi_{rel})}{\sin^2(2\psi_{rel}+1)}$, for a polarization modulator using a square-wave or sine-wave bias. While the square wave bias has an intrinsically higher transmission efficiency, $\langle s^2[t] \rangle \propto \sin^2(2\psi_{rel})$, when scanned over an unknown random polarization angle distribution this is not true. When the relative detector orientation and incoming polarization angle are in the same polarization direction, the net signal modulation efficiency is zero. For a sine wave, the efficiency is also $\frac{1}{3}$ independent of the detector polarization angle because all polarization angles are swept through during the sine-wave bias.

Pole it was found that the problem originates in the readout and not the actual bias board. No solution was found to eliminate the readout problem therefore it has to be corrected by software after data acquisition. The first step in the algorithm for cleaning and analyzing the bias signal is to bandpass filter the entire bias time ordered data stream and then find all the points where the bias crossed zero. The median number of points between each transition is found and any region that did not have the median value (within 10%) is rejected along with the surrounding transitions. Using the transition points, the middle of the resulting regions are found and used as the basis points for demodulation of the data stream. The sign of the transition is also noted to discern between and up or down transition.

Using these basis points from the bias signal, each up and down plateau are split in half and the mean and standard error of the mean are found. The mean of the first half is subtracted from and summed with the mean of the second half from the previous transition. For my analysis “half” is defined by cutting five points from the half before the transition and six points after the transition. These factors were derived from a process of trial and error using elevation nod data to maximize the amount of time used while not creating a noticeable bias in value. The means of the other variables (az, el, psi, etc.) are found from both sets of points used in the two halves. It is very important to keep track of the up or down transition parity because this gives the relative sign of the difference. For normalization purposes, the sum and difference are divided by two to match nominal convention. The time coordinate is derived from the time at each transition, specifically the point before the bias crosses zero.

The result of this demodulation technique is two separate signals. The “sum” signal is the intensity signal and is just a low-pass filtered and downsampled version of the original signal. Since the FRMs only modulate polarization, theoretically nothing needs to be done to extract the intensity data; however, in practice just a low-pass downsampled version of the original data does not look as good as the result of the demodulated data. The “difference” signal is related to the polarization field, but multiple measurements at different polarization angles are needed to fully extract all information. See Figure 4.4 for a view of the modulated waveform parts and the power spectra of the pre-demodulated and post-demodulated signals. Also see Section 4.1.3 for examples of the demodulation process used on el-nods.

4.1.3 Temperature to Polarization Leakage Characterization using El-nods

The FRMs were extensively tested in the lab with man-made calibration sources, but until deployment to the South Pole with BICEP they had not been tested with a true far-field optical source. Before using them to observe low level Galactic and CMB polarization, it was necessary to test them on a larger magnitude source to refine demodulation software and characterize the devices. An ideal source for this is the Earth's atmosphere. El-nods (see Section 1.3.2) were done with the FRMs before every scan-set, giving a large set of calibration data over different weather conditions to analyze the properties of the FRMs.

A normal el-nod moves the telescope up and down in a sine-wave pattern with an amplitude of one degree causing a change in atmospheric loading proportional to the cosecant of the elevation. For non-FRM channels this pattern can be fit for a slope, yielding calibrated timestreams. For FRM channels, when the FRMs are modulating, the resulting signal is more complex, as can be seen in Figure 4.5. These modulated el-nods produce unique calibration data, which is not possible to gather for the channels without FRMs. The atmospheric el-nod is an unpolarized $\sim 100mK$ signal, therefore there should not be any modulation visible. Any modulation seen in Figure 4.5 is an indication of systematics in the system or FRM. The signal must first be demodulated and split into intensity (Figure 4.6) and polarization (Figure 4.5) data.

The analysis of the demodulated data consists of low-pass filtering the signals and elevation data in the frequency domain in software. The magnitude of the el-nod is then derived by treating the filtered elevation as the bias signal to lock-in to the el-nod signal in the intensity and polarization data. The signal seen in the demodulated polarization data is a direct measure of the intensity to polarization leakage (called "instrumental polarization" or IP). Again, it is not possible to derive the IP for the non-FRM pixels because they do not have modulation that unambiguously splits the intensity and polarization data simultaneously. This brings to mind the famous quote, "ignorance is bliss".

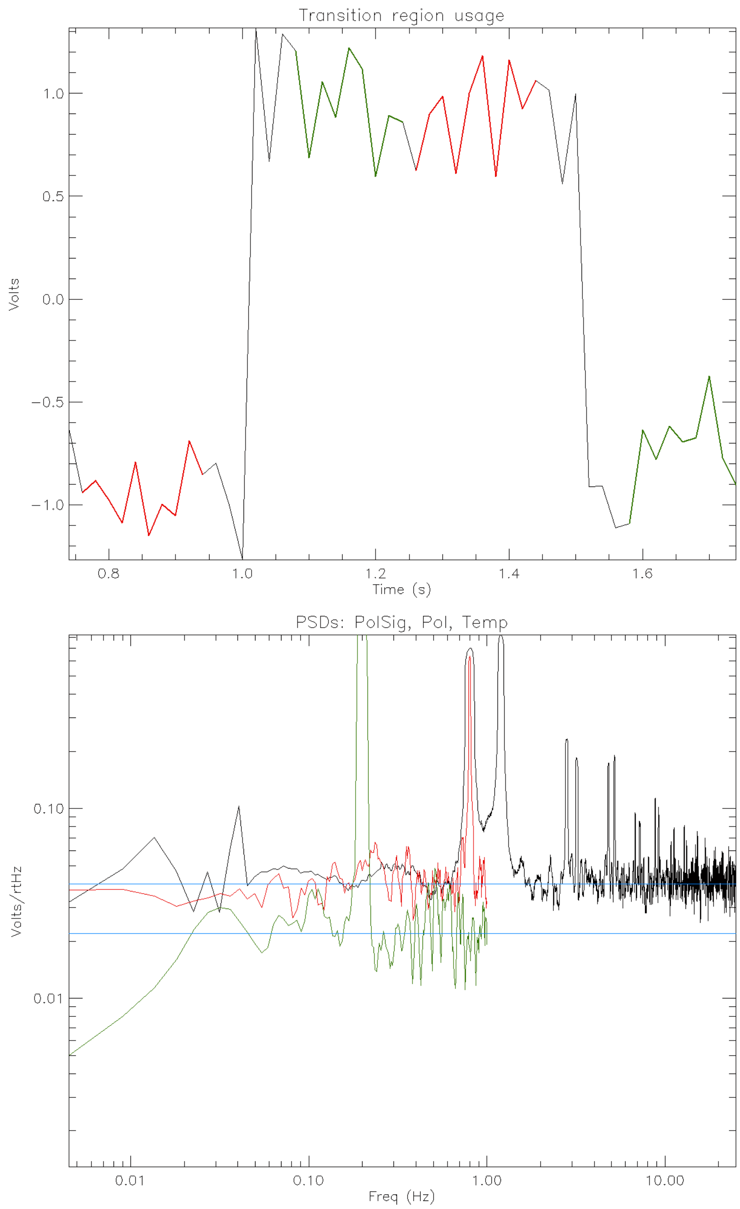

Figure 4.4: The square wave bias from the FRMs and power spectra of the pre and post-demodulated signals. The top plot is an average looking transition split into parts by up or down transition and before (red) and after (green) the transition. The average of the red and green sections are found and differenced, multiplying by the sign of the transition (up or down). The bottom plot shows the power spectra of a pre-demodulated signal (black) with the intensity data (red) and polarization data (green). This plot shows that the intensity demodulation is essentially a smoothing and downsampling process while the polarization signal cannot be seen in the pre-demodulated signal.

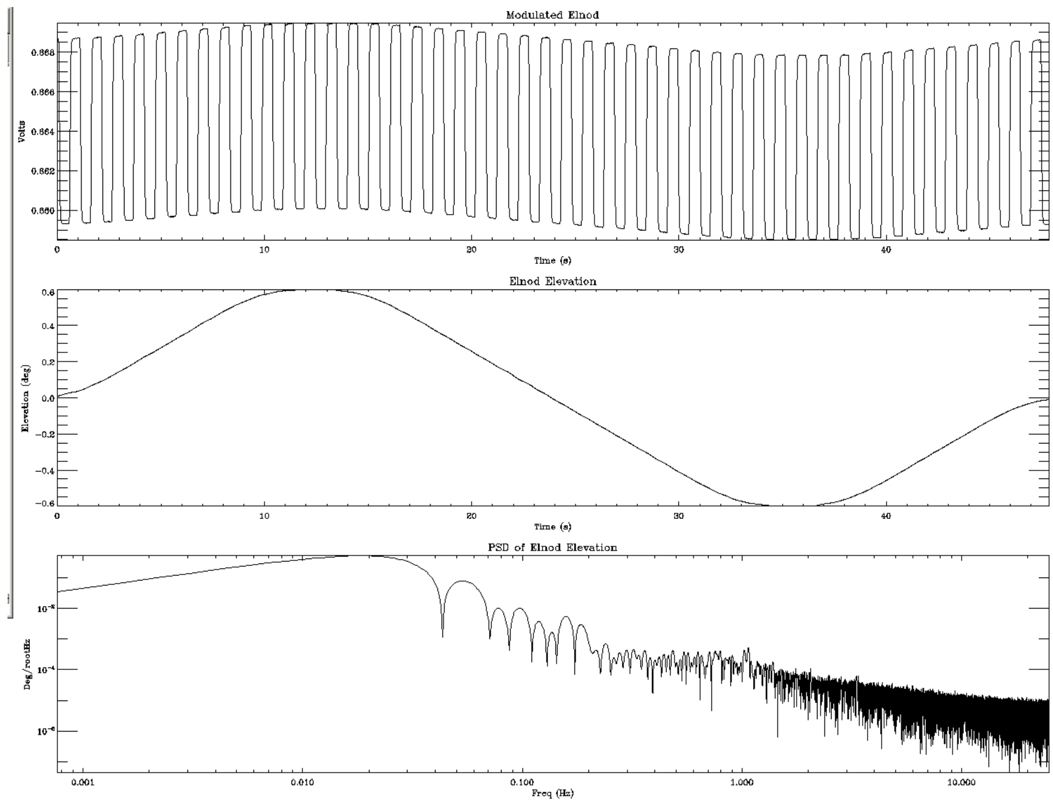

Figure 4.5: El-nod implemented with the FRMs turned on (top) shown with the telescope elevation drive register (middle) and power spectra of the pre-demodulated signal (bottom). The atmosphere is unpolarized and the FRMs only modulate polarization, meaning that any modulated signal seen here is a systematic from the telescope or FRM.

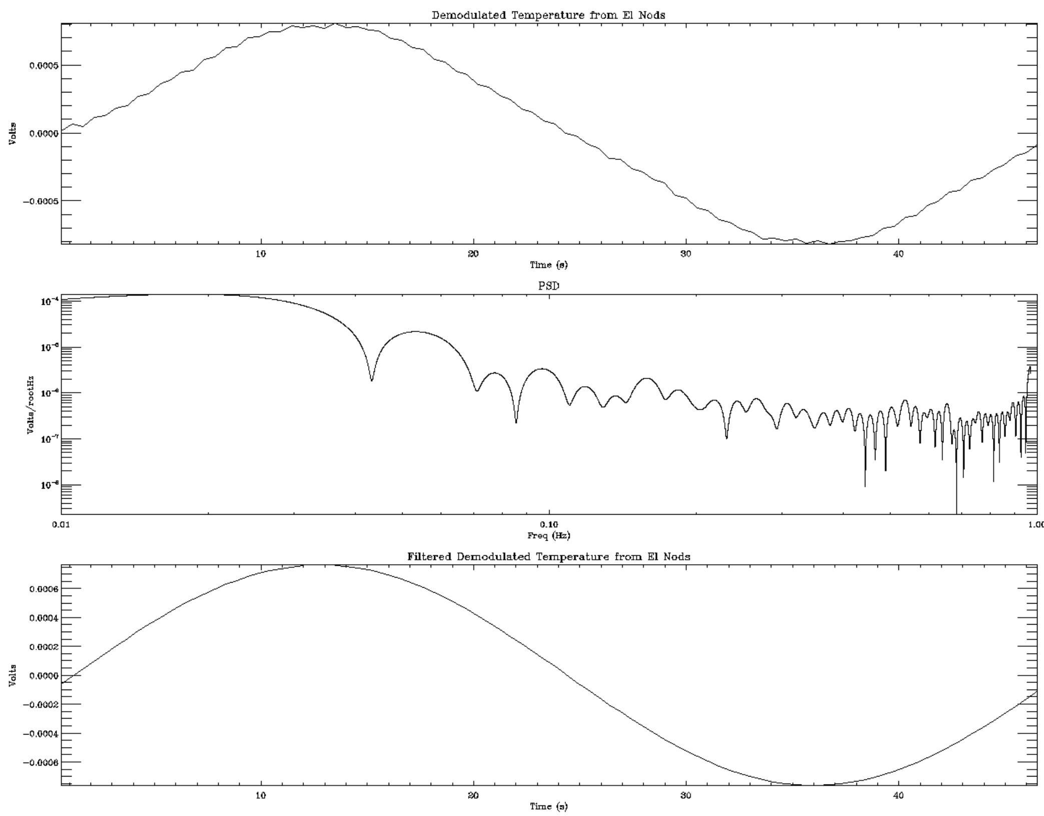

Figure 4.6: The unpolarized intensity of an el-nod after being demodulated (top) with the power spectra (middle) of the raw demodulated signal and the time stream of the filtered intensity data (bottom). The magnitude of the el-nods are found by low-pass filtering the signal and elevation data and then performing a software lock-in to the elevation data. Since the elevation nod is nearly a sine wave, this filtering and lock-in maximize the ability to recover the el-nod magnitude.

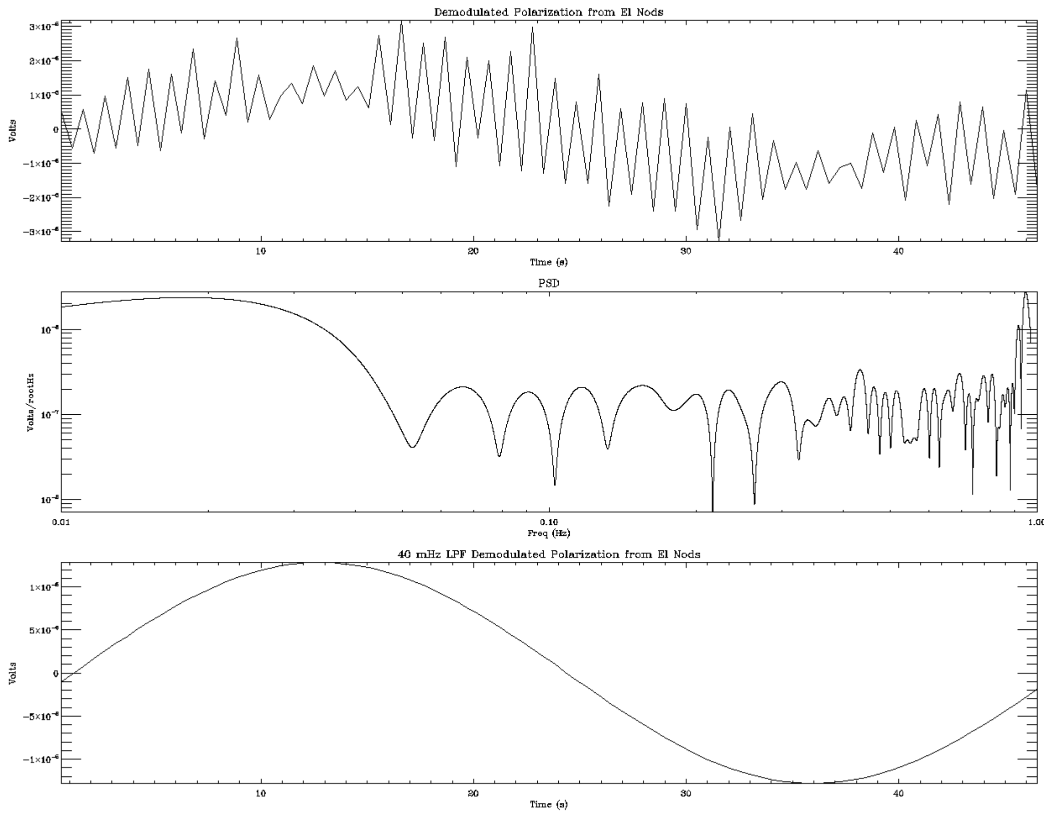

Figure 4.7: The polarized intensity of an el-nod after being demodulated (top) with the power spectra (middle) of the raw demodulated signal and the time stream of the filtered data (bottom). The DC component of the demodulated signal has been subtracted, which accounts for nearly all the spurious signal seen in Figure 4.5. There is residual high frequency power due to aliasing that is easily removed by low-pass filtering. The magnitude of the filtered demodulated polarized signal is derived in the same manner as the intensity data so that the two values can be directly compared. The amplitude in the bottom plot therefore gives a direct measure of the intensity-to-polarization leakage (also called “instrumental polarization”).

The first step in the analysis process is to make sure the effect is real, and not an artifact. The magnitude of each intensity and polarization el-nod for each scan-set is carried out at a different elevations. These magnitudes are found and plotted as a function of elevation center as seen in Figure 4.8. The el-nod magnitude is proportional to the elevation, which causes the atmospheric loading to change. If this residual signal is inherent to the FRM, it would not change systematically with elevation. While the modulation can give positive or negative power depending on the phase of the bias, the general magnitude of the slope in Figure 4.8 shows the recovered intensity of the el-nod is most-likely real. Figure 4.8 shows a nearly identical trend of polarization el-nod magnitude vs. elevation. The fact that the polarization magnitudes generally follow the intensity magnitude confirms that this is true leaked el-nod intensity signal into polarization.

The ratio of the el-nod intensity and polarization signals gives the IP for each channel. This value was derived for each FRM run separately as seen in Figure 4.9. Each run occurred under different observing conditions, showing the robustness of this method to calculate IP. Some channels had relatively large IP, which could possibly prevent them from being used to measure low-level polarization. However, this method characterizes the IP for each channel to a very high level, allowing the possibility of removing this effect in future data analysis. Since the leakage can be measured so easily and with such high precision, this effect is potentially much easier to remove as compared to the leakage from spectral response mismatch in Section 1.3.3. Additionally there would be no spectral response mismatch because the modulation allows differencing of the signals from the same channel as opposed to two different channels within a feed.

4.1.4 False Noise from Fourier Transform Spectral Leakage

During initial testing of the FRMs, elevated white noise levels in all the devices were detected. Some of this was misunderstanding due to a Fourier transform effect most often called “spectral leakage”. An example of this is shown in Figure 4.10, a discrete square wave will not necessarily produce a series of delta-function like spikes in the periodogram. Applying a Hanning filter, which is approximately a cosine function,

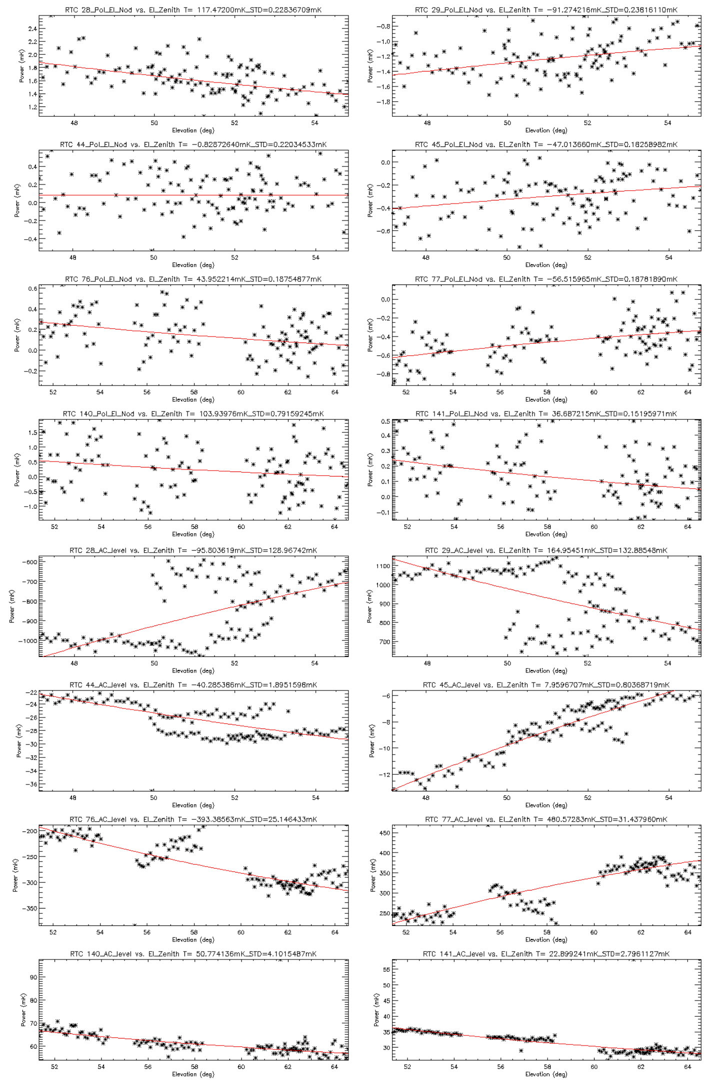

Figure 4.8: The el-nod magnitudes from four working FRM feeds in BICEP from a single FRM run over all scan-sets taken at different elevation centers. The top set of eight plots are the power from the unpolarized intensity of the demodulated el-nods at the different scan-set elevation centers showing the general trends of decreasing magnitude with elevation (atmospheric loading) and that the sign of the demodulated power is opposite sign for the two arms within a feed. The bottom set of eight plots are the power from the polarized intensity of the demodulated el-nods at the different scan-set elevation centers. Taking the ratio of the values from the two sets of plots give the value of the intensity to polarization leakage, which can be large for several channels. The sign of the leakage is a free parameter and changes from one feed set to the other.

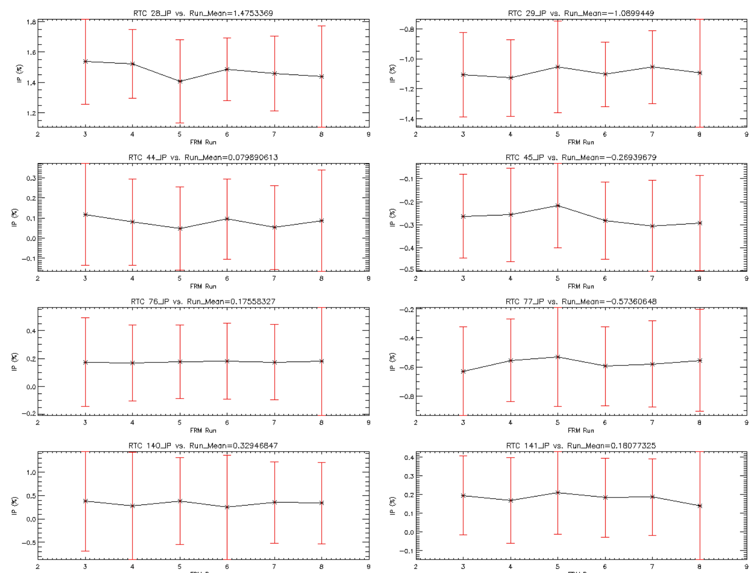

Figure 4.9: Plot of IP derived from el-nod data for each of the FRM runs with good data. The red error bars are the standard deviation of values within a run, not the error in the mean. The error in the mean values can be seen as the run to run variation in the derived IP value. IP is detected with high significance in all channels. The simplest model of IP predicts the two arms in a feed will have opposite signs, as can be seen for RTC 28 and 29. RTC 140/141 does not show this simple relationship but these channels were flagged bad based on other calibration data as well, Regardless of the FRMs.

decreases this effect by making the ends of the data stream go to zero. If one did not know about this effect, the black curve in the lower right hand corner of Figure 4.10 could easily be mistaken for construction defects in the FRMs.

Further investigation into the noise properties of the FRMs was carried out using observational data taken from installed feeds in the BICEP telescope during the first observing season in 2006 (Section 4.2), showing no excess noise is detected using the 100 GHz FRMs.

4.1.5 FRM Modulation Angle Calibration

FRM modulation efficiency is maximized for $\pm 45^\circ$ rotation and it is important to calibrate the devices well for this to occur. To this end, a rotating dielectric sheet calibrator (Takahashi et al., 2010) was used to input a small changing polarized signal. The coupling of the dielectric sheet calibration to the BICEP telescope was an accomplishment utilizing a wide variety of techniques or personnel.

While the calibrator was rotating, the FRMs were square-wave biased as shown in top plot of Figure 4.11. For each separate FRM bolometer the raw time stream is divided into “up” and “down” states. Once the time stream is split, each half is analyzed exactly like they were separate bolometers by taking the position in the focal plane and the calibrator angle and fitting to the expected functional form. From this fit the effective detector polarization angle sensitivity is derived. The process was repeated for different FRM current bias levels until the rotation angle was optimized. The final rotation levels for some FRMs were off by as much as a degree because the current-biasing electronics only had 256 discrete current levels leading to current jumps of up to several degrees in some cases.

4.1.6 FRM Spectral Response

Before deployment a full integrated test run of the telescope was performed at the Caltech High Bay, as discussed in Section 3.1. Ideally, it would be best to do a dedicated testing of the system without the FRMs, then insert the FRMs and do another round of testing. Since such resources were unavailable, only a single run with six

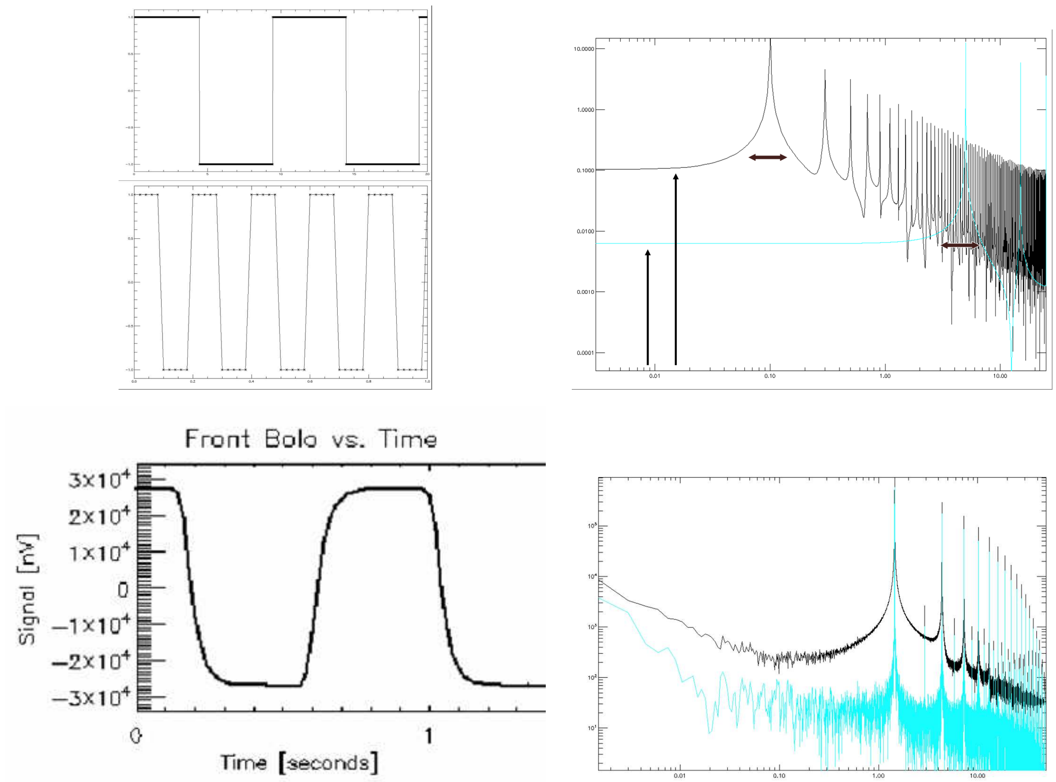

Figure 4.10: Spectral leakage of simulated and real data. The upper left hand plot shows simulated discrete square waves. The upper right hand plot shows the periodogram of those two square waves. The arrows are pointing out both the elevated noise level and broadening of the peak. As the frequency increases, this spectral leakage effect decreases for a given square wave magnitude. A infinitely long continuous square wave in time produces singular peaks in frequency space. This is not true in practice because the time series is truncated and sampled at discrete intervals. The lower left graph show a plot of a portion of a front bolometer of an FRM feed's voltage signal vs. time. The right is the periodogram of the data (black) and with a Hanning filter applied (blue). The Hanning filter counteracts the spectral leakage effects by damping the ends of the time ordered data stream.

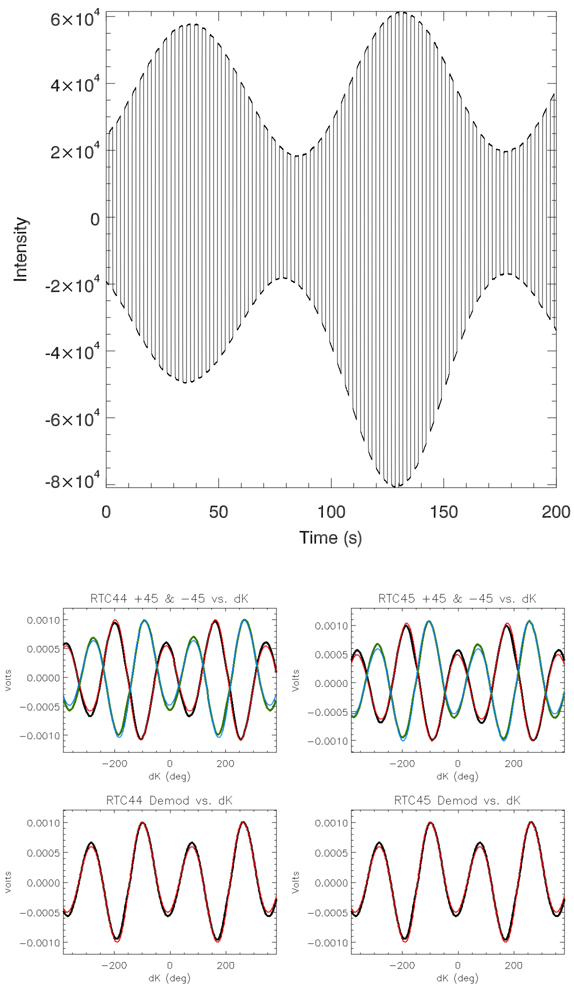

Figure 4.11: Dielectric sheet calibration time streams (top) and demodulated signals (bottom two rows) used to calibrate the FRM rotation angles. Each demodulated time stream is fit as a separate detector where the fitted model is over plotted for each detector.

FRM pixels was accomplished. Figure 4.12 shows the average spectral response of the feeds without FRMs compared to the feeds with FRMs. The nearly identical spectral responses in the two cases shows the FRM spectral response is nearly flat, to within the precision of the measurement.

One caveat is the FRM spectral responses are taken without any applied magnetic field. This was an oversight in planning as spectral responses should be collected at many different bias levels to compare the relative spectral response of the FRMs in different cases. The net spectral response of the devices should be flat as a function of bias frequency; however, Gault et al. (2011) showed the spectral response of a phase-shifter can change as a function of bias. Effects from biasing the FRMs can possibly affect the spectral response such as differences in bolometer loading.

4.2 Observing Runs

There were eleven FRM runs during the 1006 austral winter. The first two attempts were "test" runs. The first two successful runs used a scan strategy focused on the entire "Gal-bright" field (See Chapter 1). The next six runs focused the FRMs on a small patch in the Gal-bright region where there was a large polarization signal expected. The last run focused on Eta Carina in the Gal-weak region; however, this run had pointing problems so no useable Galactic data resulted. By the fifth run, the focus of the FRM runs was to detect Galactic polarization from a single FRM feed at 100 and 150 GHz, while modulation was occurring. There was only one fully working FRM channel at 100 GHz, and two at 150 GHz. While data is automatically taken for all the channels, the telescope scan strategy focuses a single FRM feed on the Galaxy. This is necessary because significant integration time is needed to detect polarization using only a single feed therefore focusing the scan strategy so only two FRMs cover a small patch of sky maximized integration time per FRM channel.

4.2.1 An Example FRM Run

The first full FRM run resulted in almost 17 hours of useful data for each of the six feeds. A modulation frequency of 1 Hz was used, which was a tradeoff between

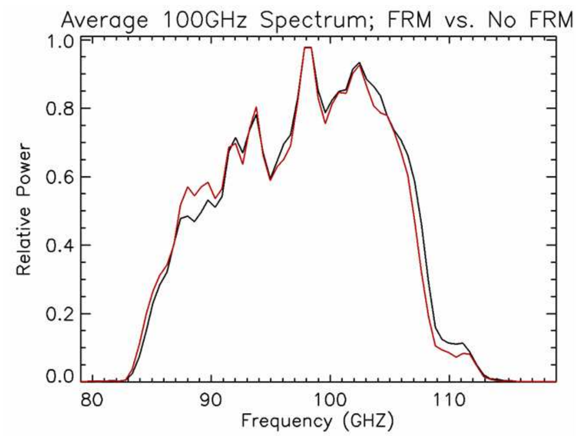

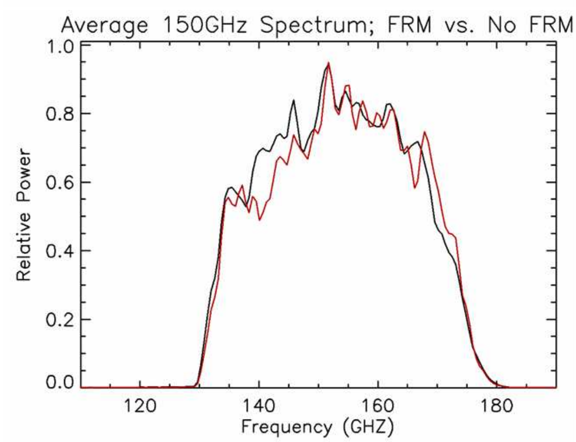

Figure 4.12: Average BICEP spectral responses for 100 and 150 GHz taken with and without FRMs in the focal plane feedhorn stack. This data was taken nearly simultaneously implying that the detectors are different for the FRM and non-FRM pixels. On average, the spectral responses compare very well to each other implying a very flat spectral response for the FRMs.

$1/f$ noise in the intensity data and the bolometer time constant's effect on the square wave bias for the polarization data. El-nods (Section 1.3.2) were used for calibration during the runs. The demodulation scheme used summed and differenced the two different square wave states in the time domain. Approximately 40% of the data was cut during the square wave transition region. Additionally, for both the square-wave sum and difference data, a third order polynomial was removed. The two bolometer arms were not summed and differenced as was done for the nominal data analysis method.

Two separate methods are used to evaluate whether the FRMs had higher noise levels after demodulation. Both methods are based on comparing the FRM data when they are being biased versus when they are not being biased. An FRM off-state occurs before and after each scan set. There is approximately a six second window before the bias function starts but after the telescope stops moving, and about six seconds after the biasing was stopped but before the telescope is moved, where the FRMs are not biased and the telescope stationary (the "off-state" data). Since the on- and off-state data are taken so close in time to each other, there is no change in atmospheric or telescope conditions making the comparison more robust. For each uni-directional scan and off-state, the periodogram is computed and the median value between 0.08 and 0.13 Hz is computed (called "spot-noise"). The average ratio of the median spot noise with the FRMs on and off is 1.47 at 100 GHz and 2.01 at 150 GHz. The ratio at 100 GHz is expected because the demodulated data is the difference of a single time stream, adding the noise in quadrature between the "up" and "down" states, resulting in a factor of square root of two. This noise ratio is computed for each bolometer arm separately, so when data from both arms in a feed are summed, the combined noise is the same as if the two arms were differenced and not modulated. Unfortunately, the origin of the excess ratio at 150 GHz is not known.

4.2.2 All FRM Runs

The FRMs underwent a long series of lab tests, construction iterations, and characterizations with both bright polarized and unpolarized sources before deployment. However, they had yet to detect polarization from an astronomical source. To achieve this "cherry on top" in addition to the other testing, four consecutive runs concentrated

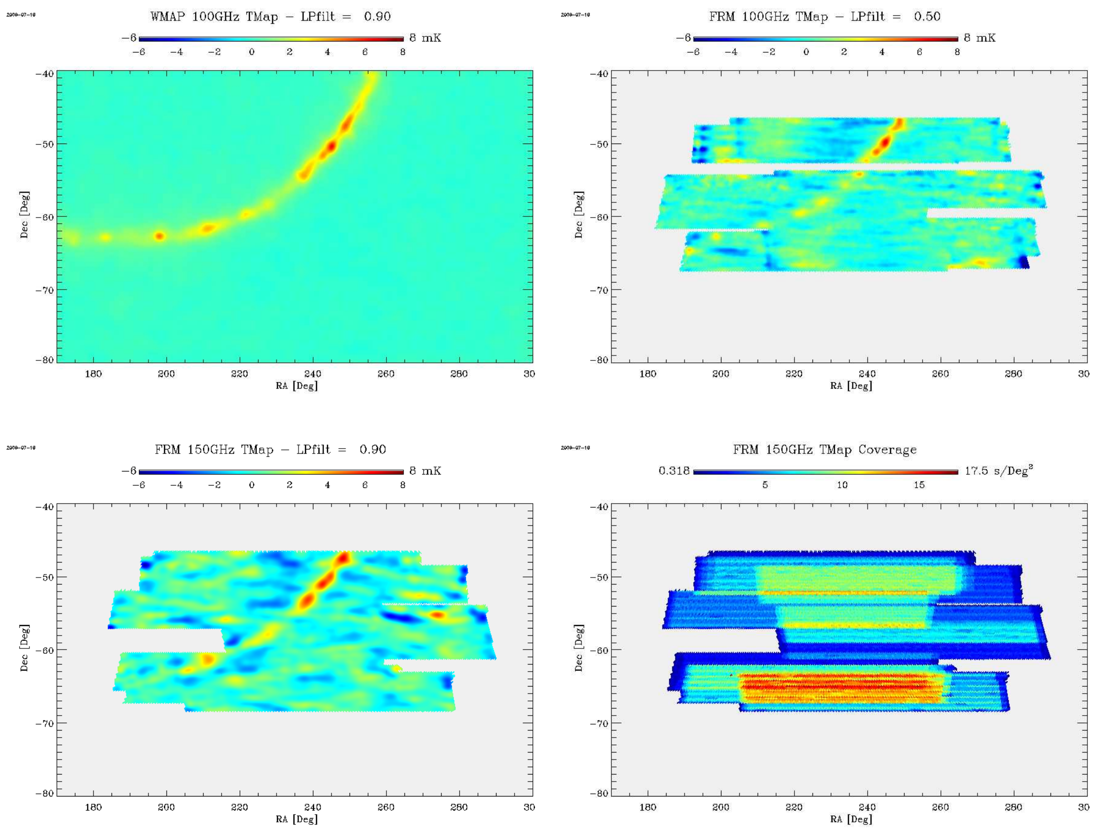

Figure 4.13: Maps from the first full 48 hour FRM run of BICEP using five of the six FRM feeds (one feed had a bias that was not working). The upper left plot is from a WMAP W-band three year map simulation accounting for BICEP filtering effects but not possible demodulation effects. The upper right hand plot is from BICEP 100 GHz FRM feeds while the lower left is from 150 GHz FRM feeds. The lower right hand plot is an example of the coverage of the feeds on the sky. As expected because of integration time and noise levels, no polarization signal could be seen from either BICEP band (maps not shown).

a single feed on a very small patch of the sky for only one 150 GHz and one 100 GHz feed with FRMs. Using maps from three-year WMAP observations and first-year BICEP observation made from feeds without FRMs, the center of the small observing is chosen to be at an RA and Dec of 243° and -51° respectively ($\ell \approx 332°,\ b = 0°$). An interesting point about this choice is that it wasn't clear at the time why this observing center had relatively low intensity compared to the surrounding area. In retrospect, the study of Galactic polarization from Chapter 1 explains why this is true.

For each full run, each 100 and 150 GHz feed observed the region in one of two polarization angles. Since only two boresight angles can fully recover the polarization properties in a map pixel, only two boresight angles were used in the scan strategy. The penalty for this was the inability to remove systematics with more boresight angles or possibly having a large difference in observing time at one boresight angle versus another for, certain weather patterns.

The final analysis of these runs focuses solely on the single 100 GHz FRM feed because it has the lowest 1/f noise and can be directly compared to WMAP. At the time of this analysis the pipeline was relatively immature compared to Section 1.3. There are no corrections for spectral leakage and the polarization angle treatment assumes the two measurements exactly at 45° with ideal polarization modulation angles of ±90°. The boresight pointing of the telescope is from the raw encoder values not corrected with data from the optical camera. The feed locations use design parameters not the more precise ones derived from CMB observations. No simulations of possible pointing, beam, or modulation systematics is performed. A single WMAP simulation from their three-year observations is performed, assuming no modulation and ideal feed and polarization angle position. The filtering does not include any masking, subtracting a first order polynomial from each half-scan. The scan length was so short that a zeroth order polynomial subtraction was considered; however, this was never fully implemented with all the data.

Figure 4.14 shows the final result of this analysis. Comparison to WMAP shows good general agreement in intensity and some general similarities in polarization, except for the minor boresight pointing errors for BICEP. The detection of polarization was deemed significant compared to the noise by comparing the individual maps from the four runs separately. The main polarization feature was seen in all four sets of maps. The detection of astronomical polarization is in some ways a validation of the technology; however, the lack of a rigorous observing campaign still leaves some unanswered questions about low level residual systematics that could still plague these results. The limited amount of time spent on the analysis pipeline also leaves open the door for more advanced analysis techniques that could enhance the viability of similar devices.

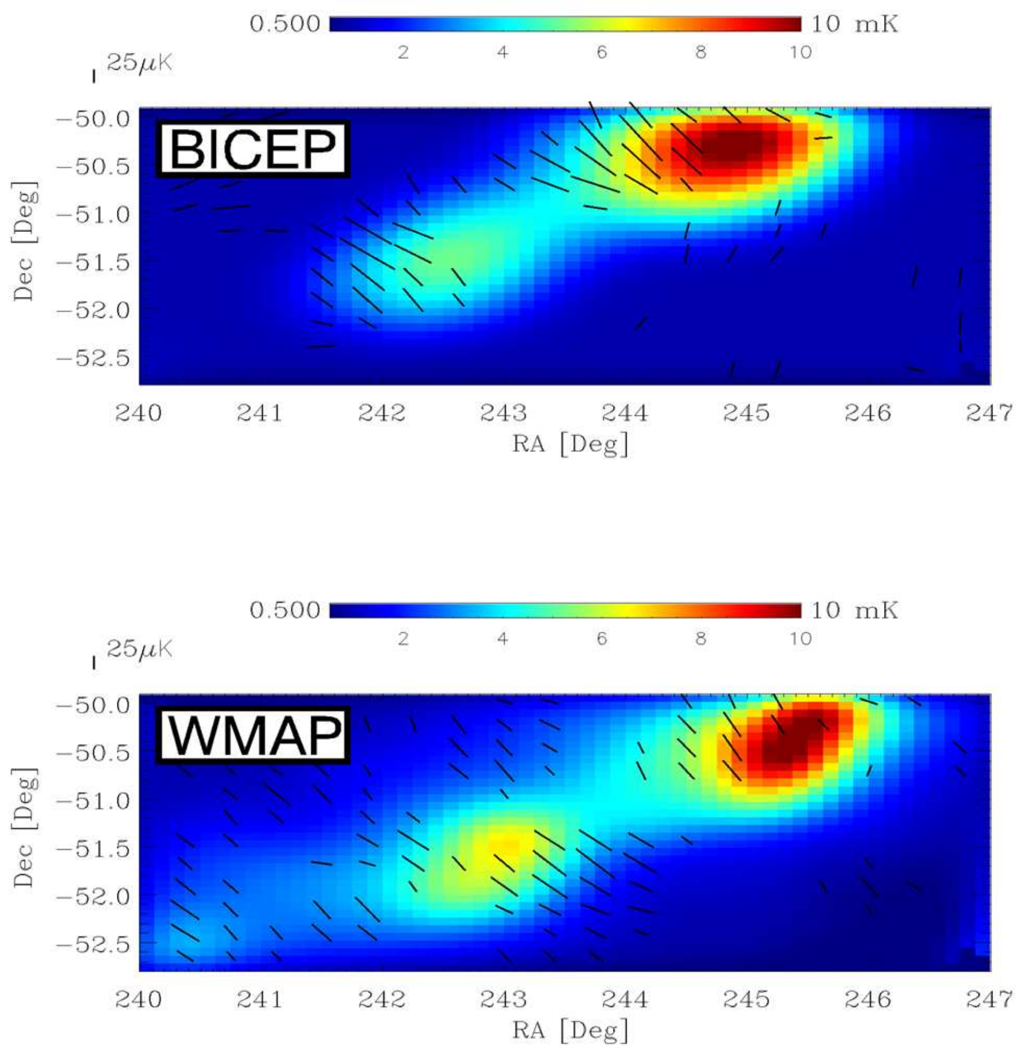

Figure 4.14: BICEP and WMAP intensity maps from four 48-hour FRM runs from the first season of BICEP over-plotted with polarization vectors. There is good general agreement between the two experiments, both in intensity, and in polarization, except for a minor boresight pointing difference in the BICEP maps. The BICEP maps are derived from observations with the FRM modulating with a 1 Hz square wave while the WMAP simulation from their three-year observations doesn't include any modulation.

Chapter 5

Conclusion and Future Work

This dissertation covers a large range of topics from design, computer modeling, construction of parts and devices, implementation of software and hardware, testing and characterization, and analysis of a large data set. My graduate career did not focus on one single ability or one pathway, allowing me to engage in research of this set of diverse topics. I believe this experience gives me a unique perspective from which to draw conclusions about my research.

FRM technology is interesting and novel. While the challenges of implementing his technology were met, it did not end up being used in the final results for the experiment. The general concept of a modulator is an extremely important both from a technology standpoint and from a data recovery standpoint. With an ever decreasing signal-to-noise ratio future experiments will undoubtedly need to integrate more and more complicated modulation schemes. Another area of research would be optimal ways to decode the information in the presence of different types of noise and systematics. Technology development is moving fast in the field and so a robust way of modulating and demodulating will need more time to become mature. Alternative methods of modulating and neutralizing beam systematic should be explored as well such as with half-wave plates, possible phase-shifting of signal on integrated TES dipole antenna wafers, or mechanically moving devices.

The telescope characterization work was very useful for the Galaxy paper as well as the CMB polarization studies from BICEP data. CMB telescopes will need to be characterized even more precisely in the future, which is why this is an area which will be expanding. It will hopefully also become an area that matures in technology and hopefully off-the-shelf calibration devices will become more standard. However, more precise methods of telescope characterization are needed, especially for future satellite missions that cannot be modified after launch very easily.

220 GHz technology will be used again at some point. The method I used for implementing the technology, coupling a 220-feedhorn to a 150-bolometer, was unique. Ultimately the data were limited by noise and systematics. Eventually, to reach the highest possible sensitivity on the sky, future experiments will at some point have to remove foregrounds and separate them from the CMB signal. An experiment like Planck will do a very good job of showing how taking measurements at many bands is necessary to fully understand astronomical emission. While initial detection of cosmological B-modes will most likely be made at one or two bands, it is also possible that detection won't ever be made until more complete observations are made across the electromagnetic frequency spectrum.

Analysis methods in this paper range from simple to complex. While I have spent great effort on the complex techniques, it is the simple techniques that will most likely be used in the future. Analysis techniques used in mapmaking only need to be as good as the data are bad. If all experiments were systematics-free and only had white noise, the simplest possible techniques would suffice. Even if the data are not optimal, the simple techniques will still provide a useful baseline for comparison. There is definitely a great amount of work that can be done to optimize CMB data analysis but it is also important to develop broad straight-forward techniques.

Bibliography

Ade, P. A. R., Pisano, G., Tucker, C., & Weaver, S. 2006, in Proc. SPIE, Vol. 6275, 62750T

Amblard, A., Cooray, A., & Kaplinghat, M. 2007, Phys. Rev. D, 75, 083508

Bennett, C. L., et al. 2003, ApJS, 148, 1

Benoît, A., et al. 2004, A&A, 424, 571

Bierman, E. M., et al. 2011, ApJ, 000, 0000

Bin, M., Benford, D. J., Gaidis, M. C., Buttgenbach, T. H., Zmuidzinas, J., Serabyn, E., & Phillips, T. G. 1999, International Journal of Infrared and Millimeter Waves, 20, 383

Bock, J., et al. 2008, ArXiv e-prints, 0805.4207 [astro-ph]

Bracewell, R. N. 1986, The Fourier Transform and its applications, ed. Bracewell, R. N.

Burn, B. J. 1966, MNRAS, 133, 67

Chiang, H. C., et al. 2010, ApJ, 711, 1123

Chuss, D. T., Davidson, J. A., Dotson, J. L., Dowell, C. D., Hildebrand, R. H., Novak, G., & Vaillancourt, J. E. 2003, ApJ, 599, 1116

Culverhouse, T., et al. 2010, ApJ, 722, 1057

Davis, Jr., L., & Greenstein, J. L. 1951, ApJ, 114, 206

Dickman, R. L. 1978, ApJS, 37, 407

Dodelson, S., et al. 2009, in Astronomy, Vol. 2010, astro2010: The Astronomy and Astrophysics Decadal Survey, 67–+

Dotson, J. L., Vaillancourt, J. E., Kirby, L., Dowell, C. D., Hildebrand, R. H., & Davidson, J. A. 2010, ApJS, 186, 406

Draine, B. T., & Fraisse, A. A. 2009, ApJ, 696, 1

Duband, L., Hui, L., & Lange, A. 1990, Cryogenics, 30, 263

Dunkley, J., et al. 2009, in AIP Conf. Ser. 1141, CMB Polarization Workshop: Theory and Foregrounds, ed. S. Dodelson et al. (Melville, NY: AIP), 222

Eriksen, H. K., Jewell, J. B., Dickinson, C., Banday, A. J., Górski, K. M., & Lawrence, C. R. 2008, ApJ, 676, 10

Eriksen, H. K., et al. 2006, ApJ, 641, 665

Finkbeiner, D. P. 2003, ApJS, 146, 407

Finkbeiner, D. P., Davis, M., & Schlegel, D. J. 1999, ApJ, 524, 867

Fixsen, D. J., & Mather, J. C. 2002, ApJ, 581, 817

Fosalba, P., Lazarian, A., Prunet, S., & Tauber, J. A. 2002, ApJ, 564, 762

Gault, A., Bierman, E., Hyland, P., Keating, B., Malu, S., & Timbie, P. 2011

Glenn, J., Walker, C. K., & Young, E. T. 1999, ApJ, 511, 812

Grossman, E. 1989, Airhead Software Co

Hamaker, J. P., & Bregman, J. D. 1996, AAPS, 117, 161

Hansen, F. K., Banday, A. J., Eriksen, H. K., Górski, K. M., & Lilje, P. B. 2006, ApJ, 648, 784

Heiles, C. 2000, AJ, 119, 923

Hildebrand, R., & Kirby, L. 2004, in ASP Conf. Ser. 309, Astrophysics of Dust, ed. A.N. Witt, G.C. Clayton, & B.T. Draine (San Francisco, CA: ASP), 515

Hildebrand, R. H. 1983, QJRAS, 24, 267

—. 1988a, Astrophysical Letters Communications, 26, 263

—. 1988b, QJRAS, 29, 327

Hildebrand, R. H., Dotson, J. L., Dowell, C. D., Schleuning, D. A., & Vaillancourt, J. E. 1999, ApJ, 516, 834

Hiltner, W. A. 1951, ApJ, 114, 241

Jarosik, N., et al. 2007, ApJS, 170, 263

Jones, T. J. 1989, ApJ, 346, 728

—. 2003, New Astronomy Review, 47, 1123

Jones, W. C., Bhatia, R., Bock, J. J., & Lange, A. E. 2003, in Proc. SPIE, 4855, 227

Jones, W. C., et al. 2007, A&A, 470, 771

Kamionkowski, M., Kosowsky, A., & Stebbins, A. 1997, Phys. Rev. D, 55, 7368

Keating, B. G., Ade, P. A. R., Bock, J. J., Hivon, E., Holzapfel, W. L., Lange, A. E., Nguyen, H., & Yoon, K. W. 2003a, in Proc. SPIE, 2855, 227

Keating, B. G., O'Dell, C. W., Gundersen, J. O., Piccirillo, L., Stebor, N. C., & Timbie, P. T. 2003b, ApJS, 144, 1

Kogut, A., et al. 2007, ApJ, 665, 355

Larson, D. L., Eriksen, H. K., Wandelt, B. D., Górski, K. M., Huey, G., Jewell, J. B., & O'Dwyer, I. J. 2007, ApJ, 656, 653

Lazarian, A. 2007, Journal of Quantitative Spectroscopy and Radiative Transfer, 106, 225

Leach, S. M., et al. 2008, A&A, 491, 597

Li, H., Dowell, C. D., Goodman, A., Hildebrand, R., & Novak, G. 2009, ApJ, 704, 891

Martin, D. H., & Puplett, E. 1970, Infrared Physics, 10, 105

Martin, P. G., & Whittet, D. C. B. 1990, ApJ, 357, 113

Mather, J. C., et al. 1994, ApJ, 420, 439

Mathewson, D. S., & Ford, V. L. 1970, MmRAS, 74, 139

Matsuo, H., Sakamoto, A., & Matsushita, S. 1998, PASJ, 50, 359

Matthews, B. C., McPhee, C. A., Fissel, L. M., & Curran, R. L. 2009, ApJS, 182, 143

Miville-Deschênes, M., Lagache, G., Boulanger, F., & Puget, J. 2007, A&A, 469, 595

Miville-Deschênes, M., Ysard, N., Lavabre, A., Ponthieu, N., Macías-Pérez, J. F., Aumont, J., & Bernard, J. P. 2008, A&A, 490, 1093

Novak, G., et al. 2003, ApJ, 583, L83

Page, L., et al. 2007, ApJS, 170, 335

Ponthieu, N., et al. 2005, A&A, 444, 327

Runyan, M. C., et al. 2003, ApJS, 149, 265

Rybicki, G. B., & Lightman, A. P. 1979, Radiative processes in astrophysics, ed. Rybicki, G. B. & Lightman, A. P.

Seljak, U., & Zaldarriaga, M. 1997, Physical Review Letters, 78, 2054

Stephens, I. W., Looney, L. W., Dowell, C. D., Vaillancourt, J. E., & Tassis, K. 2010, ArXiv e-prints

Takahashi, Y. D., et al. 2010, ApJ, 711, 1141

Tauber, J. A., et al. 2010, A&A, 520, A1+

Timbie, P. T., et al. 2006, New Astron. Rev., 50, 999

Tucci, M., Martínez-González, E., Vielva, P., & Delabrouille, J. 2005, MNRAS, 360, 935

Vaillancourt, J. E. 2007, in EAS Publications Series, Vol. 23, EAS Publications Series, ed. M.-A. Miville-Deschênes & F. Boulanger, 147–164

Weiler, K. W. 1973, A&A, 26, 403

Whittet, D. C. B. 1992, Dust in the galactic environment (Taylor and Francis)

Yoon, K. W., et al. 2006, in Presented at the Society of Photo-Optical Instrumentation Engineers (SPIE) Conference, Vol. 6275, Society of Photo-Optical Instrumentation Engineers (SPIE) Conference Series